KINETICS OF PULVERIZED COAL COMBUSTION AT HIGH PRESSURES

Donlad. J. Eckstrom, Albert S. Hirschon*, Ripudaman Malhotra*, Stephen Niksa[#]*

*SRI International, 333 Ravenswood Avenue
Menlo Park, CA 94025
[#]Niksa Energy Associates, 1745 Terrace Dr., Belmont, CA 94022

Introduction

As part of the U.S. Department of Energy's project called "High Pressure Coal Combustion Kinetics," SRI has performed a series of experiments on pulverized coal that are characteristic of the near burner flame zone (NBFZ). The objectives of these experiments are (a) to provide new data for pressurized coal combustion that benchmark kinetic models for pyrolysis, gaseous and solid product production and burnout, and pollutant formation, and (b) to generate samples of solid combustion products for analyses to fill crucial gaps in knowledge of char morphology, formation of inorganic fumes and fly ash, and fly ash utilization potential for combustion at high pressure. In pursuit of these objectives, we determine all solid, aerosol, and gaseous product formation during the transition from secondary pyrolysis, through vapor phase and soot burnout, to partial char burnout. In another phase of this project, the data from these experiments are being used to develop chemistry submodels that could be plugged into full-scale CFD simulators.

Tests in the NBFZ test configuration simulate near-burner p.f. flame conditions without the complications of turbulent, rotational, swirling flow fields. For tests with a particular fuel-type, particle size, and pressure, the furnace temperature, suspension loading, and nominal residence time are fixed while the inlet O_2 concentration is varied from 0 to 50 %, to progressively increase the S. R. values. A case without O_2 determines the total volatiles yield and distributions of so-called secondary volatiles pyrolysis products, which are the volatiles and soot remaining after the primary volatiles from the coal are pyrolyzed further in hot gases. They consist of soot, oils, CH_4, C_2H_2, CO, CO_2, H_2O, H_2, H_2S and N-species. As the inlet O_2 level is progressively increased in succeeding tests, the process chemistry moves through oxidative pyrolysis, volatiles combustion, soot oxidation, and char oxidation. Of course, these stages exhibit considerable overlap, depending on the relative burning rates of the various fuels in the reaction system. They are resolved by depletion of the available O_2; i.e., flows with higher inlet O_2 levels progress deeper into the sequence of chemical reaction stages before the flames are extinguished by the consumption of O_2.

Experimental

The Experimental Facility. The experiments were performed in a slightly modified version of our pressurized-radiant coal flow reactor shown schematically in **Figure 1**.[1] The pulverized coal path begins in the pressure vessel on the left, in which a positive displacement feeder releases coal into the drop tube where it is entrained by gases fed into the pressure vessel from below. The entrained coal passes through a U-tube and is fed into the central tube of the injector. A sheath flow of the same gas composition is fed into an annulus that surrounds the core flow; the areas, and therefore the flow rates of the entrainment and sheath flows are equal. The sheath flow was designed to keep coal particles from impinging on the flowtube walls in the hot zone, but modeling studies show that at the high pressures of these experiments turbulence rapidly mixes the particles throughout the tube cross section, and, in fact, tends to concentrate them near the walls (Liu and Niksa 2003).

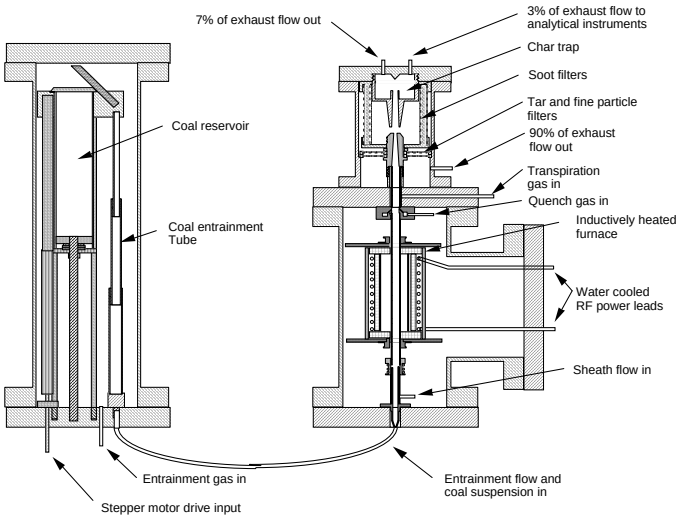

Figure 1. SRI's short-residence-time radiant-coal-flow reactor (SRT-RCFR).

The flow tube in these experiments was made of mullite, and was 16 mm OD x 12 mm ID. This tube passes through a furnace consisting of an RF-induction heated graphite sleeve of 10 cm diameter and 15 cm length. The graphite temperature is maintained in the range of 1560 – 1620 °C during the experiments, resulting in a radiant flux on the mullite tube of approximately 60 W/cm^2. The mullite tube is in near radiative equilibrium with the graphite, leading to a comparable mullite wall temperature as well as a comparable radiative flux on the particles within the tube.

The entrainment gas was argon with a varying percentage of oxygen. Because these gases are transparent to infrared radiation, the gas within the furnace is heated by a combination of conduction from the walls and convection from the radiatively superheated particles. In the absence of combustion, the gas temperature at the end of the furnace is calculated to be approximately 450 K while particle temperatures are approximately 1050 K.

At 5 cm downstream of the furnace, cold N_2 gas is injected into the flow stream at a rate of approximately 75% of the combined entrainment and sheath flow rate in order to drop the gas temperature to below 1,000 °C and thus to "freeze" the chemistry. The mixed flow is then transported through a sintered wall "transpiration" tube where another 25% of N_2 flow is added to reduce deposition on the tube walls. The flow is finally accelerated through a slightly converging nozzle into a virtual impactor called a centripeter. Particles with sufficient mass and momentum penetrate the quasi-stagnation flow at the tip of the char trap and are collected as "char." Lighter particles, characterized as tar and soot, follow the gas streamlines and are trapped on a series of quartz paper filters. Calculations indicate that the division between "heavy" and "light" particles occurs at around 15 – 20 μm. Since partially burned char particles are always larger than this and tar or soot particles are much smaller, the division between types of solid products is well defined.

After passing through the fine particle filters, the majority of the exhaust stream passes through a throttling valve that drops the pressure to atmospheric. A small fraction of gases is bled off through the char trap to assist in char capture, and additional gas is drawn from the same area for product analysis by a battery of instruments as shown in **Table 1**. Major products (CO, CO_2, H_2O) as well as O_2 are characterized to the 0.01% level, while hydrocarbons and nitrogen-containing species are measured to the ppm level. The analytical gas line is heated to minimize condensation of H_2O and oils.

Table 1. Analytical Equipment for Determining Various Gases

Analytical Equipment	Gases
Gas Chromatograph	CH_4, C_2H_x, C_3H_x, oils, H_2
FTIR	CO*, CO_2*, HCN*, NH_3, NO
Non-dispersive IR	CO, CO_2, H_2O
Paramagnetic Resonance	O_2
Wet Chemistry	HCN, NH_3

* Redundant determination

Solid product yields are determined gravimetrically. Tar samples are extracted from the filters by solution in THF followed by evaporative drying, and char, tar, and soot samples are submitted to an outside laboratory for elemental analysis. The coal feed rate is determined by calibration, and consistency of the measurements is confirmed by determining that the mass balance between coal fed and solid + gaseous products produced closes to within 5%. Furthermore, the elemental balance on C, H, and O typically also closes to 5%, with some excursions to 10%. Elemental nitrogen does not balance because we do not measure N_2 production, although at low oxygen levels N_2 is not a major product, and other species then close the N balance to about 20%.

Test Conditions. Three coals were tested, including two high volatile bituminous (Pittsburgh No. 8 and Illinois No. 6) and one western sub-bituminous (Powder River Basin). The coal samples were obtained from the Penn State coal bank; their specific identifications and properties are given in **Table 2**. Pitt #8 coal was tested at 1, 2, and 3 MPa (10, 20, and 30 bar), Illinois #6 was tested at 1 and 2 MPa, and PRB was tested at 1 MPa. The coal was ground, pre-classified by aerodynamic vortexing, and sieved to the double cut range of –140 + 200 (75 – 105 μm). Test samples were dried at 90°C overnight to moisture levels < 1% before being placed in the coal feeder reservoir.

Table 2. Composition of Coals Studied

Coal Name	Proximate Analysis, ad wt.%				Ultimate Analysis, daf wt.%				
	M	Ash	VM	FC	C	H	O	N	S
Pit. #8 DECS 23	0.7	12.3	37.9	49.1	80.8	5.4	5.8	1.7	6.3
Ill. #6 DECS 24	0.2	17.3	35.8	46.7	74.1	5.5	8.2	1.4	10.8
PRB DECS 26	0.1	5.0	39.4	55.5	73.7	5.6	19.0	1.1	0.6

The entrainment and sheath flow rates were adjusted to give an average velocity at the inlet to the furnace of 30 cm/s at all pressures. The nominal residence time in the furnace was then 500 ms, while actual residence times were substantially less because of expansion of the gas due to heating. The nominal coal feed rate was 1.5 g/min, resulting in suspension loadings of approximately 0.05 g_{coal}/g_{gas} at 1 MPa, 0.025 g_{coal}/g_{gas} at 2 MPa, and 0.017 g_{coal}/g_{gas} at 3 MPa. Higher coal feed rates led to problems of clogging or of overheating the flow tube. Oxygen concentrations in the entrainment and sheath flows ranged from zero to approximately stoichiometric. Absence of feed oxygen gave secondary pyrolysis conditions, while stoichiometric levels of oxygen were sufficient to convert tars and aerosols to soot within the available residence time. Seven to ten ratios of oxygen/coal were tested for each coal and pressure condition in order to map the transition from secondary pyrolysis through tar

Results and Discussion

Figures. 2-6 give an example of the results of measurements for Pittsburgh #8 coal at 1 MPa. **Figure 2** shows that secondary pyrolysis gives a char yield of 53% (char product/coal fed = 0.53 on a DAF basis), while the tar + soot yield was 23% (all product yields are given on a DAF basis). For this coal, an O_2/coal ratio of 2.1 corresponds to a stoichiometric ratio (S.R.) of 1. At S.R. = 1, 60% of the char and 90% of the soot have been consumed. Hydrogen is 95% consumed (**Figure 6**), while the volatile hydrocarbon products are essentially totally consumed at oxygen levels well below stoichiometric (**Figure 4**). The volatile nitrogen species HCN and NH_3 decrease by >99% and 90%, respectively, as the oxygen level increases, while NO increases (**Figure 5**). These opposing trends result in a minimum in the nitrogen pollutants at an S.R. = 0.75. Note that the experiments are conducted in Ar/O_2 mixtures rather than N_2/O_2 mixtures, so that the thermal NOx mechanism is not operative. Analogous sets of data were collected at other pressures and for the other coals to study the effect of pressure and coal type on the combustion.

The effects of pressure on pyrolysis and combustion of Pittsburgh #8 coal are summarized in **Figures 7-9**. In these figures, the burnout histories of char, soot, and hydrocarbons with increasing oxygen are presented in the form of percent burnout of the initial quantity of each species produced by secondary pyrolysis. The increasing thermal capacity of the entrainment gas with increasing pressure results in lower gas temperatures, and thus delayed flame ignition, and it is this effect that dominates the reduced char burnout with increasing pressure seen in **Figure 7**. However, the same effect is not apparent in the soot and hydrocarbon burnout histories.

The effect of coal type at a pressure of 1 MPa is summarized in **Figures 10-12**. **Figure 10** shows that char burnout is much more extensive for the sub-bituminous PRB coal than for the bituminous Illinois #6 or Pittsburgh #8 coals, consistent with expectations based on coal rank. Similar trends hold for soot burnout shown in **Figure 11**, although this may be a thermal effect (i.e., somewhat higher flame temperatures and more extensive flames because of enhanced char burnout) since the soot compositions were found to be nearly independent of coal type.

Conclusions

In spite of the challenges of measuring complete gaseous and solid product yields at elevated pressures and temperatures, we were able to cover the entire NBFZ operating domain by running the SRT-RCFR facility at a fixed coal feedrate with variable inlet O_2 concentrations to impose the same range of S.R. at all test pressures. This strategy yielded datasets for three coals at 1.0, 2.0 and 3.0 MPa. These data represent a major advance in the fundamental characterization of near-burner p.f. combustion at elevated pressures.

The measurements are of such quality that only relatively small adjustments to the raw data were needed to close the balances on mass and C/H/N within ± 5 % in individual runs. The adjusted datasets show the expected tendency in the burnout of gaseous and solid fuels to increase steadily for progressively more oxidizing conditions. They also show that formation of NOx increases rapidly at S.R. values above 0.5. These data are well suited to serve as benchmarks for development of kinetic models for pyrolysis, gaseous and solid product production and burnout, and pollutant formation, as well as for characterizing char and ash properties. The data are also being used to tune chemical submodels that describe evolution of the different species in a manner that can be incorporated into full-scale CFD process simulators.[2]

Acknowledgement. This research was sponsored by the National Energy Technology Laboratory, U. S. Department of Energy, under subcontract Agreement No. FY00012SRI from Prime Contract DE-FC26-01NT40777 to Fluent Incorporated.

References

(1) Cor, J., Manton, N., Mul, G., Eckstrom, D., Olson, W., and Malhotra, R., *An Experimental Facility for the Study of Coal Pyrolysis at 10 Atmospheres*, Energy and Fuels, **14**, 692-700, 2000.

(2) Liu, G. and Niksa, S., *DoE High Pressure Coal Combustion Kinetics, Task 1.3. P-RCFR Simulations for NBFZ Tests*, Third Interim Report, March 26, 2003 (unpublished).

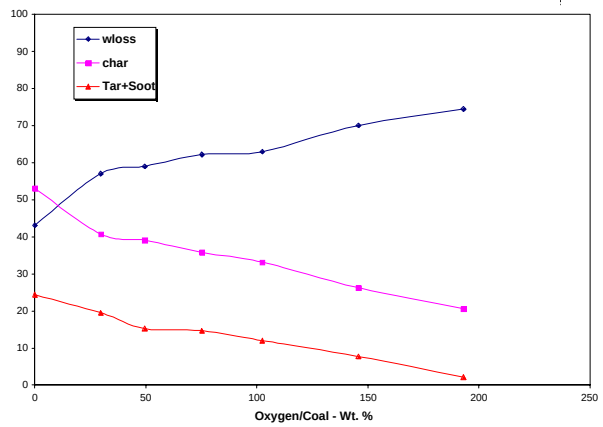

Figure 2. Yield of major products during combustion of Pitt coal at 1.0 MPa.

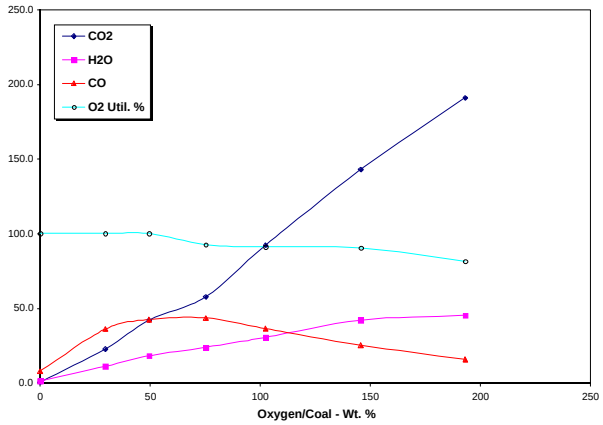

Figure 3. Yield of oxygenated gases during combustion of Pitt coal at 1.0 MPa.

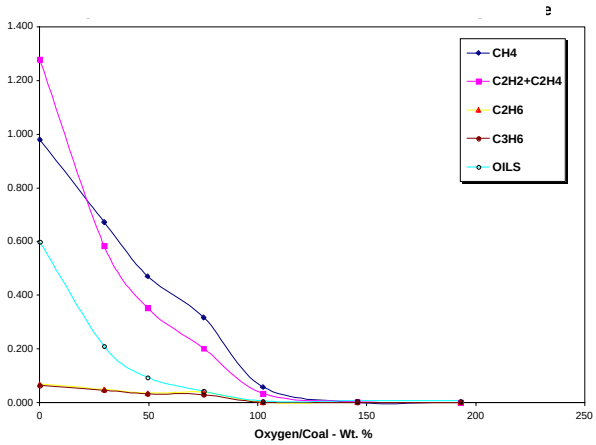

Figure 4. Yield of hydrocarbon gases during combustion of Pitt coal at 1.0 MPa.

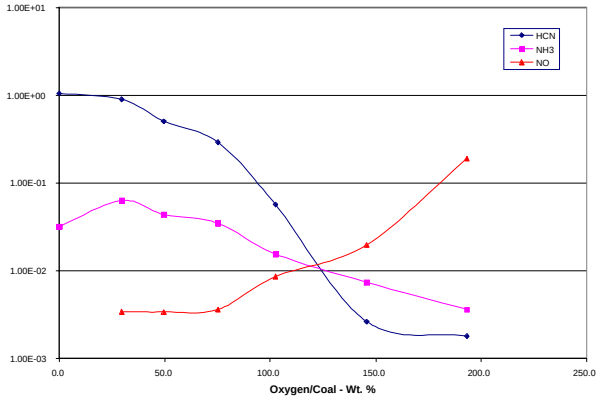

Figure 5. Yield of nitrogen gases during combustion of Pitt coal at 1.0 MPa.

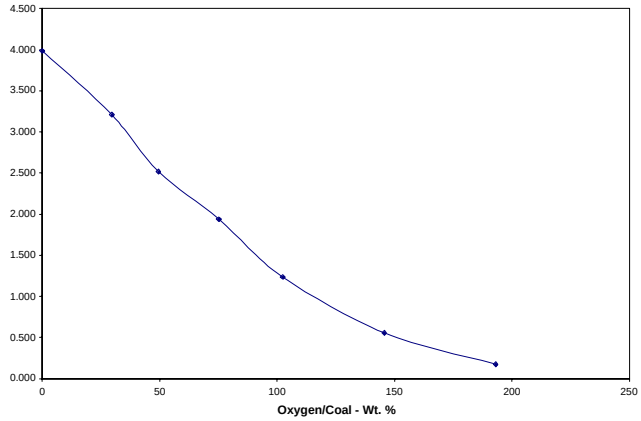

Figure 6. Yield of Hydrogen during combustion of Pitt coal at 1.0 MPa.

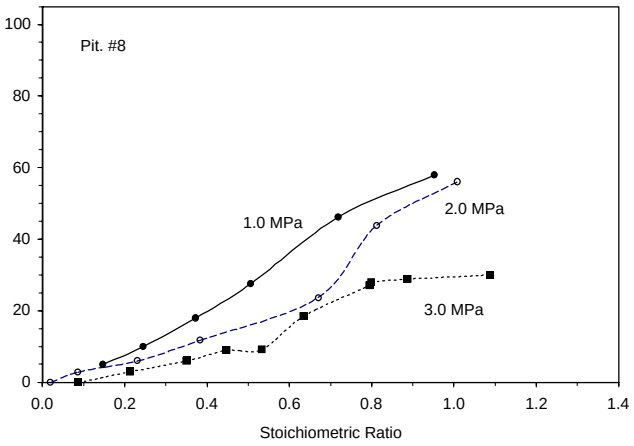

Figure 7. Char burnout at various pressures for Pitt coal.

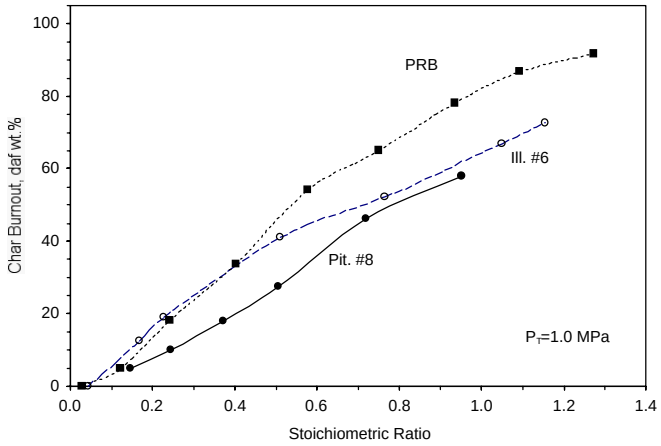

Figure 10. Char burnout for PRB, Pitt, and Ill coals at 1.0 MPa..

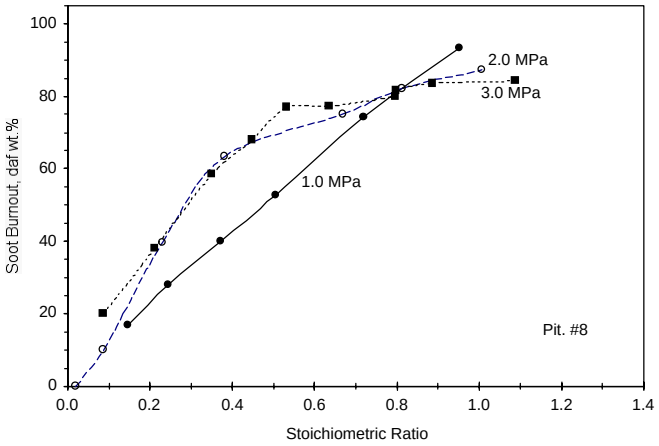

Figure 8. Soot burnout at various pressures for Pitt coal.

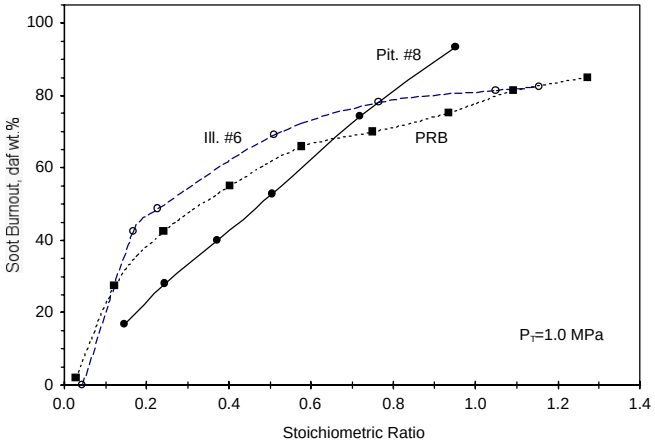

Figure 11. Soot burnout for PRB, Pitt, and Ill coals at 1.0 MPa..

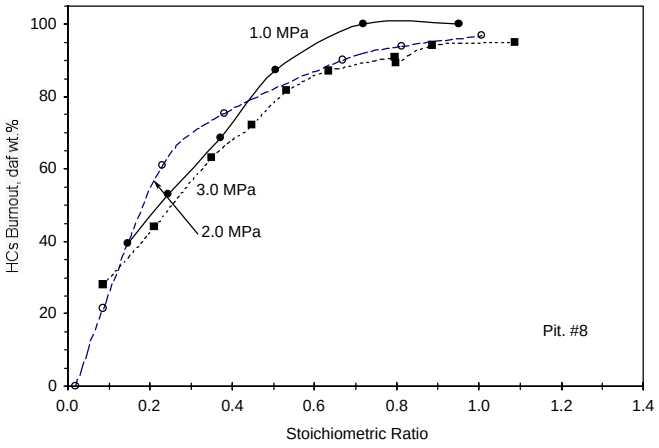

Figure 9. Hydrocarbon burnout at various pressures for Pitt coal.

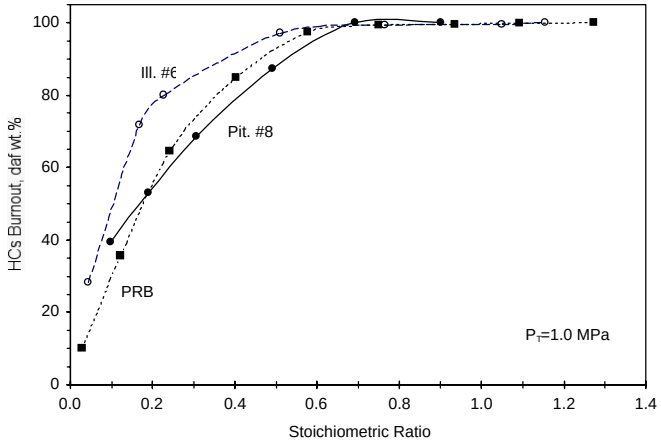

Figure 12. Hydrocarbon burnout for PRB, Pitt, and Ill coals at 1.0 MPa..

Application of a Circulating Fluidized Bed Process for the Chemical Looping Combustion of Solid Fuels

Yan Cao, Kunlei Liu, John T. Riley and Wei-Ping Pan

Institute for Combustion Science and Environmental Technology (ICSET)
Western Kentucky University, Bowling Green, KY 42101
Email: yan.cao@wku.edu

Introduction

In recent years more concerns have arisen about CO_2 emission due to global warming. Among available or proposed technologies, chemical looping combustion[1] (CLC) is the most promising technology to combine fuel combustion and CO_2 purification. It uses a solid oxygen carrier to transfer the oxygen from the air to fuel in a reducer and oxidizer. Thus, air is never mixed with the fuel, and the CO_2 does not become diluted by the nitrogen of the flue gas. NO_x formation can be largely eliminated. A number of metals have been discussed in the literature,[2] such as oxides of Fe, Ni, Co, Cu, Mn.

Solid fuels such as coal and biomass have been ignored in CLC process due to technical problems, including the separation of oxygen carrier from fuel and ash, the possible interaction between the fuel ash and oxygen carriers and the combustion of unburned carbon particles in the oxidizer due to the circulation of solid fuel particles. The adaptation of the CLC to the combustion of solid fuels presents many challenges.

In this paper, an innovative concept – application of a CFB combined with a moving bed on the chemical looping combustion of solid fuels is introduced.

Technical Approach

Is it possible to add solid fuel into a reducer directly? There exist several technical difficulties. The reaction rate between solid fuel and the oxygen carrier is slow for a solid fuel due to low solid-solid contact efficiency and reactivity. The solid fuel gasification rate is always 1000 times slower compared to combustion at the same evaluated temperature.

In order to overcome the technical difficulties mentioned, it is proposed that a CFB coupled with a moving bed be used for the chemical looping combustion of solid fuels. In this approach, the facility will consist of three major components – a high-velocity riser acting as an oxidizer, a down-flow moving bed acting as a gasifier and a low-velocity bubbling bed acting as a deep reduction reactor and separation device for the oxygen carrier from fuel ash as well as unburned carbon. The whole system uses two loop seals for oxygen carrier circulation.

Kinetic Analysis. The CLC process is governed by the prevailing chemical thermodynamics and kinetics. The gasification rate could be fast enough to match the rate of oxygen carrier reduction in the down-flow moving bed.

All reactions related to the pyrolysis and gasification of fossil fuel are endothermic, as illustrated by Equations (1), (2) and (3). In the proposed CLC system, the gasification process for solid fuel is combined with a reduction process for the oxygen carrier in the reducer where no oxygen exists. The only way to supply heat for the fossil fuel gasification process is the reduction reaction of oxygen carrier with the syngas produced.

$C_nH_mO_p \rightarrow (p\text{-}n)CO_2 + (2n\text{-}p)CO + (2/m)H_2$, 5 Kcal/mol (1)
$C + H_2O \rightarrow CO + H_2$, 28.3 Kcal/mol (2)
$C + CO_2 \rightarrow 2CO$, 38.4 Kcal/mol (3)

Just a few metal oxides that have been developed as oxygen carriers for the CLC process show exothermic properties when reacted with carbon. The possible reactions related to oxygen carrier candidates and carbon in the reducer are shown in Table 1. Thus, the enthalpy of solid fuel combustion in the chemical looping process is equal to the sum of the enthalpies of the two steps. Copper oxide shows an exothermic property due to the smaller enthalpy of its oxidizing step than those of solid fuel direct combustion.

Table 1. Reaction Enthalpies at 1000°C and 1 atm [3]

$C + O_2 \rightarrow CO_2$, -392.75 KJ/mol
Endothermic
$2\ NiO + C \rightarrow 2\ Ni + CO_2$, 75.21KJ/mol
$2\ MnO + C \rightarrow 2\ Mn + CO_2$, 378.98 KJ/mol,
$2\ Mn_3O_4 + C \rightarrow 6\ MnO + CO_2$, 56.7 KJ/mol
$2/3\ Fe_2O_3 + C \rightarrow 4/3\ Fe + CO_2$, 146.37 KJ/mol
$2\ PbO + C \rightarrow Pb + CO_2$, 32.82 KJ/mol
Exothermic
$2\ CuO + C \rightarrow Cu + CO_2$, -96.51 KJ/mol
$2\ Cu_2O + C \rightarrow 4\ Cu + CO_2$, -61.04
$2\ Mn_2O_3 + C \rightarrow 4\ MnO + CO_2$, -33KJ/mol

Lead is a hazardous element and not used. Manganese oxides could produce non-reactive compounds. Also, there is a thermodynamic limitation in the reduction reaction of manganese. Most of oxygen in copper oxide is active for reaction with methane, and the highest efficiency could be achieved. Thus, it is selected as the preliminary candidates for oxygen carriers for the CLC for solid fuel combustion.

Thermodynamics Analysis. Chemical reaction thermodynamics phase diagram for the reduction reactions by CO produced in solid fuel gasification process are shown in Figures 1.

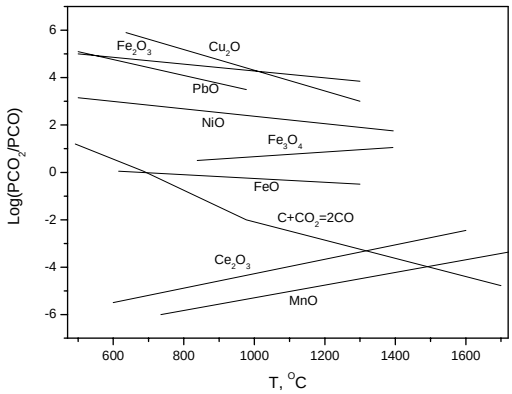

Figure 1. Variation of the thermodynamics equilibrium factor for MeO-CO as a function of temperature[3]

Figure 1 shows that the ratio varies from approximately 10^5 for the reduction of Cu_2O to values on the order of 10^{-5} or less for the reduction of MnO to Mn. For the reduction of a metal oxide with CO in the absence of solid carbon, the oxides of copper, lead and nickel will be reduced to elemental form at gas ratios between 10^5 and 10^2. Therefore, the completeness of the reaction could be

achieved and a concentrated CO_2 stream will be obtained in the proposed CLC system. The reduction of manganese requires a CO_2-free environment, which is practically impossible for the CLC of solid fuel to achieve. Because carbon is also present in the reaction mixture in the proposed reducer, the reduction of metal oxide and carbon gasification to CO_2 occurs simultaneously. As shown in Figure 1, above the simultaneous equilibrium temperature where two curves for the reduction of metal oxides and the Boudouard reaction intersect, MnO needs to be above 1600^{o}C, which is impossible in the CLC due to high temperature. In contrast, the curves for NiO, Cu_2O, PbO and Fe_2O_3 do not have intersection with the carbon curve even at low temperatures. The simultaneous reactions are not limited by thermodynamics, they are determined entirely by kinetics, which typically are fast in the CLC. Thus, using NiO, Cu_2O, CuO and PbO as oxygen carriers could result in higher ratios of $P_{CO2}/P_{CO.}$

Similarly, analysis of the reduction of metal oxides with H_2 shows that it is less exothermic than its corresponding reaction with CO. Moreover, equilibrium of the water-gas reaction will occur and shift to the right at lower temperatures. This shows H_2 at high temperature is a better reducing agent than CO for oxygen carriers.

Process Analysis. The volume of the gas flow in the air reactor is much larger than that in a reducing reactor because a large amount of nitrogen in the air is carried in. Moreover, the oxidizing rate of the oxygen carrier is much faster than the rate of the reducing reaction. Thus, a high gas velocity is chosen in the oxidizing reactor to keep a reasonable size reactor and to reduce the capital cost. In the reducer, long residence times, on the order of minutes, is needed for solid fuel gasification and oxygen carrier reduction due to slow reaction rates. Meanwhile, only a small amount of gas is needed for fossil fuel gasification, so a down-flow moving bed was selected. In accordance with the huge density and size differences between ash and the oxygen carrier, a low-velocity bubbling bed was chosen to separate the oxygen carrier from fuel ash as well as unburned carbon. The whole system uses two loop seals for oxygen carrier circulation.

Conclusions

Purifying CO_2 in an efficient and energy-saving way is the first and most important step for its sequestration. Chemical looping combustion could achieve this goal when it is applied to solid fuel in a highly practical way. An innovative concept was proposed to apply a CFB combined with a moving bed in the CLC of solid fuels. A coal gasification process which occurs in the moving bed in a loop seal, will be combined with a reduction process of metal oxide to achieve direct utilization of solid fuel. Thermodynamics Analysis showed that using Cu_2O, CuO as oxygen carriers could result in higher ratios of P_{CO2}/P_{CO} in solid fuel CLC process.

References

1. Marion, J.; Naskala, Y.N.; Griffin, T. "Controlling Power Plant CO_2 Emissions: a Long Range Approach," *Proceedings* of the First National Conference on Carbon Sequestration, **2001**, Washington, DC, DOE/NETL-2001/1114. (on CD-ROM).
2. Mattisson, T.; Jarders, A.; Lyngfelt, A. "Reactivity of some Metal Oxide Support on Alumina with Alternating Methane and Oxygen-application for Chemical-looping Combustion," *Energy & Fuels*, **2003,** *17*, 643-651.
3. P.W. Atkins. *Physical Chemistry*, fifth edition, W.H. Freeman and Company, New York.

CARBONACEOUS MATERIALS FOR GAS PHASE DESULFURIZATION: ROLE OF SURFACE HETEROGENEITY

Andrey Bagreev, Teresa Bandosz

Department of Chemistry, The City College of New York
New York, N Y 10031

Introduction

Removal of sulfur containing species becomes nowadays a strategic issue [1, 2]. It is due to strict environmental regulations combined with searching for new clean sources of energy such as fuel cell. For fuel cell application gaseous fuel has to be almost free of sulfides or mercaptans. Those species poison the reforming catalysts thus causing shortening of the life-time of a cell and an increase in the costs of energy. Since sulfur containing gases are toxic and they have very low odor threshold all efforts are made to filter air form facilities where anaerobic digestion can occur such as, for instance form municipal waste water treatment plants [3-6].

Among various methods used to remove hydrogen sulfide, adsorption on activated carbons is considered as a very efficient and cost effective approach. This is the result of unique surface properties of carbonaceous adsorbents [7-10] such as high surface area, and pore volume, along with surface chemistry, which promotes catalytic oxidation of H_2S in the presence of even small amounts of air and moisture [11-23]. As a result of surface reaction, hydrogen sulfide is oxidized either to sulfur or sulfur dioxide. The latter process, in order to retain a significant amount of sulfur species on the surface, has to proceed further and SO_2 is oxidized to sulfuric acid. Due to the reactions mentioned occur at room temperature and under atmospheric pressure the physical adsorption of hydrogen sulfide is negligible at these conditions [15].

To enhance the catalytic properties of activated carbon various methods have been used [2] from which the most common is impregnation of activated carbon with sodium or potassium hydroxide or salts containing potassium such as potassium carbonate [3, 5, 23-27]. Doing this only slightly increases the cost of materials leading to the much better performance [6]. But since an ideal solution never exists the application of caustic impregnated carbons carries certain drawbacks. The most significant is a low ignition temperature. In the presence of caustic a strong exothermic reaction occurs and a carbon bed can easily self-ignite resulting in enormous cost of extinguishing and a widely spread environmental damage. Another issue is related to safety of working with hazardous materials, as is a caustic solution present on the surface of carbons.

All of these resulted in a search for better adsorbents that, with sustained efficiency, would be much safer to work with. The window of opportunity opened in surface chemistry of carbons. This is an important factor governing their catalytic properties [10, 28, 29]. One method of modification, usually applied during production of adsorbent, is introduction of nitrogen containing groups [30-32]. Like in the case of caustic materials, such carbons are basic and the high dispersion of catalytic sites in the pore system provides efficient oxidation. The catalytic action is so pronounced that a surface of such carbons not only converts hydrogen sulfide to sulfur as in the case of caustic impregnated materials, but oxidation proceeds even further to sulfuric acid. The presence of sulfuric acid was seen as another "plus" in application of nitrogen enriched adsorbents. They can be washed out with water and thus they regeneration is inexpensive. The Calgon patent describing the performance of Centaur® claims that after loosing 20% the initial capacity as a result of the first run, the carbons maintain their performance on 80% level practically forever [31]. Taking into account that the capacity of such carbon is about half of the capacity of the caustic impregnated materials the situation looked almost ideal. But, as mentioned above an ideal solution does not exit. Additional step in the preparation of carbon (impregnation with urea of low temperature chars) increases the cost of materials. Although the smaller capacity than that of caustic impregnated carbon can be compensated by many steps of inexpensive regeneration, once again the practical and safety reasons limit the applications of such carbons. Concentrated sulfuric acid present on the surface can lead to health hazard (skin burning) and many facilities do not feel comfortable with regeneration system where strong acid is generated.

The mentioned above factors directed the attention of scientists and engineers to virgin materials. During the last few years the performance and suitability for hydrogen sulfide removal of many types of unmodified carbon have been described in the literature [6, 13-16, 33]. When the concentration of hydrogen sulfide in air is less then 100 ppb virgin carbons can provide the sufficient protection for few years [6]. It was shown that the capacity and the degree of hydrogen sulfide oxidation depend on the porosity and the surface chemistry [13-16]. Moreover, the content of inorganic matter in ash has proven to be important [34]. This concept led to the development of new, sewage sludge adsorbents [35-38]. Although their content of carbon is only about 20 %, their capacity is much better than that of virgin, coconut shell based activated carbon. An important advantage of those materials is conversion of hydrogen sulfide to sulfur and low costs of production.

An objective of this paper is to demonstrate the importance of surface heterogeneity and its effect on the amount of hydrogen sulfide adsorbed on carbonaceous materials and on the products of surface reactions. Very often the choice of adsorbent is governed not only by its cost and removal capacity but also by the other factors such as, for instance, the possibility of regeneration or the level of toxicity of the spent materials. The results presented here summarize the effects of surfaced features on the capacity and chemistry of the processes occurring during adsorption of H_2S on carbonaceous materials.

Experimental

Materials. Five carbonaceous materials were investigated in this research. They are as follows: STIX (cautic impregnated bituminous cola based- Watrelink Barnabey and Sutcliffe) Midas OCM^{TM} (US Filters) [39], Centaur® (Calgon), S-208 (coconut shell based- Waterlink Barnabey and Sutcliffe), and laboratory made sewage sludge derived adsorbent, referred here as SC carbon. After exhaustion in H_2S breakthrough capacity test the letter E is added to the name of the samples.

Methods

H_2S breakthrough capacity. The standard dynamic test (ASTM D 6646-01) [40] was used to evaluate the performance of carbons for H_2S adsorption. Humidified air (relative humidity 80% at 293K) containing 1% (10,000ppm) of H_2S was passed through a column of carbon (diameter 1", bed height 9"). The test was stopped at breakthrough concentrations of 50 ppm. Then the breakthrough capacity for H_2S adsorption was calculated using concentration of adsorbat, flow rate, breakthrough time and volume of carbon.

pH of carbon surface. A pH of the carbon surface was evaluated according to ASTM D 3838 standard procedure. Briefly, 10 g of activated carbon was placed in 100 mL of hot water and boiled gently for 900 s. Then the flask content was filtered, filtrate was cooled, and pH was measured.

Sorption of nitrogen. Nitrogen isotherms were measured using a ASAP 2010 (Micromeritics) at –196 ^{o}C. Before the experiment the samples were heated at 120 ^{o}C and then outgassed at this temperature under a vacuum of 10^{-5} Torr to constant pressure. The isotherms were used to calculate the specific surface area, micropore volume (DR method), V_{mic}, mesopore volume, V_{mes}, total pore volume, V_t,, and pore size distributions [41-42].

Thermal analysis. Thermal analysis was carried out using TA Instruments Thermal Analyzer. The instrument settings were: heating rate 10 deg/min and either air or nitrogen atmosphere with 100 mL/min flow rate. The residues after heating in nitrogen and air (ash content) at 1000^{o}C are reported. From the experiments run in air the ignition temperature was determined [6]. Experiment carried out in nitrogen provided information about the speciation of surface oxidation products.

Apparent density. Apparent density of carbons was evaluated using ASTM Method D 2854 [43]. It is determined on a granular sample be measuring the volume packed by a free fall from a vibrating feeder into an approximately sized graduated cylinder and determining the mass of the known volume.

Moisture. Content of moisture was evaluated using ASTM Method D 2867 [43]. A sample of carbon is put into a dry, closed weighting dish and weighted accurately. Then the dish is opened and placed with the lid in a preheated oven. The sample is dried to constant weight and cooled in dessicator. The weight loss is expressed as a percentage of the weight of the original sample.

Results and Discussion

From the measurement of the hydrogen sulfide breakthrough curves, taking into account the density of materials, the breakthrough capacity was calculated. The results are summarized in Table 1 along with the pH values of the carbon surfaces. Analyzing the data it is seen that Midas® outperforms other materials. Its capacity per unit volume bed is twice higher than that of Centaur® whereas the capacity the sewage sludge derived material is twice higher than that of STIX. The carbons also behave differently when water adsorption is considered. As shown previously [34], presence of water is a crucial factor enhancing hydrogen sulfide adsorption. It enables dissociation of to HS^- ions [13], when the pH allows it. It is well known that activated carbon surface is considered as hydrophobic. Adsorption of water usually occurs as a result of the presence of oxygen or nitrogen containing functional groups and inorganic matter [44]. High adsorption of water on Midas® and Centaur® is the result of long exposure to humidified air (longest breakthrough time) and also affinity of surfaces to retain water. In the case of Centaur® this is linked to the nitrogen containing groups whereas in the case of Midas® hydration of inorganic matter likely plays a role.

In order to discuss the performance of materials as removal media in the process where catalytic action is expected to enhance their performance, the structural and chemical features of surfaces have to be described. The simplest estimation of carbon surface chemistry is the measurement of the pH of its water suspension [13]. As listed in Table 1 all materials are basic and the pH of Midas and SC is over 10. That pH is the result of the presence of inorganic matter (basic oxides). In the case of Centaur® the closest to neutral pH value is caused by protonation of the nitrogen containing groups [45]. High pH of STIX is caused by the presence of potassium hydroxide.

Table 1. H_2S Breakthough Capacity, Amount of Water Adsorbed and pH Values of the Carbon Surfaces.

Sample	H_2S breakthrough capacity [g/g of carbon]	H_2S breakthrough capacity [g/cm^3 of carbon]	Water adsorbed [mg/g]	pH initial	pH exhausted
S208	0.036	0.02	0.04	9.8	8.82
Centaur®	0.130	0.060	0.41	8.30	1.47
Midas®	0.608	0.251	0.12	10.85	10.38
STIX	0.230	0.140	0.06	10.2	7.2
SC	0.079	0.052	0.03	10.58	9.63

The amount of ash in each material may indicate the importance of the presence of catalytic inorganic phase (Table 2). In the case of SC and Midas® the ash content is the highest. In SC it comes as a natural component of the sewage sludge precursor [35-38] whereas, in the case of Midas it was added as a part of the material preparation procedure [39]. It is important to mention that the ash content of Midas® twice exceeds the content of basic metals oxides described in the patent [39]. Relatively high amount of ash in Centaur® is linked to its bituminous coal origin. In the case of STIX about 13% of ash has its main origin in potassium hydroxide used for impregnation along with ash coming from a bituminous coal precursor.

Table 2. Density, Ash Content, Ignition Temperature and the Initial Moisture Content.

Sample	Bulk density [g/cm^3]	Ash content [%]	Moisture [%]	T_{ign} [^{o}C]
S208	0.55	1.9	5.2	425
Centaur®	0.48	5.5	6.6	510
Midas®	0.41	26.8	12.2	524
STIX	0.60	12.9	8	320
SC	0.66	76.9	2.5	426

From the nitrogen adsorption isotherms the structural parameters were calculated. They are collected in Table 3. The data clearly shows that Midas® has the highest surface area and pore volume whereas SC- the lowest. Also, either for the latter carbon or Midas® a significant contribution of mesoporosity is found. On the other had, S-208, Centaur®, and STIX, are very homogenously microporous. The highest nitrogen uptake noticed for Midas®, the lowest for SC, which is related to the differences in the chemical composition of materials. Midas® contains 70% of carbonaceous phase, SC- only 20.

Not only porosity but also the density of materials is liked to their content of inorganic matter. The densest is SC, then Midas, Centaur and S-208. This has an effect on the capacity calculated per gram (Table 1) and thus affects the cost of materials in real life operations.

The evaluation of the materials' performance is more valid when the products of surface reaction are discussed. The pH values of exhausted carbons listed in Table 1 clearly indicate the differences in the surface reaction products. Highly acidic pH of Centaur® and a noticeable decrease in the pH for S-208 and STIX suggest a significant degree of sulfuric acid formation. For SC and Midas® the pH, however slightly decreases, is still on a very high level. Such a

decrease can be caused by formation of sulfides and sulfates from oxides. Those species and sulfur, should not cause dramatic decrease in the pH value.

Table 3. Structural Parameters Calculated from Sorption of Nitrogen.

Sample	S_{N2} [m^2/g]	V_{mic} [cm^3/g]	V_t [cm^3/g]	V_{mic}/V_t
S208	877	0.43	0.46	0.96
S208E	800	0.40	0.42	0.95
Centaur®	987	0.44	0.56	0.79
Centaur®E	443	0.18	0.26	0.69
Midas®	1110	0.43	0.81	0.53
Midas®E	95	0.03	0.14	0.21
STIX	620	0.30	0.35	0.85
STIXE	340	0.18	0.26	0.69
SC	98	0.04	0.16	0.25
SCE	28	0.01	0.10	0.10

Comparison of the DTG results obtained on exhausted samples (the low temperature peak, < 250 ^oC for pure carbon materials represents removal of SO_2 from reduction of sulfuric acid [13-16] and the peaks between 300- 500 ^oC are linked to removal of sulfur from various pore sizes (from larger to smaller) [13-16]) revealed that indeed in the case of Centaur® almost only SO_2 is released, for -S208 and STIX there is a mixture of SO_2 and elemental sulfur . In the case of Midas® a huge peak representing removal of sulfur from pores of various sizes was found. For sewage sludge derived adsorbent a broad peak present between 200-400 ^oC represents sulfur [36-38]. Although its position is close to that for sulfuric acid ion S208 that shift is caused by removal of sulfur from large pores, which are present in this material. This process requires much less energy (lower temperature) than evaporation of sulfur polymers from the microporous structure as that in S-208.

Those significant amounts of sulfur adsorbed on the materials studied are stored in their pore system. As shown from Table 1 for all carbons the volumes of pores, micropores in particular, significantly decreases. This is of course linked to the decrease in the surface areas. An exact location of oxidation products is seen from the analysis of pore size distributions for carbons after exhaustion. Whereas for S-208 and Centaur® mainly volumes in pores smaller than 20 Å are affected for SC and Midas® sulfur is deposited in all pore sizes and smaller micropores are completely filled. It looks like the capacity lasts until that volume is exhausted and more pore volume would provide more capacity as expected when the catalytic actions is involved.

Another important factor which should be evaluated here is the ignition temperature of adsorbents (Table 3). The evaluation of temperature of self-ignition based shows high ignition temperature of catalytic carbons. The ignition temperatures of S-208 and SC are almost identical and about 100 ^oC lower that that for Centaur® and Midas®. Since manufacturing of those carbons requires additional steps some additive may work as fire retardants. Low ignition of caustic impregnated carbon is the result of the presence of highly reactive potassium hydroxide.

Based on the comparison presented above, and the results published elsewhere where the mechanisms of adsorption/oxidation are discussed [13, 26, 33, 36-38], the materials containing a catalytically active inorganic phase mixed with the activated carbon seem to be the best performing adsorbents. On their surface, thanks to the presence of catalytic oxides, hydrogen sulfide is oxidized to sulfur. The catalytic action is complex and consists of two different mechanisms: one on pure activated carbon surface and one on the catalytic phase. It is likley that the reaction of H_2S oxidation occurs on the carbon and oxides surfaces simultaneously with formation of elemental sulfur, metal sulfides and sulfuric acid which later reacts with carbonates.

As indicated above, the presence of water on activated carbons contributes to the dissociation of hydrogen sulfide and facilitates to its oxidation to sulfur and sulfur dioxide [33] The proposed mechanism involves 1) H_2S adsorption on the carbon surface, 2) its dissolution in a water film, 3) dissociation of H_2S in an adsorbed state in the water film , 4) surface reaction with adsorbed oxygen with formation of elemental sulfur 4a) or sulfur dioxide 4b), and 5) further oxidation of SO_2 to H_2SO_4 in the presence of water :

$$H_2S_{gas} \xrightarrow{K_H} H_2S_{ads} \quad (1)$$

$$H_2S_{ads} \xrightarrow{K_S} H_2S_{ads\text{-}liq} \quad (2)$$

$$H_2S_{ads\text{-}liq} \xrightarrow{K_a} HS^-_{ads} + H^+ \quad (3)$$

$$HS^-_{ads} + O^*_{ads} \xrightarrow{K_{R1}} S_{ads} + OH^- \quad (4a)$$

$$HS^-_{ads} + 3\,O^*_{ads} \xrightarrow{K_{R2}} SO_{2\,ads} + OH^- \quad (4b)$$

$$SO_{2ads} + O^*_{ads} + H_2O_{ads} \xrightarrow{K_{R3}} H_2SO_{4\,ads} \quad (5)$$

$$H^+ + OH^- \longrightarrow H_2O \quad (6)$$

where H_2S_{gas}, $H_2S_{ads\text{-}liq}$, and H_2S_{ads} correspond to H_2S in gas, liquid and adsorbed phases, respectively; K_H, K_S, K_a and K_{R1} , K_{R2} , K_{R3} are equilibrium constants for related processes (adsorption, gas solubility, dissociation, and surface reaction constants); O^*_{ads} is dissociatively adsorbed oxygen, S_{ads} , SO_{2ads} , $H_2SO_{4\,ads}$ represent sulfur, SO_2 and H_2SO_4 as the end products of the surface oxidation reactions.

It is known that oxides of iron, zinc and copper are used in industry as absorbents and /or catalysts of H_2S removal from different gaseous media at low (20-200^oC) and high (300-800^oC) temperatures [2]. The H_2S removal at low temperatures mainly occurs due to gas-solid reactions in a thin hydrated lattice of metal oxides. This process leads to sulfides formation:

$$ZnO + H_2S \longrightarrow ZnS + H_2O \quad (7)$$

$$CuO + H_2S \longrightarrow CuS + H_2O \quad (8)$$

$$Fe_2O_3 + 3H_2S \longrightarrow FeS + FeS_2 + 3H_2O \quad (9)$$

$$Fe_2O_3 + 3H_2S \longrightarrow Fe_2S_3 + 3H_2O \quad (10)$$

$$2Fe_2S_3 + 3O_2 \longrightarrow 2Fe_2O_3 + 6S \quad (11)$$

Carbonates of calcium and magnesium are also supposed to have high affinity for H_2S adsoption in wet condition due to neutralization reactions ([7]

$$CaCO_3 + H_2S \longrightarrow Ca(HCO_3)_2 + Ca(HS)_2 \quad (12)$$

Moreover, transition metal ions can catalyze the H_2S oxidation in aqueous solutions by molecular oxygen due to the redox process

[2]. For example, in the case of iron the following reactions may occure:

$2Fe^{3+} + HS^- \text{ ----> } 2Fe^{2+} + S + H^+$ (13)

$4Fe^{2+} + O_2 + 2H^+ \text{ ----> } 4Fe^{3+} + 2OH^-$ (14)

On the surface of caustic impregnated carbon the following reaction path have been proposed in addition to those occurring on the surface of pure carbon [21]s:

$NaOH + H_2S \text{ ---->} NaHS + H_2O$ (15)

$2NaOH + H_2S \text{ ---->} Na_2S + H_2O$ (16)

$NaHS + 0.5O_2 \text{ ---->} S + NaOH$ (17)

$Na_2S + 0.5O_2 + H_2O \text{ ---->} S + 2\ NaOH$ (18)

$2\ NaOH + H_2SO_4 \text{ ---->} Na_2SO_4 + 2H_2O$ (19)

And side reactions:

$NaOH + CO_2 \text{ ---->} NaHCO_3$ (20)

$2NaOH + CO_2 + H_2O \text{ ---->} Na_2CO_3 + 2\ H_2O$ (21)

$Na_2CO_3 + H_2S \text{ ---->} NaHCO_3 + NaHS$ (22)

The presence of NaOH and strongly basic environment enhances the dissociation of hydrogen sulfide. Moreover, according to the reactions 17-18, NaOH and basic environment is regenerated in the system enabling more H_2S to be dissociated and, as a final product, oxidized to elemental sulfur following reaction 17. The results published elsewhere [28] showed that on one mole of NaOH 3 to 4 moles of H_2S are adsorbed which clearly indicates the catalytic effect of the carbon surface. A question raises what causes that the reaction stops and it stops when almost the same capacities are reached on all materials. The possible reason for this is "inactivation" of sodium hydroxide. This may happen as a result of reactions 19-20 where carbonates and sulfates are formed on the surface. Although the pH remains basic in most cases, this can be due to the presence of carbonates not hydroxide. It makes the formation of sodium sulfides, sodium hydrogen sulfides, sodium sulfates, and sulfuric acid the most important reactions in this system. When all NaOH is used sulfuric acid is formed which was observed as very low pH of exhausted samples used in sewage treatment plants [6]. On the other hand, following reactions 1-11, and 17, sulfur must be formed in the system and it does not affect the surface pH.

Slightly different pattern than that on the virgin carbon surface is proposed to occur on the surface of catalytic carbon , Centaur®. This is a very microporous carbon enriched with nitrogen [32]. That nitrogen is likely in the form of pyridinic-like groups. As in the case of sodium, their basicity enhances the dissociation of hydrogen sulfide to HS- ions. Owing to high microprosity of this carbon, that process occurs in the confined space where big sulfur polymers cannot be formed following reaction 4. Thus small sulfur radicals are readily oxidized to sulfur dioxide and further to sulfuric acid. Reaction likely proceeds from small pores to larger until low pH of sulfuric acid suppresses the dissociation of H_2S, which results in the observed breakthrough.

Conclusion

The results presented here show the differences in the performance of various materials as hydrogen sulfide adsorbents. For comparison, only the best commercial materials are used. As demonstrated, the variety of the oxidation products can be found on the surface and the speciation depends on textural and chemical heterogeneity of their surfaces. However, the desired speciation depends on the final application and options of disposal, a good carbonaceous material for H_2S removal should be basic in its nature and have available pore space to store oxidation products.

Acknowledgement. This research was supported by NYC Department of Environmental Protection.

References

(1) http://www.epa.gov/air/caaac/dieselreview.pdf
(2) Stirling, D. *The Sulfur Problem: Cl;eaning up Industrial Feedstocks*, RCS, Cambridge, 2000.
(3) Turk, A.,;Sakalis, S.; Lessuck, J.,; Karamitsos, H.; and Rago, O. *Environ. Sci. Technol.* 1989, **33**, 1242
(4) Stuetz, R. M.,;Fenner, R. M; Engin, G; *Wat. Res.* **1999**, *33*, 453.
(5) Turk, A.,; Sakalis, E.; Rago, O.; Karamitsos, H. *Annals New York. Academy of Sciences* **1992**, *661*, 221
(6) Bandosz, T. J.; Bagreev, A.; Adib, F.; Turk, A. *Environ. Sci. Technol*. **2000**, *34*, 1069.
(7) Bansal, R. C.; Donnet, J. B.; Stoeckli, F. *Active Carbon*: Marcel Dekker: New York, 1988.
(8) Avgul, N.N.; Kiselev, A. V. in *Chemistry and Physics of Carbon*; Walker, P. L., Jr., Ed.; Marcel Dekker: New York, 1970; Vol.6.
(9) Puri, B. R., In *Chemistry and Physics of Carbon*; P.J. Walker, Jr. Ed.; M. Dekker: New York, 1970; Vol. 6, p. 191.
(10) Leon y Leon, C. A., and Radovic, L. R. In *Chemistry and Physics of Carbon*; P.A. Thrower, Ed.; M. Dekker: New York, 1992; Vol. 24., pp. 213-310.
(11) Kaliva, A. N.; Smith, J. W. *Can. J. Chem. Eng.* **1983**, *61*, 208 .
(12) Bandosz, T. J., In *Fundamental of Adsorption 6*, Munier, F., Ed.: Elsevier: Paris 1998; p. 635.
(13) Adib, F.; Bagreev, A.; Bandosz, T. J. *Environ. Sci. Technol***. 2000,** *34*, 686.
(14) Adib, F.; Bagreev, A.; Bandosz, T. J. *J. Coll. Interface Sci*. **1999**, *214*, 407
(15) Adib, F.,; Bagreev, A.; Bandosz, T. J. *J. Coll. Interface Sci.* **1999,** *216*, 360.
(16) Adib, F.; Bagreev, A.; Bandosz, T. J. *Ind.Eng.Chem.Res*. **2000**, *39*, 2439.
(17) Klein, J.; Henning, K-D. *Fuel* **1984**, *63*, 1064.
(18) Hedden, K.,; Humber, L.; Rao, B. R. *VDI-Bericht* **1976**, *37/42*, 253.
(19) Meeyoo, V.; Lee, J. H.; Trimm, D. L.; Cant, N. W. *Catalysis Today* **1998**, *44*, 67.
(20) Meeyoo, V.; Trimm, D. L.; Cant, N. W. *J. Chem. Tech. Biotechnol*. **1997**, *68*, 411.
(21) Coskun, I; Tollefson, E. L..*Can. J. Chem. Eng.* **1986,** *58*, 72.
(22) Ghosh, T. K.; Tollefson, E. L. *Can. J. Chem. Eng.* **1986**, *64*, 960.
(23) Bagreev, A.,Adib, F.; Bandosz, T.J. Carbon, **2001**, 39, 21987.
(24) Choi, J. J.; Hirai, M.; Shoda, M., *App. Catal. A*, **1991**, *79*, 241.
(25) Li, C. T., U. S. *Patent No. 4,196,183*, (1980).
(26) Bagreev, A.; Bandosz, T.J. *Ind. Eng. Chem. Res*. **2002**, *41*, 672.
(27) Przepiorski J.; Oya A. *J Mat Sci Lett* **1998**, *17*, 679-82
(28) Radovic, L.R.; Rodriguez-Reinoso F. In *Chemistry and Physics of Carbon*; Thrower PA, Ed.: M. Dekker; New York, 1997; Vol.25, pp. 243-358.
(29) Salame, I.I.; Bandosz, T.J. *Langmuir* **2000**, *16*, 5435.
(30) Matviya, T. M., Hayden, R. A., *U.S. Patent 5,356,849* (1994).
(31) Hayden, R.A. *U.S. Patent 5,444,081* (1995).
(32) Adib, F.; Bagreev, A.; Bandosz, T. J. *Langmuir* **2000**, *16*, 1980.
(33) Bandosz, T.J. J. *Colloid Interface Sci.* **2002**, *246*, 1.
(34) Bagreev, A., Bandosz, T.J. Carbon, **2001**, *39*, 2303.
(35) Bagreev A.; Bandosz T.J.; Locke DC. *Carbon* **2001**, *39*, 1971.
(36) Bagreev, A.; Bashkova, S.; Locke, D.C.; Bandosz T.J. *Environ. Sci. Technol.* **2001**, *35*, 1537.

(37) Bashkova, S.; Bagreev, A.; Locke, D.C; Bandosz, T.J. Fundamentals of Adsorption -7, Kaneko K, Kanoh H, Hanzawa Y. Eds., IK International, Chiba, Japan, 239-246, 2002
(38) Bagreev, A.; Bandosz, T.J. *Environ. Sc.i Technol* **2004**, *38*, 345.
(39) Graham, J. US Patent No. 60.254,9000 (2004)
(40) ASTM D6646-01.
(41) Lastoskie, Ch. M.; Gubbins, K. E.; Quirke, N., *J. Phys. Chem.* **1993**, 97**,** 4786 ;
(42) Olivier ,J. P.; Conklin, W. B. *Presented at 7th International Conference on Surface and Colloid Science*, Compiegne, France, 1991
(43) ASTM Standards (1998). Vol.15.01. Refractories; Carbon and Graphite Products; Activated Carbon; Advanced Ceramics.
(44) Brennan, J.K.; Bandosz, T.J.; Thomson, K.T.; Gubbins, K.E. *Colloids and Surface A,* **2001**, *187-188*, 539.
(45) Kortum, G.; Vogel, W.; Andrussow, K. In *Dissociation Constants of Organic Acids in Aqueous Solutions*. Butterworth, London, 1961.

DENSITY FUNCTIONAL THEORY STUDY OF CARBON-H_2O REACTIONS DURING GASIFICATION WITH STEAM

Juan F. Espinal,[1] Fanor Mondragón,[1] and Thanh N. Truong[2]

[1] Institute of Chemistry, University of Antioquia
Medellin, Colombia A.A. 1226
[2] Department of Chemistry, University of Utah
Salt Lake City, Utah, USA 84112

Introduction

Carbon gasification is an alternative process to the combustion of coal since it produces less pollution and is more efficient. Basically, carbon gasification is the reaction of carbon with an oxidant agent such as oxygen, steam and/or carbon dioxide. Steam gasification is a process that has been widely studied by experimental techniques. Several mechanisms have been proposed for this reaction.[1-9] However, it is still not clear which of the proposed mechanisms is correct. Furthermore, these mechanisms do not provide any molecular-level details due to the complexity of the system.

In a recent theoretical study of the carbon-H_2O reaction a novel mechanism for the formation of molecular hydrogen was proposed which does not imply dissociation of the water molecule on the surface rather than a rearrangement of the hydrogen atoms.[10] This shows that molecular modeling is a powerful tool for improving our understanding of the gasification process.

The goal of this study is to carry out a Density Functional Theory study of thermodynamics of selected reactions that can take place during the steam gasification process. Particularly, we studied the interaction of the H_2O molecule with the active sites of clean carbonaceous models and possible pathways for the evolution of molecular hydrogen during the carbon-H_2O reaction.

Computational Details

Carbonaceous materials are macrostructures formed mainly by aromatic clusters. For char, it is known from solid-state ^{13}C-NMR experiments that it has structures of randomly connected graphene clusters consisting of 12-25 aromatic carbon atoms (3-7 benzene rings).[11] Since the gasification reactions take place at high temperatures, the active sites are simulated as edge carbon atoms of a graphene layer that have lost a hydrogen atom. In the carbonaceous model used for the calculations the other edge carbon atoms are terminated with hydrogen atoms. It has been reported previously that the use of H to terminate the boundaries of finite graphite models is a good choice.[12] The models shown as the reactants in Figures 1 and 2 are reasonable representations of the active sites environment in zigzag and armchair edges, respectively. Note that the π-bond network is implied in these figures. It is important to note that although the char has a highly condensed aromatic ring structure where the graphene units may have different sizes and orientations, the size of the carbonaceous models used in this study correspond to those suggested from NMR experimental data. In previous investigations it was also shown that the reactivity of a carbon material depends more strongly on the local structure of the active site rather than on the size of the graphene layer.[13,14]

In order to investigate the reaction of steam with the carbonaceous models we fully optimized each structure and some of the complexes that can be formed. All calculations (energies, optimizations, and frequencies) were done at B3LYP Density Functional Theory level (DFT), using the 6-31G(d) basis set for all atoms except for the hydrogen atoms in the water molecule where the 6-31G(d,p) basis set was used. In a previous study it was shown that spin contamination in unrestricted wave function at B3LYP level of theory is small for carbonaceous models.[15] Each model was optimized in its electronic ground state. Question on the roles of the excited states in these reactions is deferred to a separate study. This was done by performing single-point energy calculations at the same level of theory for several electronic states using geometries that were optimized at the AM1 semiempircal method for a given species, the ground state was taken as the one with the lowest energy. Furthermore, frequency calculations were done in order to confirm the stability of the optimized structures. All calculations were done using the Gaussian 98 program.[16]

Results and Discussion

Reaction of Steam with Clean Surfaces. The reaction of steam with the active sites of the carbonaceous models is a highly exothermic reaction either on zigzag or armchair configuration as can be seen in Figures 1 and 2. These reactions involve the production of a hydroxyl group after the dissociative chemisorption of the water molecule. If there is an active site next to the hydroxyl group, the hydrogen atom of this group would potentially further react with that active site to form a semiquinone group, in a reaction that is exothermic on both zigzag and armchair configurations.

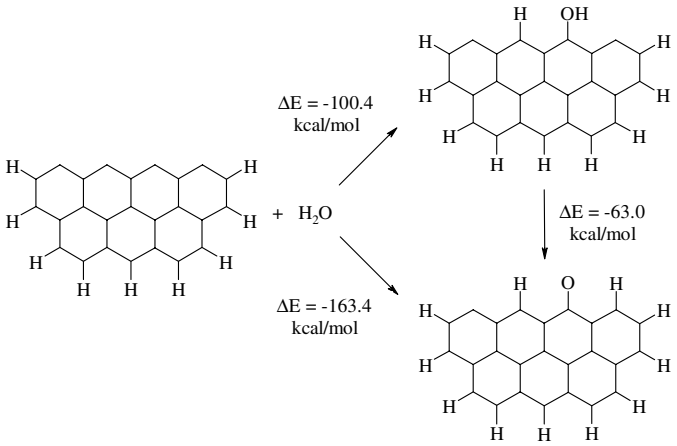

Figure 1. Reaction of the H_2O molecule on the active sites of the clean zigzag model and thermodynamic data.

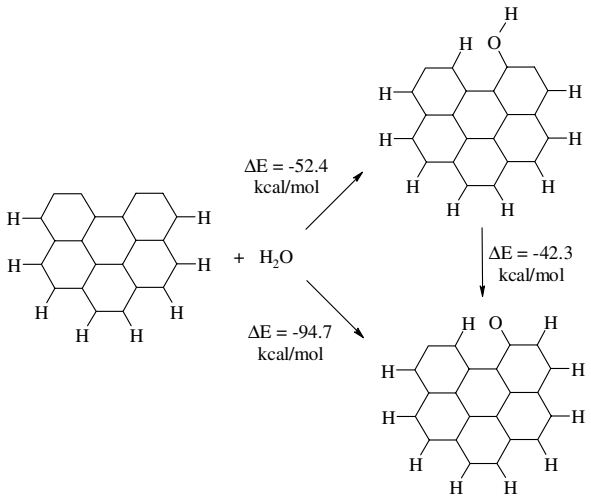

Figure 2. Reaction of the H_2O molecule on the active sites of the clean armchair model and thermodynamic data.

The reactions shown in Figures 1 and 2 are in agreement with the published experimental results where it was reported that after adsorption of water on graphite at low temperatures (25°C) the water molecule is chemisorbed and phenol and carbonyl (semiquinone) groups would be formed.[17] From the data shown, the dissociation of the water molecule at the active sites of carbonaceous materials is a thermodynamically favorable process.

Hydrogen Evolution. We studied several possibilities for the production of molecular hydrogen during the carbon-H_2O reaction on zigzag and armchair configurations. One possible pathway for the evolution of hydrogen is shown in Figure 3.

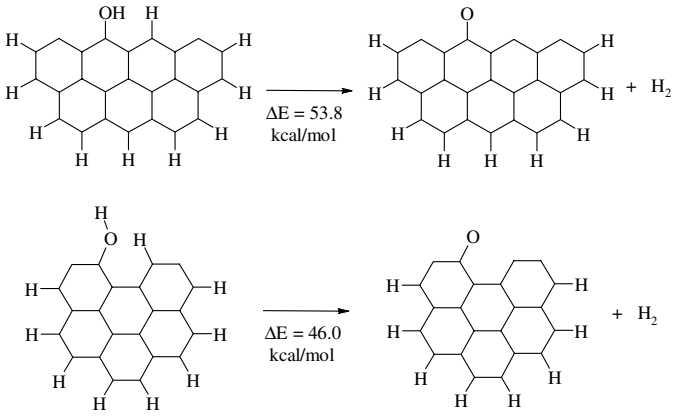

Figure 3. Possible pathways for molecular hydrogen evolution after chemisorption of one water molecule on the carbon surface.

Another route for the evolution of molecular hydrogen is found when two water molecules react on consecutive active sites as shown in Figure 4. From a thermodynamic point of view, the reactions shown in Figure 4 are more favorable ways to produce hydrogen from zigzag and armchair edges.

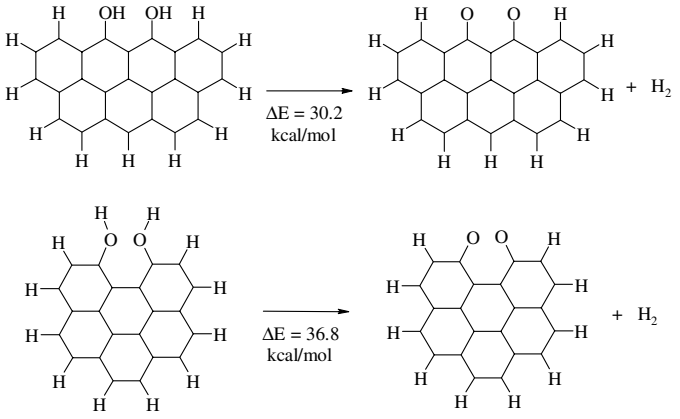

Figure 4. Molecular hydrogen evolution after carbon reaction with two water molecules and thermodynamic data.

The reactions shown in Figure 4 involve the dissociative chemisorption of two water molecules in such a way that two neighbor hydroxyl groups are obtained. These groups are precursors for subsequent hydrogen evolution leaving two semiquinone groups on the surface that could desorb as carbon monoxide or carbon dioxide as the gasification reaction proceeds.[18,19]

Conclusions

The reaction of steam with the active sites of the carbonaceous models is a highly exothermic reaction either on zigzag or armchair configuration. This reaction produces a hydroxyl group after the dissociative chemisorption of the water molecule. We propose an alternative pathway for hydrogen evolution that involves two neighbor hydroxyl groups that are precursors for molecular hydrogen production leaving two semiquinone groups.

Acknowledgements. The authors wish to thank the University of Antioquia for the financial support of the "Sostenibildad 2003" program. JFE acknowledges Colciencias and the University of Antioquia for the PhD. scholarship. We also thank the Center for High Performance Computing at the University of Utah for computer support.

References

(1) Pierce, C.; Smith, R. N.; Wiley, J. W.; Cordes, H. *Journal of the American Chemical Society* **1951**, *73*, 4551.
(2) Johnstone, H. F.; Chen, C. Y.; Scott, D. S. *Industrial and Engineering Chemistry* **1952**, *44*, 1564.
(3) Smith, R. N.; Pierce, C.; Joel, C. D. *Journal of Physical Chemistry* **1954**, *58*, 298.
(4) Giberson, R. C.; Walker, J. P. *Carbon* **1966**, *3*, 521.
(5) Yang, R. T.; Duan, R. Z. *Carbon* **1985**, *23*, 325.
(6) Yang, R. T.; Yang, K. L. *Carbon* **1985**, *23*, 537.
(7) Hermann, G.; Hüttinger, K. J. *Carbon* **1986**, *24*, 705.
(8) Hüttinger, K. J. *Carbon* **1988**, *26*, 79.
(9) Hüttinger, K. J.; Merdes, W. F. *Carbon* **1992**, *30*, 883.
(10) Zhu, Z. H.; Finnerty, J.; Lu, G. Q.; Wilson, M. A.; Yang, R. T. *Energy & Fuels* **2002**, *16*, 847.
(11) Perry, S. T.; Hambly, E. M.; Fletcher, T. H.; Solum, M. S.; Pugmire, R. J. *Proceedings of the Combustion Institute* **2000**, *28*, 2313.
(12) Chen, N.; Yang, R. T. *Carbon* **1998**, *36*, 1061.
(13) Montoya, A.; Truong, T.-T. T.; Mondragón, F.; Truong, T. N. *Journal of Physical Chemistry A* **2001**, *105*, 6757.
(14) Montoya, A.; Mondragón, F.; Truong, T. N. *Carbon* **2002**, *40*, 1863.
(15) Montoya, A.; Truong, T. N.; Sarofim, A. F. *Journal of Physical Chemistry A* **2000**, *104*, 6108.
(16) Frisch, M. J.; Trucks, G. W.; Schlegel, H. B.; Scuseria, G. E.; Robb, M. A.; Cheeseman, J. R.; Zakrzewski, V. G.; J. A. Montgomery, J.; Stratmann, R. E.; Burant, J. C.; Dapprich, S.; Millam, J. M.; Daniels, A. D.; Kudin, K. N.; Strain, M. C.; Farkas, O.; Tomasi, J.; Barone, V.; Cossi, M.; Cammi, R.; Mennucci, B.; Pomelli, C.; Adamo, C.; Clifford, S.; Ochterski, J.; Petersson, G. A.; Ayala, P. Y.; Cui, Q.; Morokuma, K.; Malick, D. K.; Rabuck, A. D.; Raghavachari, K.; Foresman, J. B.; Cioslowski, J.; Ortiz, J. V.; Baboul, A. G.; Stefanov, B. B.; Liu, G.; Liashenko, A.; Piskorz, P.; Komaromi, I.; Gomperts, R.; Martin, R. L.; Fox, D. J.; Keith, T.; Al-Laham, M. A.; Peng, C. Y.; Nanayakkara, A.; Gonzalez, C.; Challacombe, M.; Gill, P. M. W.; Johnson, B.; Chen, W.; Wong, M. W.; Andres, J. L.; Gonzalez, C.; Head-Gordon, M.; Replogle, E. S.; Pople., J. A. Gaussian 98, Revision A.8; Gaussian, Inc.: Pittsburg, PA, 1998.
(17) Miura, K.; Morimoto, T. *Langmuir* **1988**, *4*, 1283.
(18) Espinal, J. F.; Montoya, A.; Mondragón, F.; Truong, T. N. *Journal of Physical Chemistry B* **2004**, *108*, 1003.
(19) Montoya, A.; Mondragón, F.; Truong, T. N. *Journal of Physical Chemistry A* **2002**, *106*, 4236.

SIMULATION & NO_x CORRELATION FOR COAL-FIRED BOILER

Mel Fox and André L. Boehman

The Energy Institute
The Pennsylvania State University
405 Academic Activities Building
University Park, PA 16802

Introduction

Oxides of nitrogen (NO_x) are a major pollutant evolving from combustion processes. Federal emissions regulations are become increasingly stringent, in order to abate harmful NO_x emissions. Some of the proposed NO_x reduction strategies for stationary combustion systems are:

- Combustion modifications
- Reduction technologies (both catalytic and non-catalytic)
- Fuel additives and alternative fuels
- Reburning technologies
- Low-NO_x burners
- Feedback control & monitoring technologies.

Computational Fluid Dynamics (CFD) has been used to simulate combustion for decades. Simulations have been employed to assist in the design of improved burner geometries, the analysis of alternative fuels and reburning conditions, and various other applications. While studies have shown simulated results for NO_x emissions, temperature profiles and flow fields, for given planes within the boiler, no numerical relationships between such data have been determined.

The desire to implement a temperature measurement-based monitoring and feedback control system for improved NO_x control necessitates the discovery of a functional correlation between boiler temperature distributions, boiler operating parameters, and NO_x formation. This numerical simulation effort has the objective of determining how best to implement the temperature profile information that can be obtained with a new fiber optic temperature sensor under development at Penn State University, which can provide a measurement of the temperature distribution along a line-of-site across the interior of a boiler.

The work herein is focused on modeling the "demonstration boiler" at the Energy Institute at PSU. The grid was generated in Gambit 2.1, and a commercial CFD code, FLUENT 6.1, was used for simulation. Tests were designed and data was collected for typical and low-NO_x conditions. Data was collected at several planes within the boiler.

Numerical Modeling Approach

Two different cases were modeled based upon the configuration of the demonstration boiler: a normal case, where primary, secondary and tertiary air flow rates were set at conventional operating conditions; and a low-NOx case, where the secondary air flow rate is decreased and that air flow is redirected to become a tertiary air flow.

Demonstration Boiler. The demonstration boiler, located at Penn State's Energy Institute, is a D-type design watertube boiler, manufactured by Tampella Power Corporation [1].The boiler has approximate dimensions (in meters) of 2.65x1.83x2.59. It is rated for 15,000 lb/h steam (@300 psig), and was initially designed for fuel oil-firing, but has since been modified for coal-based fuels.

The three-dimensional, nonuniform grid of the demonstration boiler is shown in Figure 1. The grid was meshed at a spacing of 3, and comprises nearly 273,000 nodes.

Numerical Model. The solutions were obtained using an implicit, segregated solver, for non-premixed, steady state combustion. The *k*-ε model was employed as the turbulence model for this work, which is widely used combustion modeling [2].

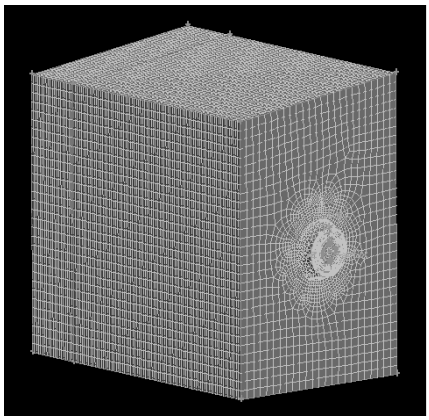

Figure 1. Three-dimensional demonstration boiler grid

The turbulent intensity is a function of the upstream flow conditions. The mixture fraction/PDF formulation, which was developed specifically to model turbulent diffusion flames [3], was used to model the combusting flow, along with the P-1 radiation model and NO_x postprocessor. Chemical equilibrium relates instantaneous mass fractions and temperature with the mixture fraction. The P-1 radiation model is advantageous due to its simple diffusion equation, which allows particulate scattering [4] and requires low CPU demand. The mixture fraction method permits intermediates, dissociation effects, and coupling between turbulence and chemistry to be accurately accounted for. A probability density function (PDF) accounts for the interaction of turbulence and chemistry [3], simulating realistic finite chemistry in turbulent flames. The density-weighted time-averaged Navier Stokes equations are solved for temperature, velocity, species concentrations and variance, from which the time-averaged NO formation rate is computed at each point, using the averaged flow-field information [3, 5]. Since the rate of NO_x formation is sensitive to temperature, the combustion solution must be highly accurate to attain reasonable results.

A Rosin-Rammler distribution was assumed for the coal particle size distribution. The particles were injected at four positions, for a total mass flow rate of coal of 0.37 kg/s. The air was injected according to Table 1.

Solutions are calculated based on the conservation equations. The continuity equation is:

$$\frac{\partial \rho}{\partial t} + \frac{\partial}{\partial x_j}(\rho u_j) = 0 \qquad (1)$$

The turbulent flow conservation equations for momentum and energy are as follows, respectively:

$$\frac{\partial}{\partial t}(\rho u_i) + \frac{\partial}{\partial x_j}(\rho u_i u_j) = -\frac{\partial p}{\partial x_i} + \frac{\partial \tau_{ij}}{\partial x_j} \qquad (2)$$

$$\frac{\partial}{\partial t}(\rho h_t) + \frac{\partial}{\partial x_j}(\rho u_j h_t) = \frac{\partial p}{\partial t} + \frac{\partial}{\partial x_j}(u_i \tau_{ij} - q_i) \quad (3)$$

Table 1. Inlet and Outlet Conditions for Both Cases

	Normal	Low-NO_x
Inlet Conditions		
Primary Air Flow Rate (kg/s)	0.2	0.20
Secondary Air Flow Rate (kg/s)	0.53	0.76
Tertiary Air Flow Rate (kg/s)	1.23	1.00
Fuel Flow Rate (kg/s)	0.37	0.37
Outlet Conditions		
Area Weighted Ave. T (K)	1712.72	1456.16
Area weighted Ave. NOx (ppm)	397.31	283.81

Results & Discussion

Calculations were performed for the conventional and low-NOx cases, from which temperature and NOx distributions were generated.

Figure 2 and **Figure 3** portray various temperature gradients over the specified surfaces. At conventional operating conditions, the elevated temperatures are indicative of coal particles trapped in recirculating flow regions, depleting available oxygen, and hence yielding significant NOx formation with adequate residence time. In the low-NOx case with air-staging, high temperature zones are fuel-rich and therefore lead to higher CO production. Though the temperature and residence time may be conducive to NOx formation, the depleted oxygen reduces net NOx formation. Successful air staging provides significant stratification of the combustion process, and thermal non-uniformity, as shown in the low-NOx case temperature profile, which indicates the extent of stratification.

Statistical Analysis. Data, in the form of 1D "lines" of information (simulating the data to be collected from the fiber-optic sensor, spanning the boiler), resulting from CFD calculations will be analyzed statistically in order to determine a correlation.

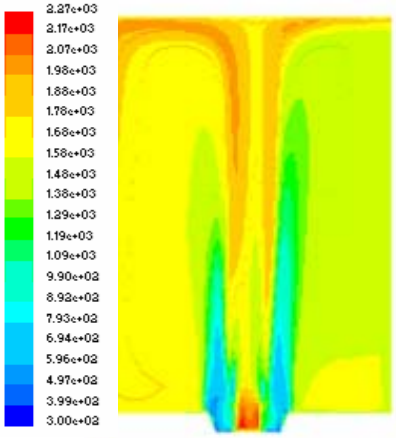

Figure 2. Low-NOx case temperature profile (axial surface)

Regression studies will be employed for the conventional and low-NOx cases. A series of regressions will be performed for each scenario, with NOx concentration held as the response variable, while predictor variables comprise T, velocities and other stoichiometric parameters in various combinations. The combination providing the best (highest) R-squared value for each case will be accepted and used in a regression study comparing the two cases.

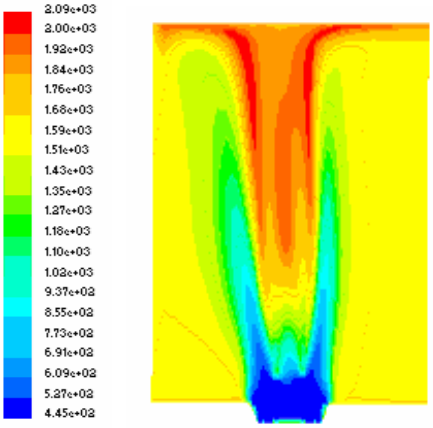

Figure 3. Conventional case temperature profile (axial surface)

Conclusions

Two separate calculations were performed with secondary and tertiary air flow rates as the only variables. The temperature profiles presented for each case provide evidence that data from a one dimensional sensor spanning a boiler in strategic locations may provide pertinent information to allow real-time NOx control.

Temperature, NOx concentrations and velocity profiles were collected for specified planes within the boiler. These parameters will be compared against one another via statistical analysis, in order to determine an algorithm for implementation in a NOx control system, in conjunction with a fiberoptic, in-situ temperature sensor.

Acknowledgements. This paper was written with support of the University Coal Research program of the U.S. Department of Energy, National Energy Technology Laboratory under contract no. DE-FG26-02NT41532. The Government reserves for itself and others acting on its behalf a royalty-free, nonexclusive, irrevocable, worldwide license for Governmental purposes to publish, distribute, translate, duplicate, exhibit, and perform this copyrighted paper.

References

1. The Energy Institute., *Demonstration Boiler Fact Sheet*, www.energy.psu.edu.
2. Launder, B.E et al, *The Numerical Computation of Turbulent Flows.* Computer Methods in Applied Mechanics and Engineering, 1974. **3**: p. 269-289.
3. Fluent Inc., *User's Guide*. 1996, Fluent Incorporated: Lebanon. p. 19-43.
4. S.S. Sazhin et al., *Modelling of the Gas to Fuel Droplets.* Fuel, 2000. **79**(14): p. 1843-1852.
5. Fluent Inc., *Fluent 6.1 Documentation*. 2003, Fluent Incorporated: Lebanon.

DIMETHYL ETHER OXIDATION AT ELEVATED TEMPERATURES

Claudette M. Rosado-Reyes, and Joseph S. Francisco

Department of Chemistry and
Department of Earth and Atmospheric Sciences
Purdue University
West Lafayette, IN 47907

Joseph J. Szente, and M. Matti Maricq

Research Laboratory
Ford Motor Company, P.O. Box 2053, Drop 3083
Dearborn, MI 48121

Introduction

The fact that current diesel engine emissions will not meet future standards, has spurred research into alternative fuels in order to reduce emissions without compromising fuel economy. Oxygenated hydrocarbons such as ethers have been proposed for use as alternative fuels or as additives in diesel engines[1]. The chemical and thermodynamic properties of dimethyl ether (DME) make it ideal for this purpose: higher cetane number of 55-60[2], lower self ignition temperatures, NO_x emissions and engine noise[3], and no soot formation. The determination of alternative fuels emissions under operating conditions (high pressure and temperature) is required to assess the impact of these materials on the atmospheric reactivity of tailpipe emissions[4].

The use of DME as a fuel for solid oxide fuel cells (SOFCs) has also been under consideration[5]. There are potential applications for its use in vehicle based fuel cells. Direct oxidation of hydrocarbons eliminates the need for fuel reformers and can reduce the cost and weight of SOFC systems. The temperature dependence of DME thermal decomposition is important in determining the power output of SOFCs and their contamination by coking.

Under laboratory conditions, chlorine atoms - produced by the photolysis of Cl_2 - initiate the chemistry. Methoxymethyl radicals (CH_3OCH_2) are produced as a result of the abstraction of a methyl hydrogen from DME. Under high O_2 concentrations, methoxymethyl radicals combine with oxygen to produce methoxymethyl peroxy radicals ($CH_3OCH_2O_2$). Previous product studies of chlorine initiated chemistry at low temperature showed a dependence on total pressure, where production of formaldehyde and methyl formate compete against each other[6]. This pressure dependence was explained by proposing and showing that the oxidation of dimethyl ether proceeds via two different competitive pathways: a pressure dependent and a pressure independent pathway.

In the pressure dependent pathway, the energetically excited peroxy (RO_2*) is collisionally deactivated into a stabilized peroxy radical that can continue reacting by usual peroxy radical reactions. From these methoxymethyl peroxy radical reactions, methyl formate ($CH_3OC(O)H$) is formed as a main by-product. Also a significant yield of formic acid (HC(O)OH) has been previously reported[7], although it is not clear how the proposed mechanism can account for it. The pressure independent pathway takes place via the intramolecular rearrangement of peroxy radical followed by dissociation into two molecules of formaldehyde and one molecule of hydroxyl radicals (2 HC(O)H + OH). This pressure independent pathway is of particular interest with respect to combustion because OH radicals are an important reactive intermediate in combustion processes. The production of hydroxyl radicals can initiate and sustain a chain reaction between DME and OH. The original study of the dimethyl ether photoinitiated chemistry intended to determine the branching ratio of $CH_3OCH_2 + O_2$ reaction with respect to pressure[6]. Time-resolved UV/IR spectroscopy was utilized to perform real time kinetic measurements of this reaction at temperatures between 230 and 350 K, pressures between 10 and 200 Torr, and a time regime of up to 60 microseconds. At room temperature, the peroxy radical stabilization becomes more significant as pressure increases, but the dissociation pathway becomes insignificant to sustain combustion chain reactions. As the temperature increases the reaction shifts to the formaldehyde production, but this change is not as significant as the one dependent on pressure. The investigation of the kinetics of the photo-initiated $CH_3OCH_2 + O_2$ chemistry at elevated temperatures above 295 K revealed thermally induced reactions taking place independent of photolysis. Also these results raised the possibility that at even higher temperatures >350K, the dissociation channel might become significant enough to sustain DME + OH chain reaction, and be even more significant near or at combustion temperatures. This study intends to determine the branching for the $CH_3OCH_2 + O_2$ reaction pathways at pressures of 20-200 Torr and temperatures of 295-700 K, and the importance of dimethyl ether degradation in the presence of O_2 over the temperature range of 295-700 K.

Experimental

To investigate the temperature dependence on the degradation of dimethyl ether and consequently on the $CH_3OCH_2 + O_2$ branching ratio, the kinetics of the reaction of $CH_3OCH_3 + Cl_2$ in the presence of O_2 is being studied at elevated temperatures. Flash Photolysis/Transient Infrared Spectroscopy is used to evaluate the yield and kinetics of Formaldehyde, Methyl Formate, and Formic Acid, at the 1709 cm^{-1}, 1742 cm^{-1}, 1791 cm^{-1} vibrational lines respectively. The measurements include the direct probing of product concentration for the first 900 μsec after Cl_2 photolysis, and in the absence of Cl, at three different dimethyl ether concentrations (6, 12, 20 × 10^{16} molecules/cm^3). These experiments were carried out at three different total pressures (60, 250, 600 × 10^{16} molecules/cm^3) and eight different temperatures between 295 and 700 K (increments of 50K).

The Flash Photolysis/Time-Resolved IR Spectroscopy experimental apparatus is described as follows. A reagent gas mixture is inserted into a quartz cylindrical reaction cell. The gas mixtures for these experiments consisted of dimethyl ether (1-7 Torr), 4.8% chlorine/N_2 (2-11 Torr), O_2 (11-38 Torr), and N_2 to make up the balance. The reaction cell is wrapped with electrical heaters and insulated for thermal stability. Temperature is monitored and controlled by thermocouples positioned along the outside of the cell. The gases are pre-heated prior to entering the cell. Photo-dissociation of Cl_2 is initiated by 351 nm light from a Lambda Physik model LPX 301 excimer laser. Two dichroic beam-steering mirrors, placed at opposite ends of the reaction cell, reflect the UV laser light into the reaction cell while allowing the transmission of IR light. Conditions were such that the reaction cell was well evacuated and the gas mixture replenished between laser pulses. A high-resolution, cryogenically cooled, Pb-salt diode laser is used as the infrared light source to probe the ro-vibrational carbonyl stretch mode of by-products at frequencies between 1700 and 1800 cm^{-1}. After passing though a mode selecting monochromator, it is directed through the reaction cell where it counterpropagates relative to the excimer laser. The IR light is focused to a LN_2 cooled HgCdTe detector with a response time of 0.3 μsec. Frequency drift is prevented by frequency locking the laser radiation to the ro-vibrational absorption line being monitored. The IR light intensity is measured for several milliseconds following the laser photolysis pulse to obtain time

dependent absorbances. In order to quantify the concentrations of the by-products, their IR absorption cross sections (σ) at the respective IR absorbance lines are determined by introducing a known amount of by-product into the reaction cell of pathlength l. The concentration is then calculated by Beer's Law via,

$$c(t) = \left(\frac{1}{l\sigma}\right)\ln\left(\frac{I_0}{I}\right)$$

The initial halogen radical concentration from photolysis is calculated indirectly by substituting methanol for DME and measuring the formaldehyde yield from the photoinitiated oxidation reaction.

Results and Discussion

For the thermally induced chemistry measurements, the gas mixture of $DME/O_2/N_2$ was allowed to equilibrate to the selected temperature while flowing through the cell. Residence time in the cell was between 2 and 4 seconds. Figure 1 shows the formaldehyde yield, in the absence of chlorine, relative to dimethyl ether initial concentrations at temperatures between 295K and 700K. At temperatures between 450K and 500K, dimethyl ether thermally-induced oxidation is starting to take place. Above these temperatures, main by-products are being produced reaching maximum concentrations between 600K and 650K, starting then to decline. At low pressure conditions, formaldehyde yield is lower compared to medium and high pressure conditions. The change in formaldehyde yield is not significant going from 250×10^{16}/cm^3 to 650×10^{16}/cm^3 total pressure. Methyl formate and formic acid yields follow a similar trend, although formaldehyde yield is greater by a factor of 2 and 10 respectively. Figure 1 clearly shows a total pressure dependency as a function of temperature in the methoxymethyl peroxy radical chemistry, but also shows that the formaldehyde yield is independent of DME initial concentration.

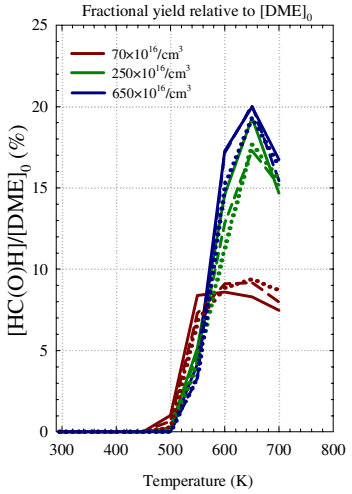

Figure 1. Formaldehyde yield relative to dimethyl ether initial concentration in the temperature regime of 295-700K at three different total pressure conditions.

Figures 2 and 3 show the pressure dependent yields of the three main by-products from photo-initiated DME oxidation experiments at 295K and 500K respectively. Due to the high initial radical concentrations, > 10^{14}/cm^3, for these measurements, the products are monitored for only a few milliseconds after the chemistry is initiated by chlorine atoms. At a given temperature, the formation of formaldehyde shows pressure dependence due to the change in the fraction of peroxy radicals that undergo dissociation. In contrast, methyl formate yield remains essentially the same over this pressure range. No detectable levels of formic acid are measured during the first few milliseconds of the reaction.

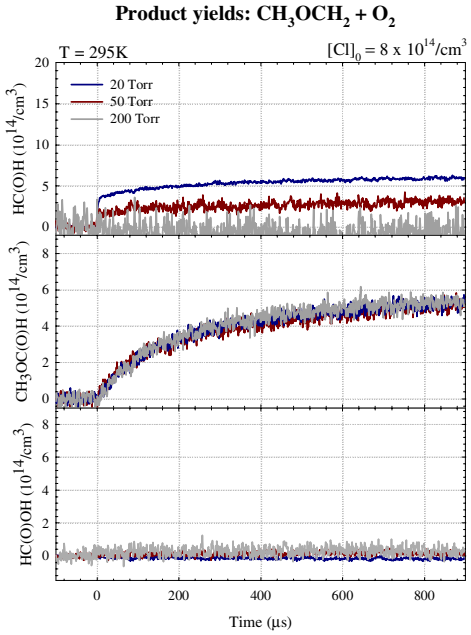

Figure 2. Formaldehyde, methyl formate, and formic acid concentration vs time profile from Cl_2-initiated DME degradation at room temperature as a function of pressure.

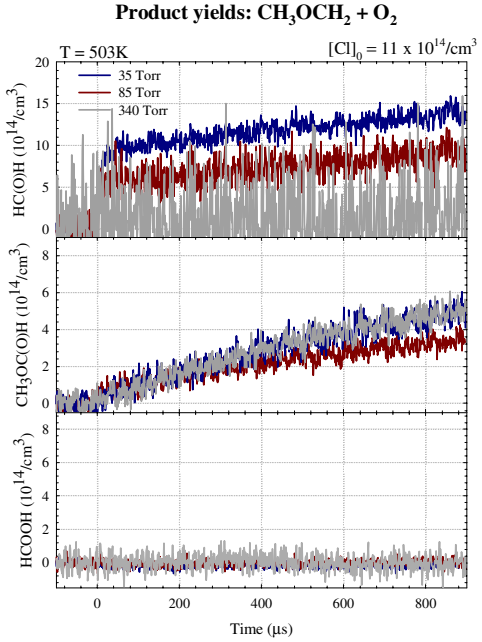

Figure 3. Formaldehyde, methyl formate, and formic acid concentration vs time profile from Cl_2-initiated DME degradation at 503K as a function of pressure.

As the temperature is raised from 295K to 503K, the formaldehyde yield increases, by as much as a factor of 3, with the

greatest increase occuring at low pressures, and becoming less at the higher pressure. As total pressure is increased, IR detection of the products becomes increasingly difficult due to both the smaller product concentrations and the pressure broadening effect on absorbance cross section. While the methyl formate yield reaches similar levels at both temperatures, the rate of formation is slower as temperature increases.

A reaction mechanism for the oxidation of DME is being used to predict the temperature and pressure dependence of the methoxymethyl peroxy stabilization vs. dissociation branching ratio as well as the peroxy radical self reaction rate constant. The methoxymethyl peroxy radical chemistry will be further described by Lindemann and Arrhenius analysis of these parameters.

References

1. Leppard, W. R.; *SAE Trans*., **1991**, 912313.
2. Kapus, P. E.; Cartellieri, W. P.; *SAE Trans*., 1995, 952754.
3. Roubi, M. A,; *Chem. Eng. News*, **1995**, 44, 37.
4. Japar, S. M.; Wallington, T.J.; Richert, J. F. O.; Ball, J. C.; *Int. J. Chem. Kinet*., 1990, 22, 1257.
5. Murray, E. P.; Harris, S. J.; Jen, H; *J. Electrochem. Soc.*, **2002**, 149, A1127.
6. Maricq, M. M.; Szente, J. J.; Hybl, J. D.; *J. Phys. Chem. A*. **1997**, 101, 5155.
7. Liu, I.; Cant, N. W.; Bromly, J. H.; Barnes, F. J.; Nelson, P. F.; Haynes, B. S.; Chemosphere, **2001**, 42, 583.

Simulation Study of CO2 Separation Process by Using Hollow Fiber Membrane

Dae-Hwan Lee, Hyung-Taek Kim

Dept. of Energy Studies, Ajou University
Wonchon-dong Yeongtong-gu
Suwon, Korea 443-749

Introduction

In accordance with the Kyoto Protocol and consecutive several international agreements, Korea must prepare for the duty of the reduction of CO_2 emission. Most of the CO_2 absorption/separation processes are energy–consuming so that optimum arrangement of CO_2 absorption system should be acquired through the simulation. In the present investigation, membrane separation process with hollow fiber is simulated to find an optimum design/operation parameter for low energy-consuming one.

The membrane separation of CO_2 requires relative low energy consumption comparing to absorption or distillation type. It can be operated easily and inexpensively since its physical separation mechanism. Also it is suitable to apply in a small-to-medium scale of CO_2 separation process. Therefore, system models for the CO_2 separation process is set up by using the membrane separator then the CO_2 separation process is simulated with changing the parameter of operation condition, separation characteristics by changing the shape of mixed membrane, and etc. The optimum conditions for the CO_2 separation process are obtained by analyzing the design and operation parameters when energy requirement is the lowest.

Methods

Simulation of 1 membrane module is initially made by using the FORTRAN program. After that using these results, 4 bundles of membrane module connected with cascade type is also simulated. During the simulation, operation/design parameters are calculated such as required membrane area, number of modules, permeated CO_2 concentration and the amount of permeated gas with no recycle streams. Finally, recycle mode of membrane simulation is proceeded by using the FORTRAN.

Simulation for 1 module. Simulation of 1 membrane module is conducted with the overall material balance equation is below:

$$(\alpha-1)y_i^2+\left(1-\alpha-\frac{1}{R}-\frac{x(\alpha-1)}{R}\right)y_i+\frac{\alpha x}{R}=0 \qquad \cdots(1)$$

$$A=\frac{(Vy)_{out}}{(J_A)_{out}}=\frac{(Vy)_{out}}{Q_A(P_1x-P_2y_i)_{ave}}$$

$$=\frac{(Vy)_{out}}{Permeate\ flux\times(x-Ry_i)_{ave}} \qquad \cdots(2)$$

α : selectivity

x : Feed composition

y_i: Permeate composition

P_1: Feed Pressure

P_2: Permeate Pressure

R : Pressure ratio(P_2/P_1)

V : Permeate rate

Flow diagram of 1 membrane module simulation is illustrated in **Figure.1**. Several parameters such as operating pressure are varied during the simulation as in **Table. 1**. Different methods of simulation are utilized in the current study. One method is fixing x_t for 0.01, in which x_t represents the retentate composition of CO_2. Then it is calculated that required membrane area, number of required modules, flow rate, and CO_2 concentration of permeate. Another method is fixing number of total modules as 50, then flow rate, CO_2 concentration of permeate, and x_t are calculated.

Table 1. Input Parameters

parameter	amount	parameter	amount
P_1	6 atm	No of HF per module	5000
P_2	0.1 atm	Feed rate	1000 m^3/day
Selectivity	20	Length of HF	50 cm
Permeability	20	Pressure ratio	P_2/P_1

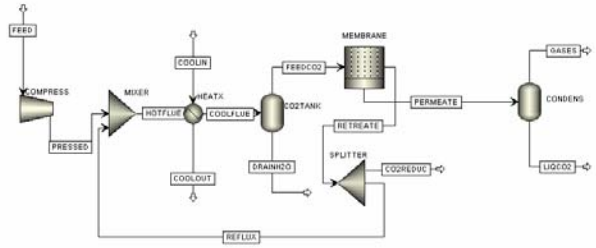

Figure 1. Overall Flow diagram

Simulation for 4 bundles of membrane without recycles. Flow diagram of 4 bundles of membrane module is composed like a cascade in **Figure. 2**. From the simulation, calculated results are illustrated as required membrane area, number of required modules for each bundles, total required membrane area, flow rate and CO_2 concentration of permeate with no recycle streams.

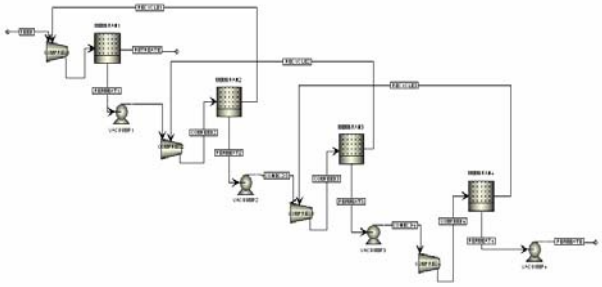

Figure 2. 4 bundles of membrane

Simulation for 4 bundles of membrane with recycles. Simulation with recycle streams is conducted as below. Since the simulation is 4 bundles of membrane module with recycles, calculation is iterated 10 times. It is calculated that required membrane area, number of required modules for each bundle, total required membrane area, number of total required module, flow rate, and CO_2 concentration of permeate.

Results and Discussion

Simulation for 1 module

1. Fixing x_t for 0.01

The result is below in **Table. 2**:

Table 2. Result at fixing x_t for 0.01

parameter	amount
Required membrane area	241.016 m^2
No of required modules	76.72 77
Flow rate of permeate	10.144 m^3/hr
CO_2 concentration of permeate	37.967 %

It is simulated during changing the pressure.

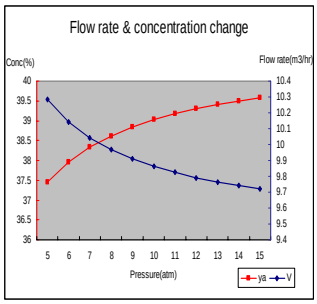

Figure 3. Flow rate & CO_2 concentration change

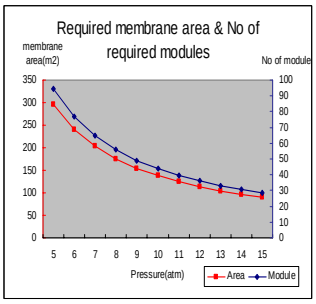

Figure 4. Required membrane area & No of required modules

2. Fixing No of modules for 50
The result is below in **Table. 3**:

Table 3. Result at fixing No of modules for 50

parameter	amount
Flow rate of permeate	6.202 m^3/hr
CO_2 concentration of permeate	48.467 %
x_t	0.0327

It is simulated during changing the No of modules.

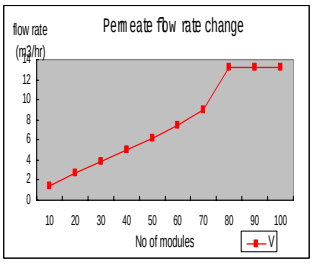

Figure 5. Permeate flow rate change

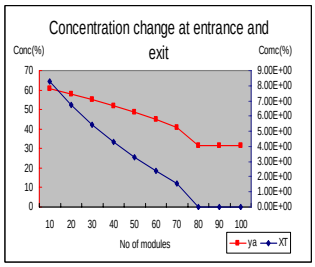

Figure 6. Concentration change at entrance & exit

Simulation for 4 bundles of membrane without recycles. It is calculated that required membrane area & No required of modules for each bundle, total required membrane area & No of required module and flow rate & CO_2 concentration of permeate with no recycles.

Table 3. Result of 4 bundles of membrane without recycles

Parameter	amount
Required membrane area(1stage)	237.016 m^2
No of required modules(1stage)	75.49 76
Required membrane area(2stage)	53.795 m^2
No of required modules(2stage)	17.12 18
Required membrane area(3stage)	22.884 m^2
No of required modules(3stage)	7.28 8
Required membrane area(4stage)	16.018 m^2
No of required modules(4stage)	5.10 6
Required membrane area(total)	329.857 m^2
No of required modules(total)	108
No of required HF(total)	540000
Feed flow rate	41.667 m^3/hr
Flow rate of permeate	2.4718 m^3/hr
CO_2 concentration of permeate	93.329 %

Simulation for 4 bundles of membrane with recycles. It is calculated that required membrane area & No required of modules for each bundle, total required membrane area & No of required module and flow rate & CO_2 concentration of permeate with recycles.

Parameter	amount
Required membrane area(1stage)	275.448 m^2
No of required modules(1stage)	87.68 88
Required membrane area(2stage)	50.111 m^2
No of required modules(2stage)	15.95 16
Required membrane area(3stage)	17.660 m^2
No of required modules(3stage)	5.62 6
Required membrane area(4stage)	10.107 m^2
No of required modules(4stage)	3.22 4
Required membrane area(total)	353.326 m^2
No of required modules(total)	114
No of required HF(total)	570000
Feed flow rate	41.667 m^3/hr
Flow rate of permeate	2.8708 m^3/hr
CO_2 concentration of permeate	93.866 %

Table 4. Result of 4 bundles of membrane with recycles

Calculation is iterated 10 times. The result is below in **Figure. 7** & **Figure. 8**.

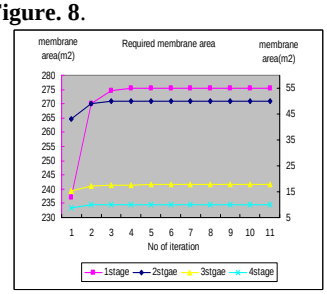

Figure 7. Required membrane area

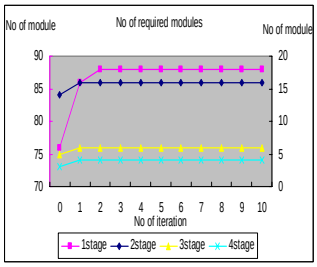

Figure 8. No of modules

Conclusions

When there are recycles, flow rate & CO_2 concentration of permeate are increased about 0.4m^3/hr and 0.53%. Required membrane area & No of required modules at 1st stage are increased. But, required membrane area & No of required modules at other stage are decreased. Total required membrane area & total No of required modules is increased. Total No of required modules is increased about 6 modules.

These results indicate that we can remove more CO_2 and get the high CO_2 concentration. If more bundles are attached, the separation units by using the hollow fiber membrane remove more CO_2 and get the high CO_2 concentration. Therefore, it is very useful that CO_2 separation process by using the hollow fiber membrane.

References

(1) James Marriott; Eva Sorensen; *Chemical Engineering Science 58*, **2003**, 4975-4990.
(2) R. Wang; S. L. Liu; T. T. Lin; T. S. Chung; *Chemical Engineering Science 57*, **2002**, 967-976.
(3) Li Xu; Lin Zhang; Huanlin Chen; *Desalination 148*, **2002**, 309-313.
(4) G. C. Kapantaidakis; G. H. Koops; *Journal of Membrane Science 204*, **2002**, 153-171.

NUMERICAL SIMULATION OF VOLATILES RELEASE FOR MICRONIZED COAL REBURNINIG

Manyin Hu[1], Hezhong Tian[2], Zhong Liu[1], Xiaomin Wang[1]

1. School of Environmental Science and Engineering, North China Electric Power University, Baoding 071003, China
2. Department of Environmental Science and Engineering, Tsinghua University, Beijing 100084, China

1. Introduction

Micronized coal reburning is an effective and promising technology in NO_X emission control of coal-fired utility boilers. NO_X is reduced in two routes with coal reburning: one is the homogenous reaction between NO_X and volatiles under fuel-rich conditions, and the other is the heterogenous reaction between NO_X and char which formed after coal pyrolysis. More NO_X can be reduced if more volatiles release from coal pyrolysis[1-3], and the corresponding char has higher reactivity also[4, 5].

Coal is composed of various functional groups. In the heating process, with the increase of temperature, various bonds between coal molecules destroy and produce volatiles through complex reactions, the volatiles release into gas phase through char pores[6]. Volatiles mainly include CH_4, C_2H_4, C_3H_6, H_2, CO, CO_2 and tar, in which C_nH_m, HCN, NH_3, H_2 and CO can react with NO. Heating rate has important influence on volatiles release during coal pyrolysis, and volatiles especially hydrocarbons release and the release rate directly affect NO reduction. Further, heating rate have effects on char structures and inner face activity points, as well as various reactions rates.

Mathematical simulation is one of the important ways to study coal pyrolysis. Volatiles release under reburning conditions in an entrained flow reactor (EFR) was mathematically simulated, in which coal less than 100 mesh and 320 mesh were used as reburning fuels, respectively. The total volatiles release and various volatiles release rates were calculated, also the effects on NO reduction were analyzed.

2. Mathematical models

2.1 Energy conversation equations

The flow in EFR is laminar. In this study, heterogenous energy transfer is determined by heat exchange and radiate heat transfer, while energy transfer between reaction system and furnace wall is determined by convective and radiate heat transfer. Pulverized coals flux is relatively smaller (about 20% of total fuel) under reburning conditions, excess air coefficient is less than 1, coal particles can not combust completely in reburning zone, the dispatch between heat absorbed and emitted--total reactive caloric is far less than other heat transfers. Therefore, reactive caloric, as well as the gas productions is omitted.

Gas phase energy conversation equation is expressed as follows:

$$\frac{d(Q_g C_{pg} T_g)}{dL} = N_v A[\frac{\lambda_g}{r_{ps}}(T_s - T_g) + \varepsilon_g \sigma(T_s^4 - T_g^4)]4\pi r_{ps}^2 + [\varepsilon_g \sigma(T_w^4 - T_g^4) + h_c(T_w - T_g)]\pi D \quad (1)$$

While, solids phase energy conversation equation is:

$$\frac{d(W_s C_{ps} T_s)}{dL} = N_v A[\frac{\lambda_g}{r_{ps}}(T_g - T_s) + \varepsilon_s \sigma(T_g^4 - T_s^4) + \varepsilon_s \sigma(T_w^4 - T_s^4)]4\pi r_{ps}^2 \quad (2)$$

For using time differential equation, the following equation:

$$dt = \frac{A}{Q_V} dL \quad (3)$$

can be used to convert energy conversation equations to time differential format. Therefore, with the above energy conversation equations, temperature fields in furnace as well as volatiles release can be calculated.

2.2 Volatiles release chemical mechanism models

According to chemical kinetic theory, in the reaction chains of one species, reactions with lower activation energies have higher reaction rate; while reactions with higher activation energies have lower reaction rate. Elementary reactions that have higher activation energy are controlling steps on the whole chain. In this study, coal pyrolysis models developed by Suubergand Solomon is simplified, and N pyrolysis models are complemented, then coal rapid pyrolysis models under reburning conditions is deduced(detail omitted for length limitation).

2.3 Volatiles release kinetics models

Coal pyrolysis productions mainly include CH_4, C_2H_4, C_2H_6, H_2, CO, CO_2, tar, HCN, and NH_i. In order to simplify the models, it is supposed secondary devolatilization take place after tar formed, and part of the species converts to gas volatiles, the remain is char. Volatiles release models of David Merrick[7] are adopted in calculations. Hydrocarbons higher than ethane are dealt with 'ethane equivalent', while gaseous nitrogen is dealt with 'ammonia equivalent'. Double-C hydrocarbons consist of C_2H_4 and C_2H_6, and ammonia equivalent are consist of NH_3 and HCN. According to the experiential data, C_2H_4: C_2H_6 is 1:7, and NH_3: HCN is 1:1.

The approach adopted to predict the final yields of the volatile matters is to establish a set of 9 simultaneous linear equations with the final masses of tar and eight volatiles as variables. These equations can be expressed as followings:

$$\sum_{j=0}^{9} A_{ij}\overline{m}_j = b_i \qquad i = 1,\cdots 9 \quad (4)$$

Where: A_{ij} is a matrix of constants; $\overline{m}_j$ are the final yields (as mass fractions of coal $_{daf}$) of CH_4, C_2H_6, CO, CO_2, H_2, H_2O, NH_3, HCN and tar; b_i is a vector of constants. Therefore, the final yields of volatiles can be figured out with these equations.

Volatiles release rates can be figured with the following equation:

$$\frac{dV_j}{dt} = K_j(V_j^* - V_j) \quad (5)$$

Where: V_j is the final yield of species j at time t (as mass fractions of coal $_{daf}$); V_j^* is the V_j at the time of $t\to\infty$, and these have been figured out through the above matrix; K_j is the reaction rate constant and comply with Arrhenius law.

$$K_j = A_j \exp(-E_j / RT) \quad (6)$$

A_j and E_j of different reactions for creating CH_4, C_2H_6, CO, CO_2, H_2, H_2O and NH_3 are showed in Table 2. With equation (6), volatiles release rates and volatiles yields at different times can be calculated.

3. Calculating parameters

Mathematical models are developed on the basis of an experimental EFR with standard 1600×φ60mm. Flue gas temperature in furnace is 1300℃. Inlet flue gas temperature is 20℃, and flux is 1.83m^3/h. pulverized coal flux is 1.457g/min□the relative reburning fuel fraction is 25%.

Table 1 Physical parameters adopted in calculation

Physical parameters	Formulations	References
Gas phase specific heat, C_{pg}	(0.9986+9.3*E*-5*(T_g-273))*29	[8]
Solid phase specific heat, C_{ps}	$0.222+2.18\times10^{-4}\times T_s$ $9741.666/T_s^2$	[9]
Solid darkness, Gas darkness	0.9□0.149	[10]
Gas heat transfer coefficient ($kWm^{-1}K^{-1}$)	$57\times10^{-6}\times[(T_s+T_g)/1600]\times0.75$	[11]
Temperature of inlet flue gas and coal	20℃	Measured
Tube wall temperature□flue gas flux	1300℃, 10.1736m^3/h	Measured

The entrained flow is divided into some time differential segments with 0.001s. Physical parameters used in calculation are showed in Table 1 and Table 2, respectively.

Table 2 Results of coal and char analysis

Items		Coal less than 100 mesh	Coal less than 320 mesh	Char less than 100 mesh	Char less than 320 mesh
Ultimate analysis (%)	C_{ad}	66.01	65.11	76.76	75.53
	H_{ad}	4.361	4.056	0.618	0.223
	O_{ad}	17.3	17.44	8.701	8.137
	N_{ad}	0.824	0.71	0.796	0.745
	S_{ad}	0.552	0.59	0.964	0.717
Proximate analysis (%)	A_{ad}	12.7	13.9	19.33	21.36
	W_{ad}	5.2	5.3	1.76	0.5
	V_{ad}	29.2	27.8	3.53	0.72

4. Results and discussion

Using the above models and parameters, the heating rate and volatiles release of coal particles that less than 100 mesh and 320 mesh, are calculated under the conditions of NO reduction with 25% reburning fuel fraction in 1300℃ EFR.

4.1 Simulation of coal particles heating rate

Fig.1 shows the simulation results of the heating rate of two sizes of coal particles during coal reburning.

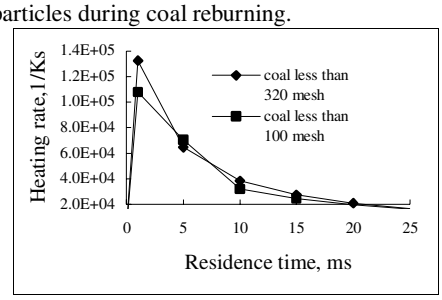

Fig.1 Simulation results of coal particles heating rate

As can be seen from Fig.1, the heating rates of two sizes of coal are all higher than 105K/s, and the heating rate of coal less than 320 mesh is obviously higher than that of coal less than 100 mesh. This implies that finer coals has higher heating rate under the same conditions, and finer coal can attain higher temperature in shorter time. At the same time, finer coal has better burning and burnout capability, which is in favor of boiler economically operation.

4.2 Simulation results of volatiles final yields

Total various volatiles final yields are showed in Fig. 2.

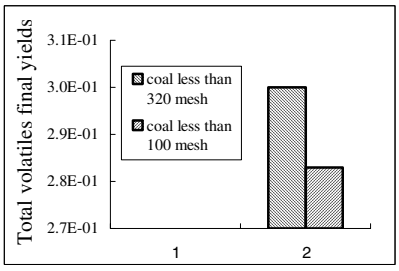

Fig. 2 Total volatiles yields of two sizes of micronized coals

It can be seen that the total volatiles final yields of coals less than 320 mesh is higher than that of coals less than 100 mesh.

Simulation results of coals heating rate show that finer coal has higher heating rate, and coal pyrolysis is more completely, also more volatiles are released. On one hand, C_mH_n, HCN and NH_3 are the main species to realize NO homogeneous reduction. More volatiles can reduce more NO. On the other hand, because finer coal achieves higher temperature in the same time, the corresponding char can also attain higher temperature and higher reaction rate to reduce NO.

4.3 Simulation results of volatiles release

Nine volatiles yields at different time are calculated. As an example, volatiles yields of C_iH_j and HCN at different time are showed in Fig. 3 and 4, respectively.

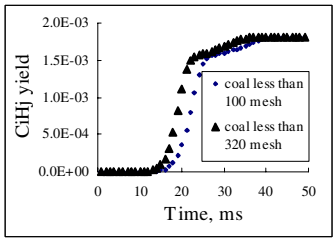

Fig.3 C_iH_j yield at different time

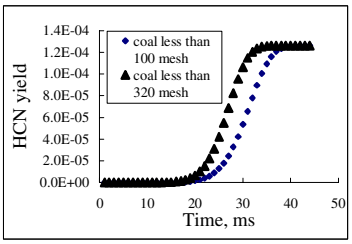

Fig. 4 HCN yield at different time

Fig.3 and Fig.4 show that volatiles release earlier from finer coal, and Fig.1 show that finer coal has higher heating rate. Finer coal attained higher temperature in the same time, so finer coal starts to devolatilize earlier, and coal devolatilize more acutely and completely.

Various volatiles almost release completely in 50ms. CO_2 has the highest release rate, and almost release completely in 18ms, then CH_4 in 28ms, and C_2H_4, CO, HCN, H, NH_3 in 40ms, C_2H_6 has the lowest release rate, and almost release completely in 47ms. This is because that the destruction of bonds that produce CO_2 needs less activation energy than that produce C_2H_6.

5. Conclusions

1-demension mathematical models based on an EFR laminar flow are developed. Then, the heating rate and volatiles release for different size of coals during NO reduction with coal reburning in an EFR are simulated and analyzed in detail. It is demonstrated that finer coal has higher heating rate and begin to devolatilize earlier, coal pyrolysis is more completely, and more volatiles are released.

With finer coal as reburning fuel, NO emission can be reduced and coal particles burning and burnout capabilities are improved. This benefits boilers economically operation. Therefore, micronized coal is better as reburning fuel than conventional pulverized coal.

References

1. Smart J P, Morgan D J. Fuel, **1994**, 73(9):1437-1442
2. Kicherer A, et al. Fuel, **1994**, 73(9):1443-1446
3. Zhong B.J., et al. J. of Eng. Thermo. **2000**, 21(3):383-387
4. Liu Z., et al. Proceedings of the CSEE, **2003**, 23(10):204-208
5. Zhong B.J., et al. J. of Combust. Sci. & Tech., **2001**, 7(2):116-119
6. Juntgen H. Fuel, **1987**, 63: 731-737
7. Merrick D. Fuel, **1983**, 62: 534-539
8. Shen W.D., et al. Engineering Thermodynamics. Beijing: higher education press, 1988
9. Perry R. H. and Gree W. D. 'Perry' s Chemical Engineers 'Handbook', 6th Ed. McGraw-Hill, New York, 1984
10. Vamvuka D., et al. Fuel, **1995**, 74: 1452-1460
11. Gururajan V. S., et al. Combust. Flame, **1988**, 72: 1-12

THE LAB-SCALE SORBENT INJECTION TESTING ON MERCURY CAPTURE WITH FOLLOW-UP SOLID-GAS MIXTURE

Yan Cao, Kunlei Liu, Xin Liu, Hongmin Yang, John T. Riley and Wei-Ping Pan*

Institute for Combustion Science and Environmental Technology (ICSET)
Western Kentucky University, Bowling Green, KY 42101
Email: yan.cao@wku.edu,

Introduction

The DOE prefers the retrofitting of dry sorbent injection upstream of either an ESP or an fabric filter baghouse to further control mercury emission in coal-fired power plants.[1] This promising technology has the widest potential application for controlling mercury emissions in plants that are not equipped with FGD scrubbers, which includes 75% of all U.S. plants. However, unlike the successful carbon injection for mercury control in waste incinerators, which produces one or two orders of magnitude lower mercury emissions, sorbent injection used in coal-fired utility boiler faces many challenges. Large quantities of PAC must be injected, leading to high costs if high removal efficiency is required.[2] In this study, two new highly effective, low-cost mercury sorbents including IGCC char and woodceramic will be used to inject in the simulated duct in a lab-scale facility with a low pressure drop turbulence mixer to enhance the mass transfer of mercury capture process.

Experimental

At ICSET of WKU, a lab-scale demonstration facility on sorbent injection was setup to evaluate the some promising sorbents behavior on Hg capture efficiency. The lab-scale facility was designed and attempted to simulate real injection and reaction process inside the duct under the power plant conditions, the brief diagram is presented in Figure 1. It consists of a reactor pipe, ash free probe, Venture flow meter and educator. The educator was used to generator a vacuum at the end of system and intake flue gas into the system. A venture flow meter was used to measure the flow rate of gas inside the reactor. The concentrated Hg generated by Cavkit as well as sorbent were injected in the front of reactor. Two ash free probes were used to make sure no sorbent was sucked out of the system which might buildup a filter cake in the gas sampling process and adversely affecting the mercury reading on semi-continuous mercury monitor (SCMM). Mercury concentration changes through the system were monitored by SCEM. At system exit, a cotton trap was used for capture of used sorbent. The system was fully insulated to maintain the desired temperature range which is about 120-150 ^{o}C.

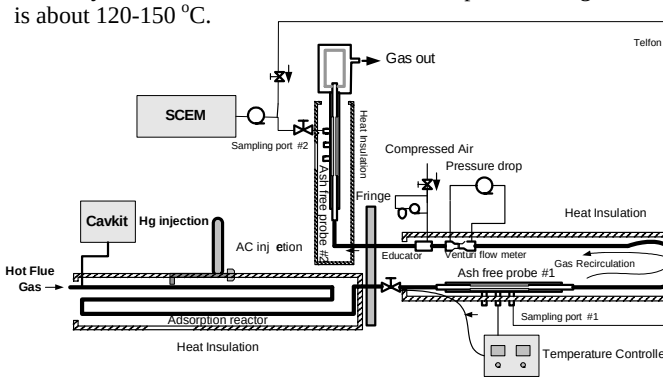

Figure 1. The Lab-Scale Testing Facility for Sorbent Injection Testing

Results and Discussion

The preliminary testing results using ceramics sorbents from chicken waste were shown in Figure 2. The testing was conducted at stack locations with two utility boilers with capacity of 165 and 450MWe, respectively. It was found that the mercury concentration in the flue gas at the outlet of the sorbent trap decreased dramatically when the sorbent was deployed.

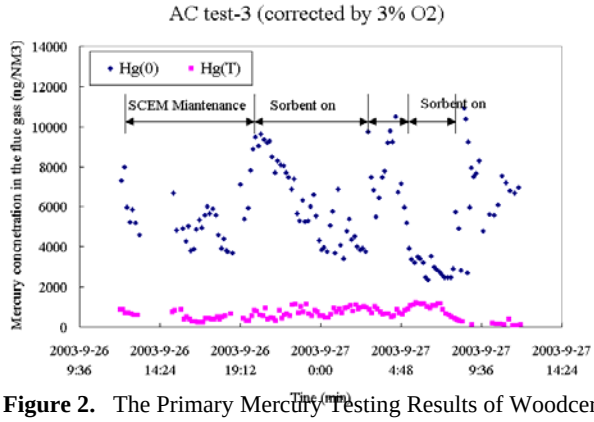

Figure 2. The Primary Mercury Testing Results of Woodceramics Prepared by WKU

The testing results of four sorbent injections showed that the maximum Hg removal efficiency of Eastern IGCC char could be as high as 78% using the S/Hg injection ratio of 12000 at a lower temperature (20 ^{o}C) and shorter residence time (0.13 s) as shown in Figure 3. The Hg removal efficiency of Eastern IGCC char decreases greatly (27%) after removal of the fine constitutes (< 45 um). To simulate the flue gas and ash under turbulent conditions inside the adsorption reactor, sorbent mixed with baked ash was used in the following tests. Eastern IGCC with medium sized particle diameter (100<dp<250um) was used, yielding 30% mercury removal efficiency at a lower carbon injection ratio (S/Hg: 1200). For Polk IGCC char with a similar particle size (100<dp<250um), about 60% mercury removal efficiency was reached at a higher carbon injection ratio (S/Hg: 12000) and a shorter residence time (0.13 s). For Woodcermics, less mercury removal efficiency was found at lower injection ratios, using a longer sorbent residence time. Increasing the injection ratio to 37000, an 80% mercury removal efficiency was found at 50 ^{o}C. Increasing the temperature to 104 ^{o}C and decreasing the injection ratio to 12000, greatly decreased the woodceramics mercury removal efficiency. The mercury removal efficiency decrease for all sorbents in the lab-scale demonstration testing was due to the lower gas velocity used (3m/s) which was far smaller than the actual flue gas velocity in a power plant. A smaller gas velocity decreases the turbulent gas flow rate and thus decreases the contact efficiency of sorbent and mercury in the flue gas.

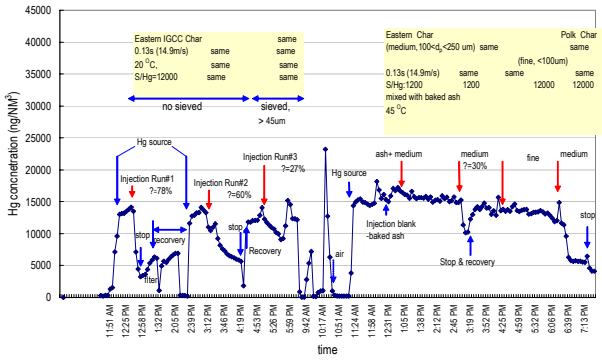

Figure 3. Mercury Removal Behavior Using IGCC Char.

Inserting an obstacle inside the adsorption reactor increased the mercury removal efficiency in the lab-scale demonstration testing. Considering the fact that the sorbent absorption rate is largely dependent on the contact efficiency of sorbent and mercury in the flue gas, a new designed Turbulence Generator was designed and used in the sorbent injection tests to strengthen gas-solid contacting efficiency. As shown in Figure 4., the elemental mercury removal efficiency by Polk IGCC char could reach 46% with Turbulence Generator adding in compared with 20% without the Turbulence Generator, a net increase of 26% at conditions of sorbent injection ratio of 3000, temperature of 120 ^{0}C and residence time of 3.5 s. As Eastern IGCC char injected in at same conditions, the elemental mercury removal efficiency increased only 5%. That means the Turbulence Generator does work on mercury removal, however, is also dependent on absorption capability of sorbent.

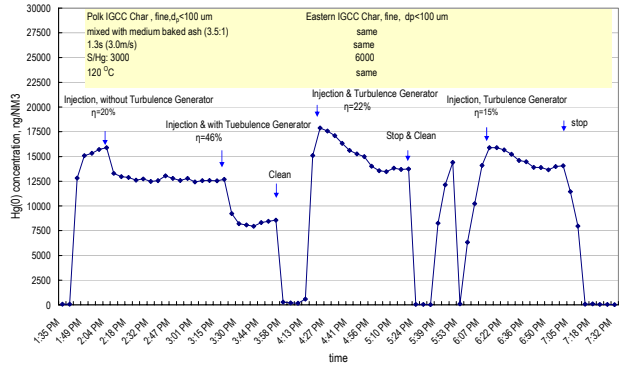

Figure 4. The effect of Turbulence Generator on mercury removal efficiency

Conclusions

At ICSET of WKU, a lab-scale demonstration facility on sorbent injection was setup to evaluate the some promising sorbents behavior on Hg capture efficiency including two type woodceramic sorbents and two types of IGCC chars. The mercury removal efficiency decrease for all sorbents in the lab-scale demonstration testing was due to the lower gas velocity used (3m/s) which was far smaller than the actual flue gas velocity in a power plant. A smaller gas velocity decreases the turbulent gas flow rate and thus decreases the contact efficiency of sorbent and mercury in the flue gas. After using turbulence mixer, even at a lower sorbent injection ratio (S/Hg: 3000) and a shorter residence time (1.3s), 69% mercury removal efficiency was achieved for Eastern IGCC char. Inserting an obstacle inside the adsorption reactor increased the mercury removal efficiency in the lab-scale demonstration testing.

References

1. Solicitation for Financial Assistance Application, DE-PS26-03NT41718, “Large Scale Mercury Control Technology Field Testing Program – Phase II”, DOE-NETL, **2003.**
2. Pavlish, J.H., Sondreal, E.A., Mann, M.D., Olson, E.S., Galbreath, K.C., Laudal, D.L., Benson, S.A., Fuel Processing Technology **2003**; 82:89-165.

NITROGEN ENRICHED ACTIVATED CARBONS AS ADSORBENTS AND CATALYSTS IN DESULFURIZATION TECHNOLOGIES

Andrey Bagreev [1], Svetlana Bashkova [2], Teresa Bandosz [1,2], Angel Menendez [3], Irina Dukhno [4], Yuriy Tarasenko [4]

[1] Department of Chemistry, The City College of New York
[2] The Graduate School of the City University of New York, New York, NY, USA
[3] Instituto National Del Carbon, INCAR (CSIC), Oviedo, Spain
[4] Institute for Sorption and Problems of Endoecology, Kiev, Ukraine

Introduction

Activated carbons (ACs) are widely used as adsorbents and catalysts in desulfurization technologies. Among AC applications in desulfurization are air purification from hydrogen sulfide and methyl mercaptan from waste water treatment plants [1-2], sulfur dioxide removal from flue gases [3-6], and deep desulfurization of gaseous fuel in fuel cell power plants [7]. Desulfurization efficiency is significantly improved when AC works not only as adsorbent of sulfur containing species, but also as a catalyst for selective oxidation of these compounds to less volatile ones which are then strongly adsorbed on a carbon surface. The catalytic properties can be improved by incorporation of nitrogen into the carbon matrix. This process results in an increase in the carbon basicity and polarity. Moreover, dramatic changes in catalytic properties of AC in electron transfer reactions take place.

The objective of this paper is to investigate the ability of nitrogen-containing AC for working as an oxidation catalyst and adsorbent for deep air purification from H_2S, CH_3SH and SO_2.

Experimental

Materials. Nitrogen enriched activated carbons were prepared by impregnation of carbons of different origins with melamine or urea followed by high-temperature treatment (HTT) in inert atmosphere at 850-950^{o}C. Among the precursors for nitrogen immobilization the following carbons were used: bituminous coal based carbons SBC (INCAR, Spain) and BPL (Calgon), wood based commercial carbon BAX-1500 (Westvaco) and experimental EBC (INCAR), as well as experimental fruit stone based carbon KAU (ISPE, Ukraine). Other series of ACs were prepared by pyrolysis of ion-exchange resin containing methylpyridinium and pyridinic nitrogen groups (SCN) and a porous styrene-divinylbenzene copolymer containing no hetero-elements (SCS). The nitrogen modification procedures were described in details elsewhere [8-11]. For comparison the results obtained on commercial catalytic carbon containing nitrogen, Centaur (Calgon), are also discussed. After nitrogen modification the additional letter U (urea) or M (melamine) are added to the names of the carbons. The exhausted carbons after the breakthrough tests are referred to with an additional letter, E.

Methods. The dynamic tests were carried out at room temperature to evaluate the capacity of the ACs for H_2S, CH_3SH and SO_2 removal [8-11]. Moist air (relative humidity 80% at 25^{o}C) containing 3000 ppm of H_2S, CH_3SH or SO_2 was passed through a column with 6 ml of adsorbent at 500 ml/min. The outlet concentrations of gases were monitored with electrochemical sensors. The tests were stopped at the breakthrough concentrations of 500 ppm for H_2S, 50 ppm for CH_3SH and 350 ppm for SO_2. The adsorption capacities of each carbon were calculated by integration of the area above the breakthrough curve (from the inlet concentration of gas, flow rate, breakthrough time), and carbon weight.

Sorption of nitrogen was used to characterize the porosity of adsorbents. Nitrogen isotherms were measured using an ASAP 2010 (Micromeritics) at -196 ^{o}C. Before experiments the samples were outgassed overnight at 120^{o}C under the vacuum of 10^{-5} Torr to a constant pressure. The isotherms were used to calculate the total specific surface areas (S_t), micropore volumes (V_{mic}), total pore volumes (V_t), average micropore sizes (L_{mic}) and pore size distributions using Density Functional Theory (DFT).

pH of carbon surface for initial and exhausted samples was estimated by placing 0.4g of carbon powder in 20 ml of water. The suspension was equilibrated during night and then its pH was measured. The amount of acidic and basic surface groups was determined by titration, with either 0.05N NaOH or 0.05N HCL.

In order to evaluate either the species present on the initial carbon surface or surface reaction products, thermal analysis was carried out using TA Instruments Thermal Analyzer. The instrument settings were: a heating rate of 10^{o}C/min in a nitrogen atmosphere, 100 ml/min flow rate. The products of CH_3SH oxidation were studied by GC/MS on Shimadzu GAS Chromatograph/Mass Spectrometer model QP5050 with XTI-5 column. The samples for GC/MS analysis were extracted from exhausted carbon samples using methanol.

The content of carbon, hydrogen, nitrogen, sulfur and oxygen was analyzed by LECO CNHS-932 and VTF900 instruments. In some cases XRF and EDX methods were used to determine the amount of sulfur adsorbed and the presence of metal impurities. The surface chemistry of nitrogen containing carbons was studied by XPS method (LEYBOLD LHS 11). The values of binding energy were calibrated with respect to C1s peak at 285.0 eV. The N1s envelopes were used to characterize different forms of nitrogen [12].

Results and Discussion

Modification of ACs with melamine and urea resulted in a significant increase in the nitrogen content (Table 1). Introduction of nitrogen also leads to changes in the surface chemistry of carbons. Indeed, after nitrogen doping all carbons became more basic than the initial counterparts, which is reflected as a rise of surface pH, absolute amount of basic functional groups and a relative carbon basicity expressed as a ratio of the number of basic groups to the total number of groups present on the surface.

Table 1. Nitrogen Content, pH of Carbon and Amount of Basic and Acidic Goups

Sample	N content %wt.	pH	Amount of groups, mmol/g		
			basic	acidic	basic/total
SBC	1.0	9.1	0.05	0.5	0.09
SBC-M	5.4	9.2	0.72	0.11	0.87
BPL	0.4	7.4	0.40	0.50	0.44
BPL-U	1.1	8.5	0.60	0.35	0.63
BPL-M	6.8	8.0	0.68	0.24	0.74
BAX	0.2	7.2	0.35	0.90	0.28
BAX-U	3.1	7.4	0.65	0.70	0.48
SCS	0	8.1	0.62	0.12	0.84
SCN	2.4	9.1	0.56	0.25	0.69

The development of nitrogen functionality for different types of nitrogen enriched carbon was extensively studied by X-ray photoelectron spectroscopy (XPS) [12-15]. It was found that the type of a carbon precursor and nitrogen modification agent result in the same surface functionalities when the treatment is done at

temperatures higher then 850°C [4,6,12-15]. During HTT of nitrogen-containing precursors, nitrogen atoms are incorporated into carbon rings and located at the edges of graphene layers as pyridinic (BE = 398.7 ev), pyrrolic (BE = 400.3 ev) and pyridone (BE = 400.5 eV), or in the interior as "quaternary" nitrogen (BE = 401.3 eV). When carbons are exposed to oxygen containing atmosphere the pyridine–N-oxides (BE= 403-405 eV) are formed. It is interesting to note that the energy state of "quaternary" nitrogen observed in N-carbons is very close to the state of real quaternary nitrogen in methylpyridinium group ($>N^+$-CH_3) of vinylpyridine resin - precursor used for preparation of polymeric carbon SCN type [12]. The pyridinic nitrogen contributes to one p_π-electron to the graphitic π-system, while pyrrolic and "quaternary"nitrogen contributes to two p_π-electrons to the graphitic π-system. These extra electrons delocalized over graphene layers can dramatically change catalytic properties of a carbon matrix in reactions involving electron transfer.

Modifications with nitrogen-containing species may also result in changes in the porous structure. For all initial and N-modified carbon samples the nitrogen adsorption isotherms were measured and then structural parameters were calculated [8-11]. All adsorbents have highly developed micro- and mesopore structure. The examples of the results are presented in Table 2. For majority of the samples after N-modification and HTT a 10 to 25% decrease in textural parameters is observed (Table 2). An exemption is the BAX-U sample whose precursor carbon (BAX) was prepared by chemical activation at 550 °C.

Table 2. Structural Parameters of Carbons Calculated from Nitrogen Adsorption Isotherms

Sample	S_t m^2/g	V_t cm^3/g	V_{mic} cm^3/g	L_{mic} nm
BPL	1000	0.71	0.40	1.16
BPL-U	883	0.67	0.34	1.17
BPL-M	811	0.70	0.31	1.19
BAX	1350	1.29	0.50	1.32
BAX-U	1087	0.80	0.40	1.15
SCN	973	0.83	0.43	1.07

The ability of N-containing ACs to work as oxidation catalyst and adsorbents for deep air purification from H_2S, CH_3SH and SO_2 was investigated in dynamic conditions. From the breakthrough curves the capacities for removal of sulfur-containing gases were calculated [8-11]. Examples of data for selected samples are collected in Table 3. In all cases a significant increase in the capacity is found for N-containing carbons compared to the initial ones, which suggests the feasibility of application of N-enriched ACs in desulfurization technologies [8-11].

Table 3.Amount of Gases Adsorbed and the pH of the Carbons

Sample	H_2S ads/pHE mmol/g	CH_3SH ads/pHE mmol/g	SO_2 ads/pHE mmol/g
SBC	0.74/4.4	6.17/4.7	-
SBC-M	7.44/2.0	7.92/3.5	-
BPL	0.12/7.9	2.50/6.9	-
BPL-M	10.1/1.8	9.19/3.7	-
BAX	0.26/4.2	0.58/6.8	0.53/2.2
BAX-U	7.94/2.0	6.25/4.9	1.09/1.9
SCS	0.76/3.9	-	0.84/2.3
SCN	5.88/1.4	9.38/2.9	4.95/1.3
Centaur	3.06	1.5	2.56

The process of SO_2 adsorption/oxidation has been studied extensively and such parameters as the porosity, surface chemistry, ash content and gas phase composition were taken into consideration [2-5,10,14-15]. It was found that in oxygen atmosphere and in the presence of water, SO_2 is adsorbed on the surface of AC, then oxidized to SO_3 by oxygen radicals and after hydration with adsorbed water it is condensed in pores as H_2SO_4 [2-5,10]. The presence of nitrogen-containing functional groups significantly enhances the adsorption capacity due to activation of molecular oxygen and creation additional basic sites for adsorption of oxidation products in molecular or ionic form. Figure 1 demonstrates the dependence of SO_2 adsorption measured in wet, dry and dry anaerobic conditions on the incremental basicity of surface in pores with sizes between 6.8 and 8.6 Å. The graph indicates that both the pore structure and surface chemistry are very important factors which should be taken into account in designing highly effective SO_2 adsorbents.

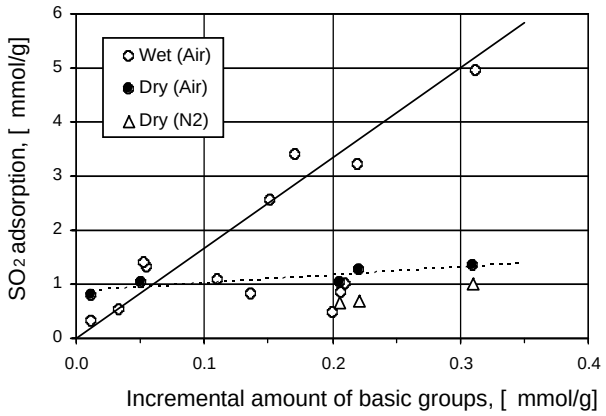

Figure 1. Dependence of SO_2 adsorption on the incremental basicity of surface in pores with sizes 6.8 and 8.6 Å. Lines show the trend in the data.

Caustic impregnated and virgin activated carbons are among most effective adsorbents for H_2S removal from different gas media at low temperatures [1-2]. It was found that presence of water and basic environment on ACs contributes to the dissociation of H_2S and facilitates its oxidation to sulfur and sulfur dioxide [1-2,8]. The proposed mechanism involves H_2S adsorption on the carbon surface, its dissolution in a water film, dissociation of adsorbed H_2S in the water film, surface reaction with adsorbed oxygen with formation of elemental sulfur or SO_2, and further oxidation of SO_2 to H_2SO_4 [1-2]. It was proposed that two types of active sites are probably responsible for catalytic action: one is the carbon active sites where molecular oxygen is adsorbed and activated, and the second ones are the small sulfur clusters or polysulfides where oxygen can also be chemisorbed. The oxidation products are adsorbed in carbon micropores. The reaction proceeds until all micropores or carbon active sites are filled with adsorbed sulfur or until low pH of oxidation products suppresses dissociation of H_2S.

The main feature of H_2S adsorption on N-containing ACs is its deeper oxidation (low pH of exhausted carbon) and higher removal capacity then on carbons without nitrogen (Table 3) [8,9]. To identify the products of H_2S adsorption/oxidation, thermal analysis in nitrogen was performed on the exhausted carbons. The results are presented as DTG curves with three main peaks (Fig. 2). First peak at 100°C represents desorption of water, second peak at 250°C is assigned to desorption of SO_2 and decomposition of H_2SO_4, and the third one at 400-450°C is related to the removal of elemental sulfur. From these data the selectivity for SO_2 oxidation was calculated as the molar ratio of SO_2 formed to total amount of sulfur adsorbed.

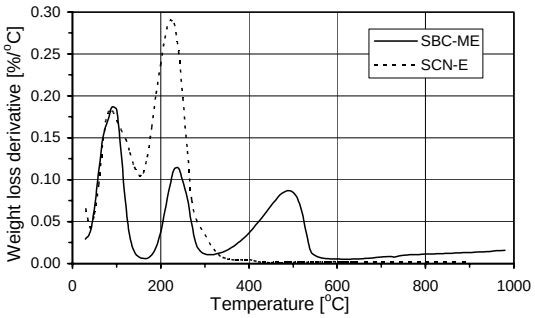

Figure 2. DTG curves in nitrogen for the samples after H_2S adsorption

To see the effect of nitrogen incorporation, the normalized capacity (with respect to the surface area of adsorbents) and selectivity for SO_2 oxidation was plotted versus the ratio of atomic content of nitrogen to carbon determined from elemental analysis (Fig. 3). Four series of N-modified carbons were chosen for this analysis. The results follow, in general, the same tend. While the specific capacity increases until the plateau is formed (saturation), the selectivity changes in the opposite direction. This is likely due to a limited accessibility of oxygen to sulfur active sites in the bulky crystals.

Adsorption/catalytic removal of methyl mercaptan on N-enriched activated carbons follows in general the same trend as the adsorption of hydrogen sulfide. The process is pH dependent and enhanced in the presence of water and oxidation proceeds due to the surface reaction between adsorbed CH_3SH and active oxygen radicals. N-dopping improves the catalytic activity. The oxidation products are adsorbed in carbon micropores [11,16]. In spite of these similarities CH_3SH adsorption has specific peculiarities: due to less water solubility and smaller dissociation constant the oxidation requires more basic conditions. Owing to higher bond energy in S-C then in S-H the reaction proceeds to dimethyl disulfide and methyl methanethiosulfonate formation at room temperature. Water and dimethyl disulfide compete for adsorption sites on the carbon surface. The dependence of the normalized CH_3SH breakthrough capacity on the N/C atomic ratio has the maximum in the capacity at N/C content of about 2% [11,16].

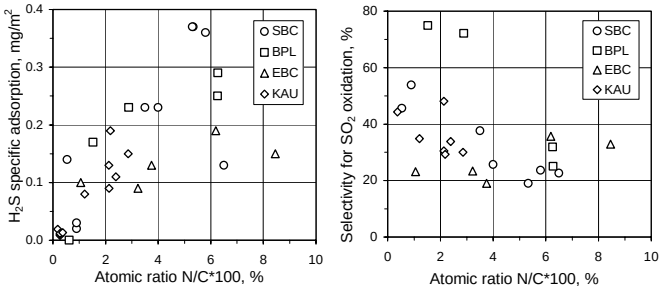

Figure 3. Dependence of the normalized H_2S breakthrough capacity (A) and the selectivity for SO_2 oxidation (B) on the N/C atomic ratio in the carbon matrices.

The observed improvement of adsorption-catalytic properties of nitrogen containing carbons in desulfurization reactions can be explained from the point of view of the electronic theory of catalysis. The extra π-electrons of pyrollic and quaternary nitrogen occupy the high-energy states in the conduction band. It is likely that from there they can be transferred to the adsorbed oxygen and superoxide ions O_2^- can be formed. Those superoxide ions can easily trigger the formation of OH* and HO_2* radicals in reaction with water. All of these species are much more reactive then molecular oxygen and may oxidize described above sulfur compounds, when they are adsorbed on carbon surface.

Conclusions

Nitrogen enriched activated carbons can be successfully used in desulfurization technologies to remove hydrogen sulfide, sulfur dioxide and methyl mercaptan from wet air at ambient temperatures. Nitrogen incorporation has a positive effect on adsorption capacities for all gases studied. Unique surface chemistry of these materials can dramatically change catalytic properties of a carbon matrix in reactions involving electron transfer.

Acknowledgement This research was supported by NATO Collaborative Linkage grant NATO EST CLG 978688.

References

(1) Bandosz, T.J.; *J. Colloid. Interface Sci*., **2002**,*246*,1.
(2) Bagreev, A.; Adib, F.; Bandosz, T.J.; *Carbon*, **2001**, *39*, 1897-1905.
(3) Mochida, I.; Korai, Y.; Shirahama, M.; Kawano, S.; Hada, T.; Seo, Y.; Yoshikawa, M.; Yasutake, A.; *Carbon*, **2000**, *38*, 227.
(4) Li, K.; Ling, L.; Lu, C.; Qiao, W.; Liu, Z.; Liu, L.; Mochida I.; *Carbon*, **2001**, *39*,1803.
(5) Raymondo-Pinero, E.; Cazorla-Amoros, D.; Salinas-Martinez de Lecea, C.; Linares-Solano, A.; *Carbon*, **2000**, *38*, 335.
(6) Raymondo-Pinero, E.; Cazorla-Amoros, D.; Linares-Solano, A.; *Carbon*, **2003**, *41*, 1925.
(7) Gardner, T.H.; Berry, D.A.; Lyons, K.D.; Beer, S.K.; *Fuel*, **2002,** *81*,2157.
(8) Adib, F.; Bagreev, A.; Bandosz, T.J.; *Langmuir*, **2000**, *16*, 1980.
(9) Bagreev, A.; Menendez, J.A.; Duhno, I.; Tarasenko, Y.; Bandosz, T.J.; *Carbon*, **2004**, *42*, 469.
(10) Bagreev, A.; Bashkova, S.; Bandosz, T.J.; *Langmuir*, **2002**, *18*, 1257.
(11) Bashkova, S.; Bagreev, A.; Bandosz, T.J.; *Langmuir*, **2003**, *19*, 6115.
(12) Lahaye, J.; Nanse, G.; Bagreev, A.; Strelko, V. ; *Carbon*, **1999**, *37*, 585.
(13) Pels, J.R.; Kaptejn, F.; Moulijn, J.A.; Zhu, Q.; Thomas, K.M.; *Carbon,* **1995**, *33*, 1641.
(14) Boudou, J.P. ; *Carbon*, **2003**, *41*,1955.
(15) Boudou, J.P.; Chehimi, M.; Simieniewska, T.; Bimer, J. ; *Carbon,* **2003**, *41*,1999.
(16) Bagreev, A.;Bashkova, S.; Bandosz, T.J. ; *Langmuir*, **2002,** *18*, 8553.

USE OF MACERAL CONTENT TO CHARACTERIZE STEAM COAL PERFORMANCE

Jane Chen[1], Shi Su[2] and, John H. Pohl[3]

1. University of Queensland, Brisbane, Australia, 2. CSIRO, Pullenvale, QLD, Australia, and 3. Virginia Tech/ARI, Alexandria,VA

Introduction

The maceral is the original vegetable matter laid down to form coal. Maceral content is measured under the optical microscope using reflectance and structure to identify the macerals and surface area (converted to volume) to quantify the maceral groups. Figure 1. shows the maceral groups for hard coals (as opposed to brown, younger coals). Macerals have been used for a long time to characterize the performance of coking coals.

The major maceral groups are vitrinite composed of woody structures, exinite (also called liptinite) composed of resins, and inertinite composed of highly altered charcoal. The maceral groups are further divided into maceral subgroups (2). Falcon and Snyman (3) show micrographs of the different submacerals.

Pohl (1) correlated most of the physical and chemical properties of coal with the maceral groups and the carbon content on a dry ash-free basis (C(daf)). The correlations included chemical content gross chacateristics such as volatile matter content of brown and black coals, chemical structure, and most physical properties. The nitrogen content, porosity, and surface area of the coal did not correlate well with the maceral groups and C(daf). In general, the maceral group accounts for the original vegetable matter and the carbon content accounts for geological alternation of the material. Figure 2. shows an example of the correlation for volatile matter of hard (black) coal.

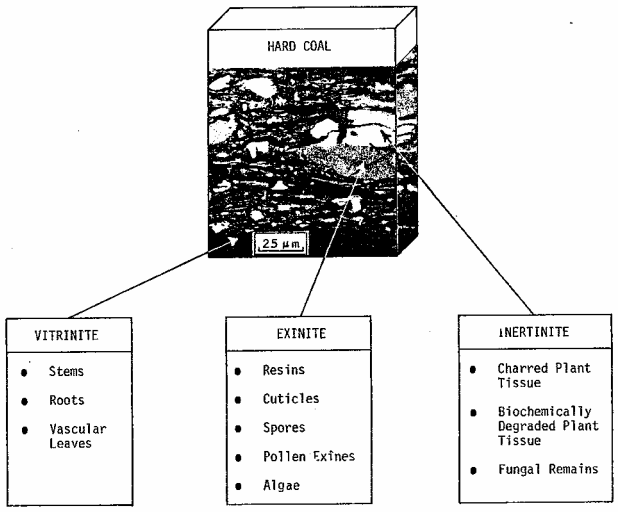

Figure 1. Maceral groups in coal. Heap, et al (1).

Pohl made attempts to correlate the maceral compositions of coals (1983-1986) with burnout of the coals measured in the Energy and Environmental Research Corp (EER) pilot scale furnace.

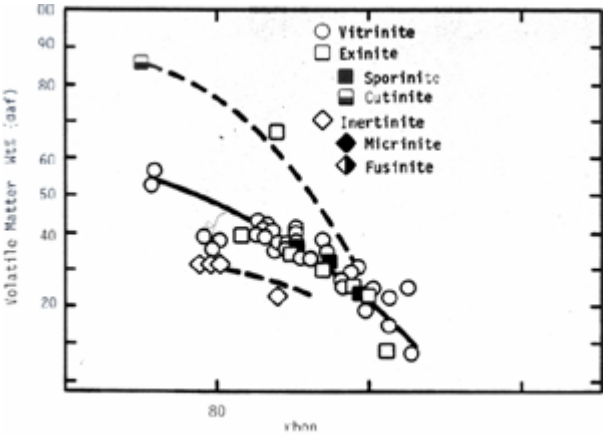

Figure 2. Correlation of volatile matter with carbon content for hard coals.(1).

The correlation used the amount of exinite plus ineritinite with a reflectance greater than 0.96. The correlation worked reasonably well, but had some problems. All maceral groups should be included. However, exinite was considered to rapidly volatilize (see Figure 2.) and burn quickly, and it was not considered necessary to include exinite in the correlation. The percent of vitrinite with reflectance greater than 0.96 worked reasonably well for USA coals where the major maceral group is vitrinite, but the correlation had to be done with percent of vitrinite and inernite with reflectance greater than 0.96 for Australian coals, where a majority of the maceral groups can be inertinite. Finally, the correlation could not differentiate between the burnout of different coals that had either 0 or 100 percent of the maceral material with reflectance greater that 0.96.

Chen, et al. (4) have recently made weight loss measurements during devolatilization and burning of single 100 um particles from pure vitrinite and some inertinite macerals groups. Chen identified the maceral groups under the optical microscope and dug out low ash 100 um pieces. The particles were suspended on a fine vibrating needle whose amplitude and frequency response were previously calibrated with glass spheres of known weight. A laser beam was spilt and used to heat the particle from two sides. We measured the particle temperature using two-color pyrometry and measured the change in amplitude and frequency continually through several hundred milliseconds until the particle completely burned. Five particles from each maceral were burned to statistically achieve an accuracy less than a factor of two for the rate of burning. Figure 3. shows the rate of weight loss in time for 5 particles each of coals with different rank (reflectance) dug from Australian Coals. Figure 3. indicates that at 80 percent burnout the rate of burning depends on the reflectance (rank) of the coal. Coals with low reflectance can have high rates of burning, while bituminous coals with reflectance near 1 can have low rates of burning. Preliminary data indicates different macerals of the same reflectance have the same burning rate and that the minimum in burning rate is a result of loss of surface area for bituminous coals.

Finally Su (6) used combinations of maceral concentrations to correlate the flame stability of pure and blends of Australian coals burned in the EER and Australia Coal Industry Research Laboratry (ACIRL) pilot scale furnaces.

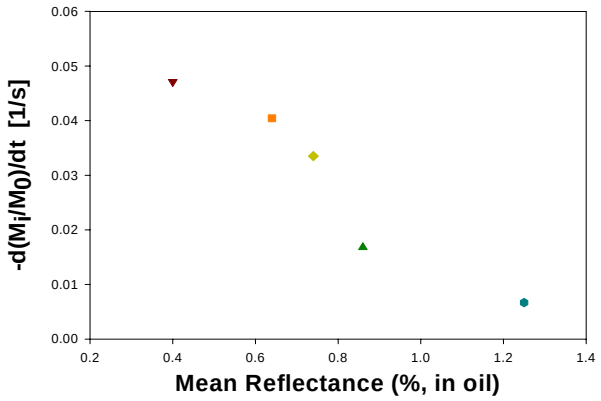

Figute 3. Vitrinite Maceral burning rate at 80 percent burnout. Chen, et al (4).

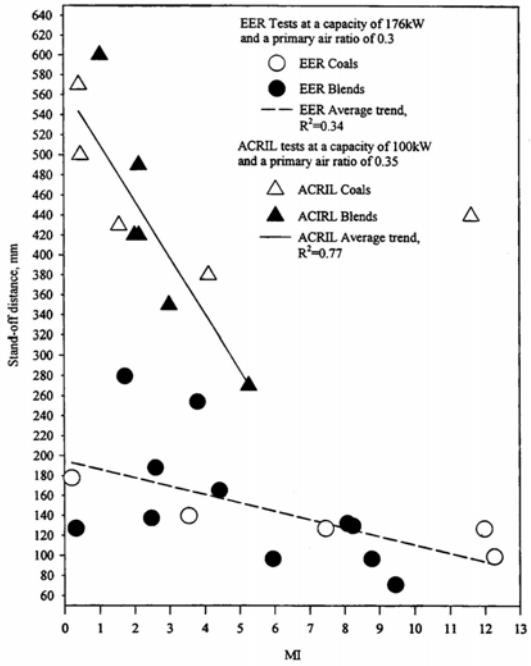

Figure 4. Correlation of Maceral Index (MI) with observed flame stability in two pilot scale furnaces. Su et a. (6)

The Maceral Index (MI) is:

$MI=(L+V/R^2/I^{1.25})*(HV/30)$

Where

MI=maceral index
L=volume percent of liptinite (exinite)
V=volume percent of vitrinite
R= vitrinite reflectance
I= volume percent inertinite
HV= high heating value in kcal/kg

Figure 5. shows the correlation of the maceral index with burnout. The correlation is excellent at high and low burnouts, but there is some scatter at burnouts around 99.5 percent and a few (5) points were not used to develop the empirical equation.

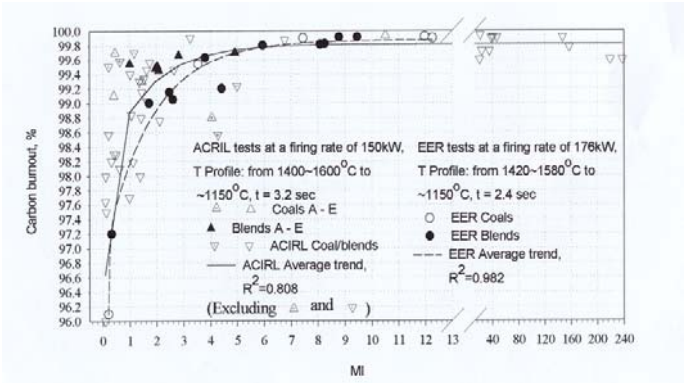

Figure 5. Correlation of Maceral Index (MI) with pilot scale burnout. A few points around 99 percent burnout were not included in developing the equation.

Conclusions

Maceral content appears to be a promising parameter to correlate coal properties and coal performance.

Acknowledgement. The authors wish to thank those who funded portions of the work at different times and places.:Electric Power Research Institute Palo Alto, CA, USA and Arun Metha, The Cooperativbe Research Centre for Black Coal Utilisation Research, Newcastle, NSW. Australia. We would also like to thank the places where this work was done: Energy and Environmental Research Co, Irvine, CA, USA, University of Queensland, Brisbane,QLD, Australia, and Australia Coal Industry Research Laboratory (ACIRL), Ipswich, QLD, Australia.

References

(1) Heap, M.P., J.C. Karmlich, D.W. Pershing, J.H. Pohl, W.F. Richter, and W.R.. Seeker, Effects of Coal Quality on Power Plant Performance and Costs, v.. 4 Review of Coal Science Fundamentals, Electric Power Research Institute, CS-4283, February 1986.

(2) Van Krevelen, D.W., Coal: Typology,-Physics,-Chemistry-Constitution, 3rd ed., Elsevier, Amsterdam, 1993);p. 39.

(3) Falcon, R.M..S., and C.P. Snyman, An Introduction to Coal Petrography: Atlas of Petrographic Constituents in the Bituminous Coals of Southern Africa, The Geological Society of South Africa, Johannesburg, South Africa.

(4) Chen, J., J.H. Pohl, V. Rudolph, and D. Harris, Combustion Rates of Single Maceral Particles from Australian Coals, Clean Power from Coal with Maximum Efficiency, China-Australian Workshop, Tiayuan, Shanxi, China, August 2001.

(5) J.H. Pohl and R. Payne, Pilot scale Evaluation of Mineral Matter on Boiler Performance, 2nd Annual Pittsburgh Coal Conference, Pittsburgh, PA, 1985, P.670.

(6) Su, S. J.H. Pohl, and D. Holcombe, Power Plant Performance of Blended Coals, 1st International Energy Conversion and Engineering Conference, AIAA, Portsmouth, VA, August 2003.

ENHANCED METHOD FOR PREDICTING THE PROPERTIES OF PETROLEUM FRACTIONS

Tareq A. Albahri

Chemical Engineering Dept. - Kuwait University
P.O.Box 5969 - Safat 13060, Kuwait
albahri@kuc01.kuniv.edu.kw

Introduction

The properties of petroleum and its fractions are usually determined experimentally in the laboratory. Several methods are available in the literature to predict these properties for petroleum fuels from their bulk properties such as the boiling point and the specific gravity for example. Although accurate enough, these methods are not suitable for incorporation into the molecularly explicit models for simulating the kinetics and dynamics of petroleum refining processes.

In previous work[1] we have developed a molecularly explicit characterization model (MECM) that allows for the simulation of the molecular composition of petroleum fractions using a pre-selected set of pure components. What is lacking, however, is the ability to predict the properties of the various streams as the molecular composition changes during processing by physical separation or chemical reaction. This work focuses on the development of such a property estimation method from the molecular composition of complex, multicomponent mixtures such as petroleum.

Technical Development

In our previous work on the simulation of light petroleum fractions[1] we have found that not all the properties of the petroleum fuel are required to be optimized against those from the pure components. In fact only the ASTM D86 Distillation, the PNA content and the RVP were sufficient to provide a feasible solution. All the other properties calculated form the bulk properties of the petroleum fraction and those from the pure components in them were almost alike. This lead us to believe that the properties of a petroleum fraction can be estimated from the above three properties alone.

The concept of the proposed model is that the global properties of a petroleum fraction such as the boiling point, the vapor pressure and the paraffins, naphthenes, and aromatics content must be equal to those calculated from the pure components contained in that petroleum fraction. When both bulk and pure component properties are available, the composition of the petroleum fraction may be predicted using optimization algorithms as simplified in Figure 1. The predicted composition of a limited set of pure components may then be used to predict the other properties of the petroleum fuel using appropriate mixing rules.

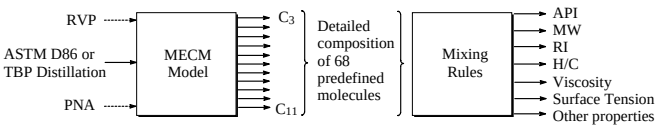

Figure 1. Simplified schematic representation of the proposed model.

Experimental values of the RVP and PNA are always desirable as inputs. However, when these are not available they may be predicted using methods available in the literature[2,3] making the ASTM D86 distillation or the true boiling point (TBP) the minimum model input required.

The internally calculated properties are the molecular weight, the Reid vapor pressure (RVP), the true vapor pressure at 100°F, the specific (API) gravity, the cubic average boiling point (CABP), the mean average boiling point (MeABP), the volumetric average boiling point (VABP), the weight average boiling point (WABP), the molar average boiling point (MABP), the Watson characterization factor (K_w), the refractive index, the carbon to hydrogen ratio (C/H), the kinematic viscosity at 100 and 210°F, the surface tension, the aniline point, the true and pseudo critical temperatures and pressures, the critical compressibility factor, the acentric factor, the freezing point, the heat of vaporization at the normal boiling point, the net heat of combustion at 77°F, the isobaric liquid heat capacity at 60°F, the isobaric vapor heat capacity at 60°F, the liquid thermal conductivity at 77 ºF, and the paraffins, naphthenes, and aromatics content. These properties are calculated for the petroleum fraction using well established methods in the literature or were developed specifically for this project[1].

The same properties are calculated from the pure component composition using the appropriate mixing rules from the literature. When the pure component properties are not available in databases they were estimated using group contribution methods available in the literature or were developed specifically for this project[1].

The difference between the values obtained from the two different methods for the true boiling point and the PNA content are minimized in the objective function the purpose of which is to calculate the values of x_i which is the mole fraction of the pure components in the petroleum fraction. This is shown in Equation 1 where both PNA and T_b of the pure components are a function of x_i. The composition of the light ends was determined using the RVP which is converted to the true vapor pressure at 100 °F and then using simple bubble point calculations.

The First line in the objective function represents the sum of errors in the boiling points of the pure components and the corresponding value on the true boiling point (TBP) curve. The pure component concentrations are determined by minimizing the following modified objective function,

$$S = \sum_{j=1}^{n} \left((Tb_j - T'b_j) \times W_o \times 100 / Tb_j \right)^2 + \left((PNA - PNA') \times W_1 \times 100 / PNA \right)^2 \quad (1)$$

where j is the index number of the molecule and n is the total number of molecules. PNA_i and PNA'_i refer respectively to the actual and predicted paraffin, naphthene, and aromatic content of the petroleum fraction. T_{bj} and T'_{bi} refer respectively to the boiling point of the pure component j and the corresponding value on TBP curve. W_1 and W_o are weighting factors and S is the objective function to be minimized.

An optimization algorithm based on the least square method was used to minimize the objective function while calculating the concentration of the pure components. The nonlinear regression algorithm minimizes the sum of the difference between the fuels bulk properties and those estimated from pure components. Using the Microsoft Excel Solver tool and the global optimization algorithm, convergence was achieved in less than one minute for all cases on a Pentium IV-1.7 GHz PC.

Discussion

The model was tested to predict the properties of 30 petroleum naphtha samples ranging in API from 35 to 91, IBP from 62 to 267 °F and FBP from 152 to 312 °F. Some of these results are shown in Table 1 and Figures 2 to 4. The MECM model proves to be a powerful tool for simulating the properties of petroleum fuels.

This work demonstrates that the complex nature of petroleum fuels may be modeled by a limited set of representative pure components using non-linear-regression optimization models. Considering the difficulty and limitations in predicting the properties of petroleum fuels in the currently used pseudo component techniques, the proposed method can be an effective alternative. The clear advantage of the model is its ability to compliment the molecularly explicit models for petroleum refining processing.

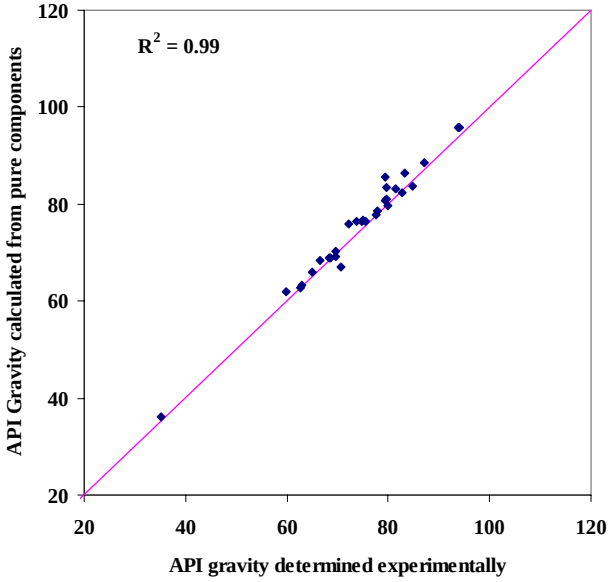

Figure 2. Bar plot for the predicted API gravity from pure components for 30 petroleum naphtha samples versus that calculated from global properties using published methods.

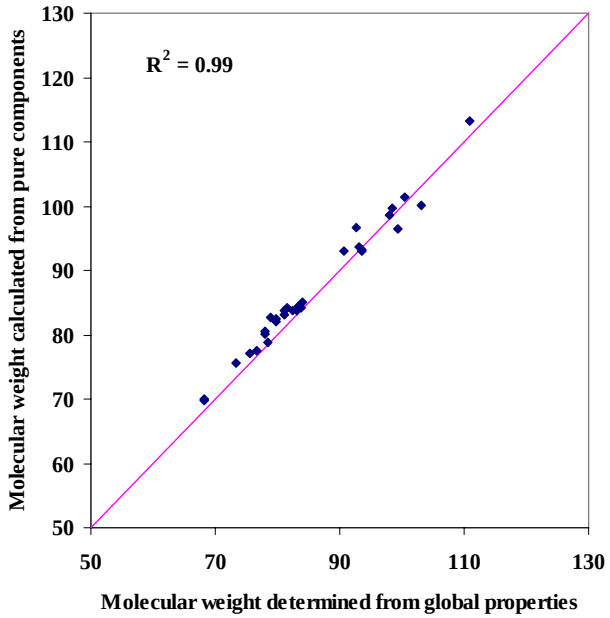

Figure 3. Bar plot for the predicted molecular weight from pure components for 30 petroleum naphtha samples versus that calculated from global properties using published methods.

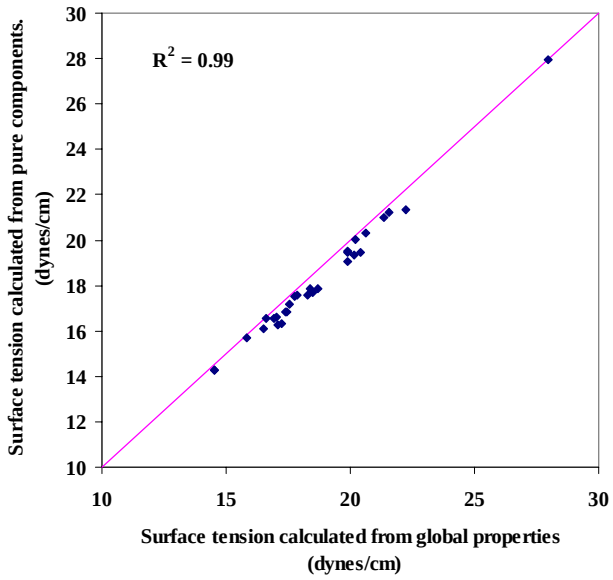

Figure 4. Bar plot for the predicted surface tension from pure components for 30 petroleum naphtha samples versus that calculated from global properties using published methods.

Table 1. Error analysis for some of the properties investigated

No.	Property	Av. % error	Corr. Coef.
1.	API gravity	2.67	0.995
2.	Cubic average boiling point	1.34	0.995
3.	Mean average boiling point	0.99	0.995
4.	Volume average boiling point	1.34	0.995
5.	Molar average boiling point	0.83	0.995
6.	Mass average boiling point	1.07	0.996
7.	Watson characterization factor	0.80	0.970
8.	Molecular weight	2.06	0.990
9.	Refractive index	0.21	0.993
10.	Hydrogen content	2.57	0.965
11.	Viscosity at 210 °F	4.04	0.960
12.	Viscosity at 100 °F	5.41	0.972
13.	Surface Tension	2.67	0.995
14.	Aniline Point	4.27	0.830
15.	Critical temperature	0.93	0.991
16.	Pseudocritical temperature	0.80	0.989
17.	Pseudocritical pressure	2.22	0.890
18.	Heat of vaporization	2.07	0.948
19.	Heat of combustion	0.80	-
20.	Freezing	5.38	-
21.	Acentric factor	3.13	0.946
22.	Critical compressibility factor	0.25	0.832
23.	Flash point	5.16	0.924

Acknowledgment

This work was supported by Kuwait University, Research Grant No. EC04/01.

References

[1] T. A. Albahri, Am. Chem. Soc., Div. fuel chem. prep., **2004**, 49(1), 327-328.
[2] M. R. Riazi & T. E. Daubert, Ind. Eng. Chem. Process Des. Dev., **1980**, 19 (2), 289-294.
[3] Jenkins, G. I. and white, M. M.. J. Inst. Petrol., **1969**, 55 (543), 153.

EFFECT OF ATMOSPHERES ON EVOLUTION OF SULFUR CONTAINING GASES DURING COAL PYROLYSIS

Qiang Zhou, Haoquan Hu, Quanrun Liu, Shengwei Zhu*

Institute of Coal Chemical Engineering, Dalian University of Technology, 129 street, Dalian 116012, P.R.China
* hhu@chem.dlut.edu.cn

Introduction

Coal is the main consumption energy in China, meanwhile it is also the main pollution contributor. Sulfur is a major factor in inhibiting the effective and extensive utilization of coal. So desulfurization is very necessary for improving coal quality and for protecting environment. Although many methods have been developed for coal desulfurization, an effective and economic process remains to be found.

Pyrolysis as an important intermediate stage in coal gasification, combustion and liquefaction etc, and a simple and effective method for clean conversion of coal has received many attentions. By pyrolysis both inorganic sulfur and organic sulfur can be removed, and most sulfur goes into gas phase in the form of sulfur containing gases (H_2S, COS, CH_3SH, CS_2 and SO_2, etc.) which is relatively easy to be recovered as sulfur. Thus knowledge of evolution of sulfur containing gases during pyrolysis is essential in finding optimum desulfurization method.

Numerous factors, including coal properties and pyrolysis conditions affect sulfur removal during the pyrolysis of coal[1,2]. Many studies about those have been done and some useful results have been obtained. Although gases derived from coal pyrolysis, such as N_2, H_2, CH_4, CO, CO_2 and so on, play important roles on the formation of sulfur containing gases, little effort has been done. The aim of this study was to investigate the effect of those gas components on the evolution of sulfur containing gases during coal pyrolysis.

Experimental

Coal Samples. Two Chinese coals, Yanzhou (YZ) and Datong (DT) coal, were used in the study. Air-dried samples were ground to -100 mesh before use. The proximate, ultimate and sulfur form analyses of two coals are listed in Table 1.

Table 1 Analyses of coals

Coal	Proximate (wt%)			Ultimate (wt%, daf)			Sulfur (wt%, db)			
	M_{ad}	A_d	V_{daf}	C	H	N	S_t	S_p	S_s	S_o*
YZ	5.9	27.7	44.8	81.4	5.7	1.3	3.6	1.7	0.1	1.8
DT	2.9	13.7	32.7	76.9	4.1	0.5	1.6	1.2	0.1	0.3

S_t: total sulfur; S_p: pyritic sulfur; S_s: sulfatic sulfur; S_o: organic sulfur. * By difference.

Pyrolysis. Pyrolysis was performed in an ambient pressure, vertical quartz micro-fixed bed reactor with inner diameter of 5mm; approximate 50mg sample placed in the reactor was heated from 25 to 1000°C with a heating rate of 5K/min under different pyrolysis atmospheres (90% N_2 mixed with 10% other selected gases, i.e. H_2, CO, CO_2 and CH_4). Air was removed from system by purging with pyrolysis atmospheres before each run. Gaseous products were all led to a gas chromatograph (GC) which was equipped with a 3m long glass column packed with 25% 1,2,3-tris(2-cyanoethoxy)propane and a flame photometric detector (FPD) to analyze sulfur-containing gases. To avoid the condensation of tar in the heating zone in the reactor, a high gas flow rate, 200cm^3min^{-1}, was used. Tar was trapped by quartz wool at outlet of the reactor. To avoid adsorption of sulfur containing gases by system, glass tube (i.d.=1mm) was used as conduit to connect reactor with GC. Total sulfur in coal was determined by Coulomb method (Testing Standard of China: GB214-77) and pyrite sulfur content was determined by ASTM D2492-80.

Results and Discussion

H_2S evolution. Figure 1 shows H_2S evolution during coal pyrolysis as function of temperature in different atmospheres. It can be seen that the evolution of H_2S during coal pyrolysis is affected by coal properties and pyrolysis conditions.

For DT coal, only one peak at about 525°C on H_2S evolution curve with two shoulders can be observed when pyrolyzed in N_2. According to the literatures[3,4], the peak is attributed to the decomposition of pyrite. The shoulder at lower temperature corresponds to the decomposition of aliphatic sulfur, and the shoulder at higher temperature is related to the decomposition of aromatic sulfurs. When YZ coal was pyrolyzed in N_2, two peaks, at about 425°C and 550°C, on H_2S evolution curve can be observed. As stated above, the first peak is related to the decomposition of aliphatic sulfur, and the second one is attributed to the decomposition of pyrite. Above 650°C, because of fixation of H_2S in mineral matter[5], almost no H_2S releases for both coals.

Compared with H_2S evolution in N_2, more H_2S evolves and more H_2S peaks are observed as coals were pyrolyzed in H_2. For DT coal, four H_2S peaks, at about 300, 525, 650 and 750°C, respectively, can be observed. According to the literature[6], the first peak results from decomposition of aliphatic sulfur, the second from decomposition of pyrite, the third and the last from decomposition of pyrrhotite and organic sulfur, such as thiophenes. The H_2S evolution of YZ coal is similar to that of DT coal, except the first peak shifts to higher temperature, which indicates the organic sulfur in thermally labile structures is mainly in the form of disulfides in YZ coal. And the effect of H_2 on the peak from pyrite decomposition is more pronounced, which results in a great difference between the peak in N_2 and that in H_2. This may be explained from the good swelling property of YZ coal which may trapped more sulfur from decomposition of pyrite, successively this trapped sulfur may transform into organic sulfur in N_2, thus less sulfur releases as H_2S. And the peaks of H_2S derived from decomposition of both pyrrhotite and thiophenes are integrated into a broad peak at about 725°C.

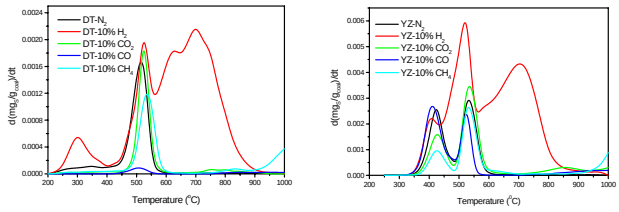

Figure 1. Effect of atmospheres on evolution of H_2S during coal pyrolysis

Compared with the effect of N_2 on H_2S evolution, CO prohibits H_2S evolution for DT coal, and has little effect for YZ coal at temperature below 650°C. Above 650°C, CO promotes H_2S evolution for both coals. This may be caused by the following reactions:

$$CO + FeS \rightarrow COS \quad [7]$$

$$COS + H_2 \rightarrow CO + H_2S \quad (\Delta G = -16.3 kJ/mol\ [8])$$

In CO_2, less H_2S releases below 500°C and more H_2S evolves at temperature region of 500 to 600°C than that in N_2. CO_2 reacts with

C (coal) to form CO at high temperature, so the evolution of H_2S in CO_2 is similar to that in CO.

In CH_4, less H_2S evolves than that in N_2 at temperature below 650°C; above this temperature, more H_2S evolves and the rate increases with increasing temperature. This may be resulted from the decomposition of CH_4 to form H_2[9], which promotes the decomposition of pyrrhotite and/or thiophenes to form H_2S.

COS evolution. It is known that COS derives from pyrite and organic sulfur[4,7]. The profiles of COS evolution during pyrolysis of two coals as a function of temperature in different atmospheres are presented in **Figure 2**.

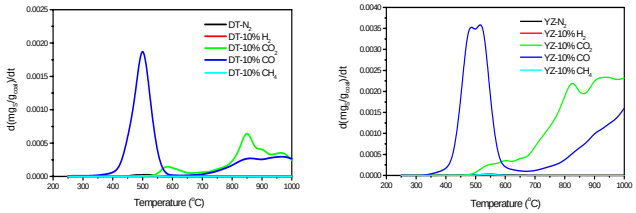

Figure 2. Effect of atmospheres on evolution of COS during coal pyrolysis

From **Figure 2** it can be seen that when coal was pyrolyzed in N_2, only a little COS evolved and mainly occurs in the temperature range of 450 to 600°C. Compared with the COS evolution in N_2, CH_4 and H_2 prohibits the formation of COS. This is because that H_2 may react with oxygen contained in coal to form water and consequently causes less CO formation, and that CO promotes the formation of COS, which will be discussed latter; meanwhile both H_2 and water can react with COS to form H_2S, all lead to less formation of COS. CH_4 may decompose to H_2 at relative low temperature in presence of coal, then it has similar effect as H_2.

Compared with the effect of N_2 on COS evolution, CO promotes the formation of COS and a COS evolution peak is observed at about 500°C, i.e. the pyrite decomposition temperature, for both coals, this shows that CO competes with H_2 to react with sulfur derived from the decomposition of pyrite. Above 650°C, the rate of COS evolution increases with increasing temperature. CO_2 also promotes the formation of COS, but at temperature below 575°C, the extent is not notable; above this temperature, more COS is formed than that in CO. This result indicates that the formation of COS is mainly related to CO in system and the effect of CO_2 is owing to the formation of CO by reaction of CO_2 with C (coal) at high temperature.

CH_3SH evolution. CH_3SH is mainly derived from the decomposition of organic sulfur in coal[2], so the evolution of CH_3SH also reflects the knowledge of decomposition of organic sulfur in coal. **Figure 3** shows the CH_3SH evolution rate profiles of the select coals in different pyrolysis atmospheres. From **Figure 3** it can be seen that the CH_3SH evolution during coal pyrolysis, just as H_2S evolution, is affected by not only pyrolysis conditions, but also coal properties. The evolution of CH_3SH mainly occurs in temperature range of 200 to 650°C, which indicates that the CH_3SH is mainly derived from the decomposition of organic sulfurs in the form as thiols, polysulfides, disulfides, dialkyl sulfides and alkyl-aryl sulfides etc.

As coal was pyrolyzed in N_2, two peaks, at around 275°C and 475°C, for DT coal and one peak, at around 475°C, for YZ coal can be observed. From the temperature of CH_3SH evolution peak, it can be concluded that there is some thiols, polysulfides and disulfides in DT coal, and some disulfides in YZ, respectively.

Compared with the evolution of CH_3SH in N_2, less CH_3SH evolves in H_2, which is caused by the promotion of H_2 on the decomposition of organic sulfur into H_2S. The other two atmospheres make CH_3SH peak shifts to high temperature.

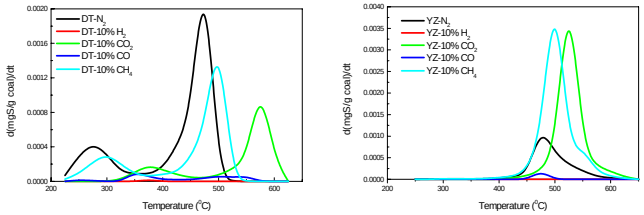

Figure 3. Effect of atmospheres on evolution of CH_3SH during coal pyrolysis

CS_2 evolution. The formation of CS_2 was also observed, but the effect of atmospheres on the formation of CS_2 is somewhat irregular. Some researchers assumed that CS_2 is derived from the reaction between pyrite and CH_4[1,10], no evidence proves CH_4 is essential for the formation of CS_2 in this study, but the evolution of CS_2 occurs in the temperature region of pyrite decomposition, which indicates that the decomposition of pyrite attributes to the formation of CS_2.

Little SO_2 was observed during pyrolysis of two coals in five atmospheres.

Conclusions

Compared with the evolution of sulfur containing gases in N_2, CO promotes the formation of COS; CO_2 prohibits the evolution H_2S at temperature below 500°C and shows similar effect on sulfur containing gases as CO does at above 500°C; CH_4 prohibits the evolution of H_2S more intensely than CO_2 at temperature below 650°C, but at higher temperature, more H_2S is formed; H_2 promotes the formation of H_2S and prohibits the formation of other sulfur containing gases.

Acknowledgement. This work was performed with the supports of the National Key Fundamental Research and Development Project of China (G1999022101).

References

(1) Khan, M. R. *Fuel*, **1989**, *68*, 1439.
(2) Hu, H.; Zhou, Q.; Zhu, S.; Krzack, S.; Meyer, B.; Chen, G. *Fuel Processing Technology*, **2004**, *85*(8-10), 849.
(3) Sugawara, K.; Enda, Y.; Kato, T.; Sugawara, T.; Shirai, M. *Energy and Fuels*, **2003**, *17*(1), 204.
(4) Ibarra, J. V.; Bonet, A. J.; Moliner, R. *Fuel*, **1994**. *73*(6): 933.
(5) Liu, Q.; Hu, H.; Zhou, Q.; Zhu, S.; Chen, G. *Fuel Processing Technology*, **2004**, *85*(8-10), 863.
(6) Piotr, R.; Steven, M.; Jan, Y.; Grazyna, G. *Fuel Process. Technol.* **2002**. *76*(2), 121.
(7) Furimsky, E.; Palamer, A. D.; Cheng, M. *The Canadian journal of chemical engineering*, **1991**. *69*, 869.
(8) Trewhella, M. J.; Grint, A. *Fuel*, **1987**, *66*(10), 1315.
(9) Breakman-Danheux, C.; Cypress, R.;Fontana A. *Fuel*, **1992**, *71*, 251
(10) Oh, M. S.; Burnham, A. K.; Crawford, R. W. Prepr. Pap. – *Am. Chem. Soc. Div. Fuel Chem.*, **1988**, *33*, 274.

EFFECT OF ATMOSHPERES ON SULFUR TRANSFORMATION DURING PYROLYSIS OF YIMA COAL

Qiang Zhou, Haoquan Hu, Quanrun Liu, Shengwei Zhu*

Institute of Coal Chemical Engineering, Dalian University of Technology, 129 street, Dalian 116012, P.R.China
* hhu@chem.dlut.edu.cn

Introduction

Desulfurization of coal is very necessary for improving coal quality and for protecting environment. Although many methods have been developed for coal desulfurization, an effective and economic process remains to be found.

Hydropyrolysis (HyPy), as an effective desfurfurization method, has received many attentions, but it's unprofitable to undertake industrial HyPy with pure hydrogen in the present energy market. Thus, it is necessary to use cheaper hydrogen-rich gas instead of pure hydrogen gas.

Some researchers have used coke-oven gas as hydrogen resource to study the sulfur removal and observed satisfying results[1]. However, little effort on the influence of pure components of coke-oven gas on sulfur transformation during coal pyrolysis has been done. The aim of this study was to study the effect of four main pure components of coke-oven gas, i.e. H_2, N_2, CH_4 and CO, on the behavior of sulfur during fixed-bed pyrolysis of Yima coal.

Experimental

Coal sample. A high sulfur Chinese coal, Yima coal (YM), ground to -100mesh, and dried in a vacuum oven at 100°C for 24hrs was used in the study. The analytical data are given in Table 1.

Table 1. Analyses of YM coal

Proximate (wt%)			Ultimate (wt%, daf)			Sulfur form (wt%, db)			
M_{ad}	A_d	V_{daf}	C	H	N	S_t	S_p	S_s	S_o *
5.9	27.7	41.3	80.1	5.3	1.2	2.4	1.5	0.1	0.8

S_t: total sulfur; S_p: pyritic sulfur; S_s: sulfatic sulfur; S_o: organic sulfur. * By difference.

Pyrolysis. Pyrolysis of coal was carried out in an ambient pressure, horizontal fixed-bed reactor (i.d. 18mm) under isothermal conditions at carried gas flow rate 400ml/min, residence time 20min and temperature from 350 to 900°C. About 2g coal samples were placed in a stainless steel boat and heated in furnace, preheated carried gas flowed through fixed-bed and carried out the volatilized matter. The heating time from ambient temperature to the desired is in about 2 minutes. After reaching the determined time, the boat was moved away from the furnace and let it cool down to the ambient temperature. To minimize the problem of the weight lose of char, the weight of char was calculated from the weight difference of boat and sample before and after pyrolysis of coal. The air was removed from the system by purging with nitrogen at the beginning of each run.

Analysis. The Coulomb method (Testing Standard of China GB214-77) was used to determine the total sulfur content in coal and residual chars, the sulfur form content was determined by the Gladfelter method[2]. The removal of total sulfur was calculated by the following expressions:

$$Desulfuriz\ ation\ ,\% = \left(\frac{S_{t,coal\,(d)} - S_{t,char\,(d)} \times Y_{char\,(d)}}{S_{t,coal\,(d)}}\right) \times 100 \qquad (1)$$

Where $S_{t,coal(d)}$, $S_{t,char(d)}$ is total sulfur content (dry base) of coal and char, respectively; $Y_{char(d)}$ is the yield of char (dry base) during pyrolysis.

Results and Discussion

Total sulfur. The total sulfur content in residual chars is shown in **Figure 1**. When Yima coal is pyrolyzed in H_2, the total sulfur content in residual char decreases with increasing temperature. The decrease mainly occurs in 350-450°C and 650-900°C regions, reaches 0.4 and 0.7wt%, respectively. In the region of 550-650°C, only 0.03wt% total sulfur decrease is occurred.

In N_2, the total sulfur content in chars increases from 2.25wt% at 350°C to 2.57wt% at 450°C firstly, and then decreases with increasing temperature at the range of 450 to 550°C. Above 550°C, the total sulfur content increases slowly from 2wt% to 2.17wt% at 900°C.

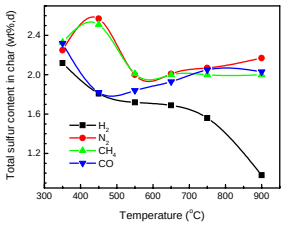

Figure 1. Total sulfur contents *vs* temperature in chars

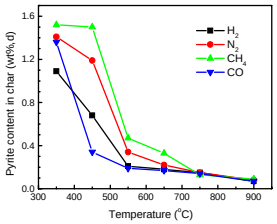

Figure 2. Pyrite sulfur contents *vs* temperature in chars

CO shows similar effect on total sulfur content change as H_2 does at temperatures below 450°C. Above this temperature, the total sulfur content continues to increase monotonously with increasing temperature, reaching 2.05wt% at 750°C, and then remains almost constant with increasing temperature.

The trend of total sulfur content change in residual chars obtained in CH_4 is similar as that in N_2 until temperatures up to 650°C. Above this temperature, the total sulfur content does not markedly change and becomes constant at about 2wt%.

Sulfate sulfur. Because the sulfate sulfur is only 3.78% of total sulfur in raw coal, it is not discussed in this study.

Pyritic sulfur. Figure 2 shows the effects of atmospheres on changes of pyritic sulfur content in residual chars during pyrolysis. It can be seen that H_2 and CO show similar effectiveness on decomposition of pyrite, while CH_4 shows similar effect as N_2 does.

The decomposition of pyrite mainly occurs at temperature region of below 550°C in atmospheres of H_2 and CO. In this region, the pyritic sulfur content decreases from 1.50% in raw coal to 0.21 at 550°C in H_2, and 0.19% in CO, respectively. At lower temperatures, H_2 shows more positive effect on the pyrite decomposition than that CO does.

Pyrite is more stable in the other two atmospheres, especially in CH_4. The mainly decomposition takes place in the temperature of 450 to 550°C for both atmospheres, and the decrease reaches 0.85 and 1.03wt% in N_2 and CH_4, respectively. At temperatures below 450°C, the content decreases slowly in N_2, and almost remains constant in CH_4 with increasing temperature.

Above 750°C, the pyritic sulfur in residual char is mainly affected by temperature, and only a little (<0.1wt%) remains in chars in all atmospheres at 900°C.

Organic sulfur. The influence of atmospheres on the organic sulfur content in residual chars during pyrolysis is given in **Figure 3.** It can clearly be seen that both temperature and atmospheres have significant effects on the decomposition of organic sulfur and transformation of inorganic sulfur into organic sulfur.

When coal pyrolysis in H_2 and temperature rise to 450°C, the organic sulfur content in residual char decreases from 0.76wt% in the raw coal to 0.57wt%, then increases with increasing temperature and reaches 0.66wt% at 650°C. Above this temperature, the content of organic sulfur in residual char decreases again and reaches 0.34wt%

at 900°C. The first decrease is caused by the decomposition of organic sulfur groups with low thermal stability, such as thiols and Polysulfides[3]. The considerable increase in organic sulfur is accompanied by the intensive decomposition of pyrite, which indicates the increase is from the transformation of inorganic sulfur. Other researchers also observed the increase of organic sulfur in char in hydrogen atmosphere [4]. The new-formed organic sulfur may have high thermal stability and is very difficult to decompose. The second decrease is caused by the decomposition of aromatic sulfurs[3]. The organic sulfur remains in residual char (0.34wt%) at 900°C may exist in condensed thiophenic species.

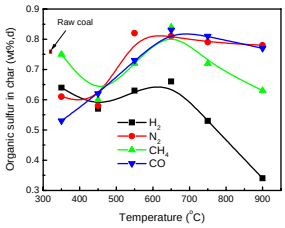

Figure 3. Organic sulfur content *vs* temperature in chars

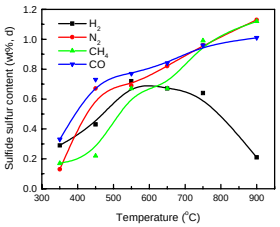

Figure 4. Sulfide sulfur content *vs* temperature in chars

The change of organic sulfur content in N_2 is similar to that in H_2 below 650°C, but the content is notable higher in N_2 than that in H_2 except at 350°C. At higher temperatures, the organic sulfur content remains almost constant in N_2. As mentioned above, the decomposition of pyrite in coal mainly occurs at 450 to 500°C in N_2, while in H_2 rich environment, this reaction starts at a relatively low temperature [5].

More organic sulfur persists in residual char in CH_4 than that in N_2 at temperatures below 450°C. Above 650°C, less organic sulfur remains in residual char in CH_4 than that in N_2. At high temperature CH_4 may decompose to H_2[6] and more ethene will be formed in the presence of CH_4 during coal pyrolysis[7]. Except for the promotion of H_2 on decomposition of organic sulfur, ethene also can react with H_2S or nascent sulfur derived in pyrolysis to form small molecule sulfur containing organic species and releases[8,9]; Meanwhile, ethene can react with organic matrix in residual char, which will decrease the coal conversion, all those lead to low sulfur content in chars.

At studied temperature range, the change of organic sulfur content in chars in CO is similar to that in N_2, but it seems that CO prohibits the transformation of pyrite sulfur to organic sulfur. CO promotes the decomposition of pyrite[1], while has little effect on coal pyrolysis, thus the relative ratio of organic free radical to nascent sulfur is lower in CO than that in N_2, so less nascent sulfur is trapped by free radical to form new stable organic sulfur in CO.

Sulfide sulfur. Figure 4 represents the sulfide sulfur content of residual chars obtained in different atmospheres. The sulfide sulfur content in char increases steadily with the progressive decomposition of the pyrite in H_2 up to 550°C, and then decreases with increasing temperature because of the decomposition of sulfide sulfur. At 900°C, only 0.21wt% sulfide sulfur persists in residual char.

The change of sulfide sulfur content in char obtained in other three atmospheres is similitude with each other, i.e. it increases with increasing temperature. By comparing **Figure 2** with **Figure 4**, it can be seen that the increase of the quantity of sulfide sulfur is corresponding to the extent of the decomposition of pyrite at temperatures below 650°C. Above this temperature, although the conversion of pyrite to ferrous sulfur is nearly complete, a further increase in sulfide sulfur is observed, which is caused by the reaction of hydrogen sulfide with alkali mineral [3,10].

Sulfur removal. The sulfur removal during coal pyrolysis is shown in **Figure 5**. It can be seen that the most effective temperature for sulfur removal of Yima coal in H_2, N_2, CH_4 and CO is 900, 550, 550 and 450°C, respectively. And the desulfurization reaches 75.5, 39.1, 38.4 and 44.0%, respectively.

In the early pyrolysis stage, below 550°C, in H_2, the desulfurization yield increases rapidly with increasing temperature from 17.1wt% at 350°C to 49.1wt% at 550°C, and then increases slowly with increasing temperature up to 750°C (59.0wt%), above 750°C, increases rapidly again, reaching 75.5wt% at 900°C. The rapid increase at temperature below 550°C is mainly caused by the decomposition of pyrite and organic sulfur groups of low thermal stability, see **Figure 2** and **Figure 3**, at temperature above 750°C is caused by the decomposition of organic sulfur and sulfide sulfur, see **Figure 3** and **Figure 4**, the slowly increase at middle temperature results from the transformation of inorganic sulfur into organic sulfur.

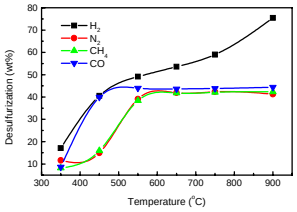

Figure 5. Effect of atmospheres on desulfurization

The desulfurization in other atmospheres are mainly caused by the decomposition of pyrite, so desulfurization mainly occurs at temperature 450-550°C for N_2 and CH_4, and 350-450°C for CO, respectively, which corresponds the temperature region of pyrite decomposition.

Conclusions

By analysis the sulfur form content changes in residual chars obtained in different atmospheres, the following conclusion can be drawn. The decomposition of pyrite mainly occurs at temperature region of below 550°C in atmospheres of H_2 and CO; in other two atmospheres, especially in CH_4, pyrite is more stable and the mainly decomposition temperature region is 450-550°C. The organic sulfur content in the residual char is the net effect of decomposition of organic sulfur species with low thermal stability and formation of new ones with high thermal stability by the reaction of hydrogen sulfide and/or nascent sulfur with organic matrix. Above 750°C, CH_4 can promote the decomposition of organic sulfur.

Acknowledgement. This work was performed with the supports of the National Key Fundamental Research and Development Project of China (G1999022101).

References

(1) Liao, H. Q.; Li, B. Q.; Zhang, B. J. *Fuel*. **1998**, *77*, 1643.
(2) Sugawara, T.; Sugawara, K.; Ohashi, H. *Fuel* 1988. *67*,1263.
(3) Grazyna, G. *Fuel*, **1995**. *74*, 356.
(4) Xu, W. C.; Kumagai, M. *Fuel*, **2003**. *82*, 245.
(5) Khan, M. R. *Fuel*, **1989**, *68*, 1439.
(6) Breakman-Danheux, C., Cypress, R., Fontana A., *Fuel*, **1992**, *71*, 251.
(7) Calkins, W. H.; Bonifza, C. *Fuel*, **1984**, *63*, 1716.
(8) Attar, A. *United States Patent* 4465493, August 14, **1984**.
(9) Hu, H.; Wu, X.; Zhu, S. Prepr. Pap. - *Am. Chem. Soc., Div. Fuel Chem.*, **2003**,*48*(1), 409.
(10) Liu, Q.; Hu, H.; Zhou Q.; Zhu S.; Chen G. *Fuel Processing Technology*, 2004, *85*(8-10), 863.

EFFECTS OF BOILER OPERATION ON WET FLUE GAS DESULPHURIZATION SYSTEM

Manyin Hu[1], Hezhong Tian[2], Bingwei Liu[1], Lidong Wang[1], Shuqin Wang[1]

1. School of Environmental Science and Engineering, North China Electric Power University, Baoding 071003, China
2. Department of Environmental Science and Engineering, Tsinghua University, Beijing 100084, China

1. Introduction

With the continuously rapid economy growth, coal-dominated energy consumption in China has caused very serious SO_2 and acid rain pollution. Northeastern Asia including China has become the third acid rain areas in the world. In 2000, total coal burning by utility boilers in China was about 600Mt, accounting for 60% of the total coal consumption. Coal fired power plants emitted more than 8Mt SO_2, contributing as high as 40% of the total SO_2 emissions in China [1]. Therefore, equipping with desulphurization installations to abate SO_2 emission from coal fired power plants is crucial for SO_2 and acid rain control in China.

Among all kinds of desulphurization processes, wet limestone-gypsum flue gas desulphurization (FGD) is the most popular process in power plant for its high efficiency, mature technique, as well as cheap and widely distributed limestone absorbent. In the early 2004, Chinese government promulgated new version of air pollutants emission standards for thermal power plant [2], newly modified SO_2 emission ceilings will lead to large amount of FGD installation.

Boiler operation conditions have a great impact on FGD performance, such as coal characteristics, excess air coefficient, boiler load, et al. In this paper, effects of these factors on FGD efficiency were analyzed and discussed, and mathematical expression of FGD efficiency was deduced. In addition, univariable and multivariable regression between FGD efficiency and some factors were carried out.

2. Factors influencing FGD performance

2.1 Coal characteristics. 2.1.1 Sulfur content

Coal sulfur content and the share of combustible components have a great impact on flue gas SO_2 concentration and FGD performance. High SO_2 concentration can improve kinetic reactivity velocity, but it is much less than the effects of SO_2 volume increase, so the desulphurization efficiency declined.

2.1.2 Coal element components

Different coal element configuration not only has impact on flue gas components and characteristics, also has effects on the flue gas rate and SO_2 concentration.

2.1.3 Coal low heating value (LHV)

Coal low heating value determined coal burning rate and produced flue gas rate. Thus, it can influence SO_2 concentration and FGD efficiency.

2.2 Gas velocity. Below the flooding velocity, gas velocity increase facilitate decreasing liquid diameter to increase the contact area, it is advantage to the SO_2 absorption. But when the gas velocity is above flooding velocity, it will make the contact of gas and liquid overbalance, which will decrease the efficiency [3].

2.3 Excessive air coefficient and air leak coefficient. The changes of excessive air coefficient of hearth exit and air leak coefficient of boiler flue directly affect the gas amount and make the SO_2 concentration and gas velocity change, and further affect the desulphurization efficiency.

2.4 Boiler load. Boiler load affects flue gas volume, gas velocity and SO_2 rate, which will make the desulphurization efficiency change.

3. Mathematical models

3.1 Desulphurization efficiency of wet FGD system. Desulphurization efficiency of wet flue gas desulphurization system can be expressed by the following equation:

$$\eta = \left[1 - C'_{SO_2} / C_{SO_2}\right] \times 100 \qquad (\%) \qquad (1)$$

Where, η is desulphurization efficiency (%), C'_{SO_2} and C_{SO_2} is the outlet and inlet SO_2 concentration of FGD (mg/Nm^3), respectively.

Desulphurization efficiency of wet FGD system is determined by liquid-gas ratio, pH value of slurry, inlet SO_2 concentration, etc. It is difficult to reveal completely the relationship between the desulphurization efficiency and the above factors, thus some hypotheses were given as following:

Air flow in the desulphurization tower was turbulence, SO_2 mixed completely by gas turbulence and diffusion, and SO_2 on any cross-section was evenly distributed. Gas velocity in scrubber tower was uniform distributed except at the boundary layer. SO_2 was absorbed completely when it came into the equipment.

The wet desulphurization tower sketch map was showed in Fig. 1, in which desulphurization tower diameter was r_b, the height was H, axes coordination was z, radial coordination was r, gas moved from down to up, absorber was sprayed from up to down.

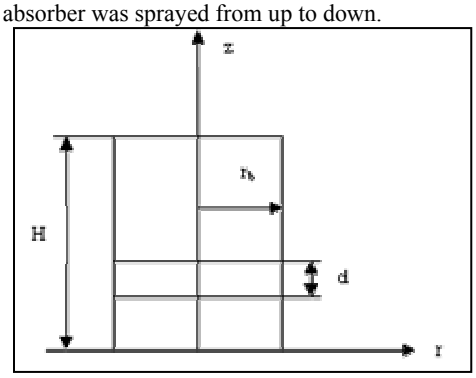

Figure 1. Sketch map of the desulphurization tower

In the z direction, any micro-volume (dv) was selected, whose section was $F(F=\pi \times r_b^2)$, length was dz, so $dv=Fdz=\pi r_b^2 dz$.

Where, F was tower cross-section area (m^2), r_b was scrubber tower diameter (m). Thus, SO_2 mass in the dv was:

$$M = C_{SO_2} dv = C_{SO_2} F dz \qquad (2)$$

Where C_{SO_2} was SO_2 concentration in dv（mg/m^3）. SO_2 mass absorbed by liquid in dt time in dv was:

$$dm = C_{SO_2} q \alpha dt dv \qquad (3)$$

Where q was absorbent spray rate in unit time (m^3/s·m^3), α was absorbing velocity coefficient (value of SO_2 concentration increasing amount in the liquid divided by flue gas SO_2 concentration).

As the SO_2 was absorbed by the absorbent liquid, its concentration in the elemental volume cell would decrease, the change was dC_{SO_2},

$$dC_{SO_2} = -dm/dv = -C_{SO_2} q\alpha dt \quad (4)$$

$$dC_{SO_2}/C_{SO_2} = -q\alpha dt \quad (5)$$

The boundary conditions were as follows:
$z=0,\ t=0,\ C_{SO_2} = C_{In}$; $z=H,\ t=t,\ C_{SO_2} = C_{Out}$.

Then, $$\int_{C_{Out}}^{C_{In}} \frac{1}{C_{SO_2}} dC_{SO_2} = -\int_0^t q\alpha dt \quad (6)$$

Then, following expression can be obtained:

$$C_{Out}/C_{In} = e^{-q\alpha t} \quad (7)$$

In which C_{out} and C_{In} were the outlet and inlet SO_2 concentration of desulphurization tower (mg/Nm^3), respectively.

$$t = H/u \quad (8)$$

Where, t was flue gas settling time(s), u was gas velocity (m/s), and H was tower height (m).

Introducing equation (3) into equation (2), we could get

$$C_{Out}/C_{In} = e^{-q\alpha H/u} \quad (9)$$

In the expression of $e^{q\alpha H/u}$, multiplying $\pi r b^2$ in denominator and numerator, respectively, and considering $\pi r b^2 u = Q$, $\pi r b^2 H = V$, thus:

$$\eta = 1 - C_{Out}/C_{In} = 1 - e^{-q\alpha V/Q} \quad (10)$$

In which, Q was flue gas rate (m^3/s), V was the effective tower volume (m^3), $V = F \cdot H$. Thus, equation (10) changed into the following form:

$$\eta = 1 - e^{-(L/Q)\alpha} \quad (11)$$

In which, L was absorbent spraying rate (m^3/s), while L/Q was liquid-gas ratio.

3.2 Outlet SO_2 concentration of desulphurization equipment. According to boiler combustion calculation, expression of the outlet SO_2 concentration of FGD equipment was as follows: [4]

$$C_{SO_2} = 2\times10^4 f S_{ar} / \left[V_y + (273+T)/273\right] \quad (12)$$

In which, f was the percent of coal sulfur which could burn (%), while S_{ar} was coal sulfur content in air received basis. T was flue gas temperature (□), and V_y was flue gas volume produced by a kilogram of coal burning (m^3/kg).

4. Calculation example and analysis

Element analysis of the calculated coal was shown in Tab. 1.

Table 1. Elemental composition of the calculated coals

Coal	Element composition, %							$Q_{ar,net}$ (kJ/kg)
	M_{ar}	A_{ar}	C_{daf}	H_{daf}	O_{daf}	N_{daf}	S_{daf}	
Xi-Shan Sub-bituminous	6.0	21.0	91.0	3.6	2.4	1.2	1.8	24720
Xu-Zhou Bituminious	10.0	15.0	82.3	5.4	8.8	1.9	1.6	24720
Huai-Nan Bituminious	6.0	21.0	81.9	5.4	10.3	1.5	0.9	24300
Jin-Zhushan Anthracite	7.0	24.0	92.5	3.2	2.6	0.8	0.9	22210

When t=80□, k=0.95, the produced SO_2 concentrations of different coal under different excess air coefficient (α) were shown in Tab. 2.

Table 2. SO_2 concentration under different α Unit: mg/m^3

α / coal kinds	1.4	1.5	1.6	1.7	1.8	1.9	2.0
Xi Shan sub-bituminous	2014	1883	1767	1665	1574	1493	1419
Xu Zhou bituminious	1878	1757	1650	1556	1471	1396	1328
Huai Nan bituminious	1076	1006	945	891	842	799	760
Jin Zhushan anthracite	1010	944	886	834	789	748	711

As can be seen from the above two tables, flue gas SO_2 concentrations produced by different coal under different excessive air coefficient differs to a fairly large extent.

By regressing with test data of wet liestone-gypsum flue gas desulphurization system of Luo-huang power plant in Sichuan province, relationship of SO_2 concentration, pH value, liquid-gas ratio(L/Q) and desulphurization efficiency were carried out, which was shown in equation (7)[5].

$$\eta = 1 - e^{1.069 - 75.3544 L/Q - 0.4983x + ky} \quad (13)$$

Where, x was the pH value, L/Q was liquid-gas ratio(m^3/m^3) $y = C_{SO_2} - 1100$ (mg/m^3); k was concentration coefficient, $k = -2.8896\times10^{-9} y + 1.7811\times10^{-4}$.

When x=5.0 and y=2270, the relation between desulphurization efficiency and liquid-gas ratio was shown in Fig. 2.

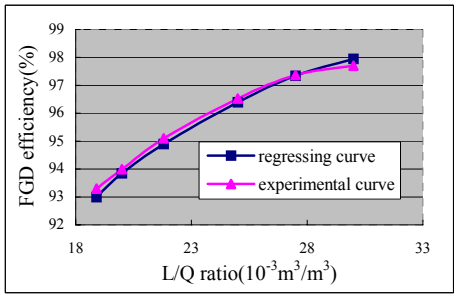

Figure 2. Relationship between FGD efficiency and L/Q

When x=5.0, L/Q=0.02, the relation between desulphurization efficiency and SO_2 concentration was shown in Fig. 3.

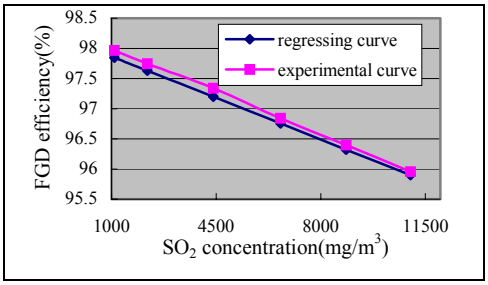

Figure 3. Relationship between FGD efficiency and SO_2 concentration

Both of the curves were well agreement with the experimental ones, and this implies that the equation could analyze and forecast the effect of boiler operation on wet flue gas desulphurization system.

5. Conclusions

Effect of power boiler combustion and operation on the wet limestone--gypsum desulphurization system was studied in this paper, and the mathematic model of FGD efficiency was established. By regression of the real FGD equipment experiment data, the relation between some factors and desulphurization efficiency was deduced. Simulation results demonstrated that these models will be very helpful for forecasting effect of power boiler burning and operation on FGD system, and supply instruction for wet desulphurization system design and operation.

References

1. Wang Z.X. countermeasures and suggestions on SO_2 discharge control for thermal power plant in China. Electric Power. 2002, 35(1): 60-63
2. GB13223-2003. Air pollutants emissions standards for thermal power plants. 2004.
3. Hao J.M., Ma G.D. Air Pollution and Control Engineering, Beijing: Higher Education Press, 1992, 330-331.
4. Fan C.Z. Power Boiler Theory, Beijing: Electricity Power Industry Press, 1985, 21-23.
5. Design construction and running of flue gas desulphurization equipment of Luo-Huang Power Plant, 1998, 10-13.

ACID LEACHING OF COAL AND COAL-ASH: KINETICS AND DOMINANT IONS

Mehtap Paul[a], Meryem Seferinoglu[b], Gul Asiye Ayçik[c], Åke Sandström[d], and Jan Paul[e]

[a]Turkish Atomic Energy Authority, Ankara Nuclear Research and Training Center, 06100 Besevler-Ankara, Turkey**.** *Present address:* Luleå University of Technology, Division of Process Metallurgy, 971 87 Luleå, Sweden.

[b]Luleå University of Technology, Division of Physics, 971 87 Luleå, Sweden *, Permanent Address:* MTA, Mineral Research and Exploration Directorate, 06520 Balgat-Ankara, Turkey

[c]Turkish Atomic Energy Authority, Ankara Nuclear Research and Training Center, 06100 Besevler-Ankara, Turkey

[d]Luleå University of Technology, Division of Process Metallurgy, 971 87 Luleå, Sweden

[e]Luleå University of Technology, Division of Physics, 971 87 Luleå, Sweden, phone +46-920-491973, fax +46-920-491074, email jan.paul@sirius.luth.se

Introduction

Acid leaching is an alternative to the conventional stabilization of ash by carbonatization or polymer induced coagulation/flocculation [1-3]. It has also been suggested that ash can replace limestone in biohydrometallurgical processing [4, 5]. Dissolved metals can be recovered from the effluent in the down-stream stages of a bioleaching process. Metals extracted at delocalized units, i.e., in separate acid leaching processes, precipitated and shipped to the main biohydrometallurgical plant as hydroxides or sulfides. The above scenario is threefold beneficial: (i) it saves limestone in the hydrometallurgical processing of sulfidic minerals, (ii) it recycles metals and (iii) it creates an inert solid ash residue. All three come with economic as well as environmental gains. The acid consumption in ash/water slurries (pH 1.0, initial S/L ratio 1:10) starts at a modest 5 L 1 M H_2SO4 per kg dry peat fly-ash and reaches 15 L /kg for bottom-ash from the combustion of wood chips and 18-24 L/kg for ash from lignites [4, 5]. Mn and Mg are regularly leached to near unity, but the yields of other dominant elements - K, Na, Al and Fe - vary, probably due to the presence of stable oxides.

The current work shows the time dependencies of acid consumption and elemental compositions in the aqueous phase for four ashes and the kinetics of acid consumption of an additional 10 coal-ashes and whole coals. Time dependent studies can link acid consumption to the dissolution of major ash components and correlate trace element extraction to the destabilization of certain major phases [6]. This is the topic of a subsequent paper [7]. The current work forms a platform to discuss residence times and process designs for an industrial process.

Experimental

Coals. 13 Turkish coals were selected [5]. The majority of the coals were also included in the MTA project 'Türkiye Linyitlerinin Teknolojik ve Kimyasal Özellikleri Envanteri Projesi' (*Eng. Project for the inventory of technological and chemical properties of Turkish lignites*) [8, 9].

Untreated Ashes. Ash from the combustion of sawmill residues was collected at the Fränsta plant (http://www.angeenergi.se) and used as received [4]. Ashes from lignite combustion of lignites were prepared from the untreated fuels as described [5]. 'As prepared' ashes were analyzed by ICP-AES/MS/SMS (Analytica AB, www.sgab.se, procedure MG-2 plus additional elements). Our untreated ashes resemble, with respect to the metal content, the primary fly-ash, rather than the secondary fly-ash, used in a previous leaching study of ash from a waste incineration unit [17].

Acid Consumption. Dry ash was mixed (solid : liquid 1 : 10, by weight) with deionized water (Millipore Milli-Q, >18 MΩcm) and the slurry stirred overnight (> 12 h). pH was reduced to 1.0 by the addition of 1 M H_2SO_4 (VWR International, *pro analysi*). pH was maintained by the subsequent additions of 1 M sulfuric acid. We report the accumulated acid vs. time.

The results of akin experiments with whole coals are also reported. The coals were dried in air for 24 h at 40 EC and ground in a ball mill [5]. We selected the 250-1000 µm fraction for the present experiments.

Time Dependence. A homogenized batch of ash was divided into 8 or 16 samples, each weighing around 5.0 g. Some experiments were also performed with batches of around 50 g ash. One sample, at a time, was mixed with deionized water (S/L 1:10) and stirred as described. Within minutes the pH was lowered to 1.0 and maintained by the subsequent additions of 1 M H_2SO_4. Leaching was terminated by the separation of effluent and solid residue after 30 min (Munktell OOR filter paper). Filtration was completed within 30-40 s. The volume of the effluent was measured and a sample taken aside for ICP-AES/MS/SMS analysis (Analytica AB, www.sgab.se, procedure V3a plus additional elements). The experiment was then repeated for a new stopping time, with a fresh sample from the homogenized batch. We report analyses of the aqueous phase after 30 min, 1 h, 2 h, 4 h, 8 h, 16 h and 32 h of leaching. The results are compared with the results from our previous screening study of maximum extraction, i.e., with the concentrations after 10 days of continuous leaching in sulfuric acid at pH 1.0 [4, 5].

Results

Time Dependence of Acid Consumption. The accumulated volume of 1 M H_2SO_4 is needed to maintain pH 1.0 in coal and coal-ash slurries at 25 EC. With initial solid / liquid ratios of 1:10, which represent an upper limit. We have not varied this ratio, but assume from literature that it can be reduced to ca. 1:5 without altering the data [18]. The results for whole coals are displayed after division with the fraction of non-combustible material. The 'ash' fractions were taken from our small-scale preparations rather than averaged bulk values [5]. The 'ash' fraction do carry some uncertainty and we find it superficies to base discussion on changes in the inorganic portion of coal during combustion solely on a comparison of absolute acid consumption values. The time dependencies of whole coals and coal-ashes are markedly different. Initially, the whole coals consume acid very rapidly, but the consumption cease after less than 1/2 a day. Coal-ashes are characterized by a smaller initial acid consumption, followed by a second slower stage, extending over several days.

Initially, significant gas quantities evolved when acid was added to the slurry with ash from Fränsta. This leads to enhanced agitation and is an indication of strong carbonatization in the untreated ash. Little gas evolved during the leaching of ash from Silopi, Yata□an and Tunçbilek.

Leaching of Elements. We have analyzed the behavior of four ashes in detail: one wood-ash (Fränsta), two lignite-ashes (Mu□la-Yata□an and Kütahya-Tunçbilek) and one asphaltite-ash (Silopi). Table 1 gives the concentrations of dominant elements in the

untreated. Our analysis is based on the concentrations of ions in the aqueous phase and anomalous values X > 1 stem from samples variations and analysis uncertainties. We neglect silicon/silicic acid in solution [4, 5, 19, 20].

Discussion

Acid is consumed when parts of the untreated ash are dissolved. There is a time dependence during the first 32 h of leaching. We derive the amounts of sulfuric acid and compare these with the measured amounts of sulfur in solution. We also calculate the corresponding amounts of consumed protons from the concentration of Ca^{2+}, Fe^{3+}, K^{+}, Mg^{2+}, Na^{+}, PO_4^{3-}, Al^{3+} and Mn^{2+} in solution. This is a simplified model for the neutralizing capacity of ash [21], but it works to illuminate the role of different ash components and some anomalous behavior.

Sulfur in the solid residue is very well correlated to the concentration of Ca, Ba and other elements forming insoluble sulfates [4], but the consumption of acid is poorly explained solely by the formation of sulfate residues. Fränsta has a high neutralizing capacity, but a low concentration of sulfur in solution due to the formation of gypsum - only 12 % of Ca is dissolved after extended times. Fränsta has literally no sulfur in the untreated ash. Other metals from major components - Fe, K, Mg, Na, P, Mn - are leached to between 80 - 100 %. Aluminum alone is leached to a lesser degree (68 %). This indicates the presence of stable, Al containing (complex) ceramics, possibly the result of the combustion process.

Yatagan has a high sulfur concentration in the untreated ash, and the concentration in the solid phase increases further by about 50 %, following leaching in sulfuric acid. Ca appears to form insoluble $CaSO_4$, with only 18 % dissolved. Other elements, notably Fe, K and Na, are leached to less than 50 %, again indicating stable oxides, and we note that clays and other stable minerals are mined with the organic phase. Mn and Mg are leached completely, as expected of the carbonates and simple oxides.

Tunçbilek is actually depleted of sulfur during leaching in sulfuric acid. Ca, not very abundant in the untreated material, is almost completely extracted during leaching. Significant portions of other elements - Fe, K, Na, Al - remain in the solid phase, a strong indication that stable minerals are mixed with combustible phases, in the fuel. The current ashing temperature, 550 EC, is suitable for trace element studies and does not promote the formation of mixed oxides during combustion [5, 22]. Mg and Mn are again leached to near completion.

Finally, Silopi untreated ash is rich in sulfur, and the level increases by 30 % during leaching. Ca is leached to 23 % and Mn and Mg to near unity, but Fe, K, Na and Al are only dissolved marginally. Again stable minerals (clays, feldspars etc.) [23], mined together with the organic material, may explain the low figures.

Coals vs. Coal-ashes. Positively identified is a different time dependence for the acid leaching of coals and coal-ashes. Initially, coals consume acid at a very high rate. Within the first few minutes 60-87 % of the acid is spent, so we could not resolve details of the time dependence for this portion of the experiments. We note that Mg and Mn are leached to high percentages and there is no apparent difference between coals and coal-ashes [5]. The remaining acid is consumed during the next 3-9 h. No acid was added to the coal slurries after 10 h. We interpret the above as the dissolution of relatively small grains of inorganic material supported on a very permeable organic matrix. This agrees with the dispersion of clay minerals as finely dispersed inclusions in the coal [24].

The maximum extraction of aluminum is always higher after ashing than in the ground whole coals [5]. We suggest the possibility that the organic phase shields aluminum containing oxides from the surrounding aqueous phase. It is known from catalysis that carbonaceous residues readily form on such surfaces [25, 26]. This translates to high surface energies and makes it plausible to suggest that the organic phase in coals wets the surfaces of minerals with a high aluminum or iron content.

Silopi asphaltites are different from lignites. Only 42 % of the total acid is consumed within the first minutes and the following slower period stretches over a much longer time than 10 h. The 'ash' content - 36 % - is higher than for any of the lignites [5], which makes it feasible that the leaching is influenced by ground minerals. A different and lower permeability may also influence the time dependence [27, 28]. Silopi asphaltites are known to be denser and less fissured than Turkish lignites (MTA Geology Dept.).

The data motivates a residence time of 10 h for coals with particle sizes in the 250-1000 μm range. 10 mm particles will increase the necessary residence time with a factor 2-5, i.e., to 1-2 days [29], but current lumps for domestic use in Turkey, 18-50 mm, may give inconveniently long leaching times.

Kinetics of Ash Leaching. The kinetics of acid consumption for ashes indicated an initially fast process, followed by a slower period, possibly extending longer than 10 days (14400 min). Below, we analyze acid consumption as well as the concentration of ions from dissolved major ash components - Ca, Fe, K, Mg, Na, P, Al and Mn - in the two regimes.

The neutralizing capacity of the ashes, phrased as the total charge of ions in solution can be seen as well as the parallel behavior of acid consumption and the total charge of Ca^{2+}, Fe^{3+}, K^{+}, Mg^{2+}, Na^{+}, PO_4^{3-}, Al^{3+} and Mn^{2+} ions. We choose to display values for 16 h as well as 32 h. Note that neither set includes the initial 30 minutes. It is clear that the dissolution of different solid components are responsible for the neutralizing capacity during the initial contact (< 30 min) and the extended leaching (30 min - 16/32 h). It is likewise clear that the ashes of wood and coals are different.

Fast Regime. The initial neutralizing capacity of ash from sawmill residues (Fränsta) is dominated by Ca, K and Mg. This is a general observation for biofuels: straw, hard- and softwood, and in particular bark [30, 31], but the high neutralizing capacity is not found in peat [4]. The observed gas evolution indicates a high concentration of carbonates in the untreated ash. Time dependent data for Ca, K and Mg shows that the concentration of these ions quickly reach stable values, corresponding to the very rapid dissolution of Ca, K and Mg compounds. Whereas K and Mg are stable in solution, calcium and sulfate ions favor gypsum formation. The atomic ratios for dissolved Fränsta ash in the initial period (< 30 min) were Fe/Al 1 : 6, K/Al 15 : 1 and Na/Al 2 : 3. This reflects the ratio between simple oxides and carbonates rather than the stoichiometry of complex ceramics. Complex ceramics with Al are expected to form at combustion temperatures above 800 EC [32].

Yatagan and Tunçbilek are similar with respect to major components and represent ash from lignite combustion. The initial neutralizing capacity comes from Ca, Mg and Al. Ca and Mg quickly reach stable concentrations, at intermediate levels, but the Al fraction in solution continues to increase. We suggest the possibility of a mixture of Ca, Mg and Al compounds in the untreated ashes, but note that particle size distributions as well as solubilities will effect the profile [33-36]. The tentative second phase containing Ca and Mg is hardly leached, but the second Al containing phase is dissolved at a slow pace.

Silopi ash constitutes its own entity, separate from bio-ash or ash from lignites. The initial neutralizing capacity comes from Ca and Mg. Mg is almost completely dissolved after a short contact time, but Ca reaches an intermediate level, suggesting the possibility of two calcium containing phases in the untreated ash, one stable and one easily dissolved.

Slow Regime. As the initial phase passes, the center of importance for the neutralizing capacity shifts to new compounds in the ashes. Mg and K are still important for sawmill residues (Fränsta), but many elements contribute with Mn dominating. Momade and Momade observed a similar profile for Mn leaching from manganese oxide ore, and extended the study to the positive effects of methanol addition (< 40 %), stronger acids (< 0.3 M), higher temperatures (< 170 EC) and smaller particles (< 32 μm) [37]. Manganese carbonates are abundant in coals [38], but our data suggests that other forms also are present in the ashes.

There is a time dependence for the fraction (X) of dissolved magnesium and aluminum, interpreted by the (simplified) solution to the Elovich equation [35, 37, 39]:

$$X = a \bullet \ln(t) + b \qquad (1)$$

Lignite-ashes from Yatagan and Tunçbilek constitute a separate group. Al and Fe are dominant contributors in the 30 min - 32 h regime and the time dependencies are well modelled by a SCM process [7]. We use the expression for a product layer / diffusion controlled process [34]:

$$1 - 3 \bullet (1-X)^{2/3} + 2 \bullet (1-X) = c \bullet t \qquad (2)$$

in agreement with previous studies [37] and note that self-inhibition by the precipitation of gypsum or $MnSO_4$ as diffusion barriers, have been reported [39-41]. The above expression gives a better fit than expressions for a surface controlled process [34]. We have not exploited more elaborate idioms [36, 39], nor models for surface reaction and diffusion controlled processes [34, 42].

We conclude that the neutralizing capacity of lignite-ash in the 30 min - 32 h regime is controlled by the dissolution of particles. During the first few hours magnesium is still dissolved, but this ceases, while iron and aluminum continue to be leached. Sodium and potassium are leached, but it is unclear if the ratio of cations in a tentative mineral with aluminum can be derived.

[36, 39], nor models for surface reaction and diffusion controlled processes [34, 42].

We conclude that the neutralizing capacity of lignite-ash in the 30 min - 32 h regime is controlled by the dissolution of particles. During the first few hours magnesium is still dissolved, but this ceases, while iron and aluminum continue to be leached. Sodium and potassium are leached, but it is unclear if the ratio of cations in a tentative mineral with aluminum can be derived.

The Fe/Al atomic ratio for dissolved Yatagan lignite-ash was 1:7 in the initial period (< 30 min) as well as during the extended leaching regime (30 min - 32 h). Only small amounts of potassium (K/Al 3:100) and sodium (Na/Al 2:100) were leached after the first 30 min. The Fe/Al ratio for dissolved Tunçbilek lignite-ash was 1:5 at all times, i.e., during the initial (< 30 min) as well as the extended (30 min - 32 h) leaching period. The K/Al ratio was 10:100 (approx.) and the Na/Al ratio 2:100 towards the end of the 'slow regime', down from K/Al 20:100 (approx.) and Na/Al 10:100 in the initial period. These values may be compared with the stoichiometries of common minerals [43].

The fixed Fe/Al ratio suggests dissolution of a clay mineral (illite) [24, 43-45]. We can not discern the presence of montmorillonites, a class of iron containing clays, which swell in water, due to their sheet-like structure. This makes them feasible as inherent (liquefaction) catalysts, either by sulfidation of the metals in the coal or by adsorbing metal ions from aqueous solutions, followed by treatment in H_2S [46].

The Fe/Al ratio of elements leached from Silopi asphaltite-ash changed from 1:10 during the initial (< 30 min) period to 1:2 after 32 h. The altered ratio infers that more than one mineral is leached, albeit with comparable yields. Mn and Mg follow similar profiles, but the ratio to Al is not constant, nor to Fe. We suggest a combination of clay and carbonate association [24, 43, 44]. The initial K/Al and Na/Al ratios for Silopi were both 1:5, but diverged to slightly higher potassium concentration and slightly lower sodium concentration after 16 h or 32 h. Na occurs in several minerals [43], but association is sometimes difficult to discern [45]. Potassium and sodium containing clays are abundant, but feldspars have also been observed [23].

Whereas carbonates are expected to contribute mainly in the 'fast regime', clays and feldspars dissolve slowly. Complex oxides, with well defined structures and stoichiometries, are formed at high temperatures and observed as narrow areas in phase diagrams. These structures have high resistance to leaching. The effect is well illustrated by aluminum minerals. Aluminum was extracted to near 100 % from Bayerite / $Al_2O_3 \bullet 3H_2O$ in sulfuric acid [36]. More complex aluminum/silicon oxides showed higher stability. Kaolinite / $Al_2O_3 \bullet 2SiO_2 \bullet 2H_2O$, one common clay mineral in coal [24], was leached effectively after calcination at 500-600 EC, i.e., conditions similar to the present ashing procedure [36]. Illite / $K_2O \bullet 3Al_2O_3 \bullet 6SiO_2 \bullet H_2O$ was leached to a lower percentage, again after calcination [36]. Finally, mullite / $3Al_2O_3 \bullet 2SiO_2$, the most stable aluminum silicate and a typical product after high temperature treatment, i.e., in ash residues from power plants, showed high resistivity to sulfuric acid leaching [36, 47]. Feldspars - alkali, (K, Na)$AlSi_3O_8$, and plagioclase, $NaAlSi_3O_8$ to $CaAl_2Si_2O_8$, - constitute additional, often stable minerals [43]. These minerals are observed as minority phases in coal [24]. We note that crystallinity is a key factor [48] and poor crystallinity/amorphous material [45] and prolonged wetting [49] may significantly alter extraction yields.

Mg and P are major contributors to the neutralizing capacity of Silopi asphaltite-ash and, together with manganese, dissolved to high percentages. Other elements - Al, Na, Fe and K - contribute less to the neutralizing capacity, but are still leached according to a SCM / diffusion model, except during the initial hour [7]. It appears that the initial regime extends to 1 h, compared with 30 min or less for the lignite-ashes. A similar knee was observed in the graphical representation of Al, Fe and Mg dissolution in sulfuric acid from waste incineration fly-ash [17].

We note that acid consumption during leaching of Silopi 'whole coal' was different than acid consumption during akin leaching of lignite whole coals and we suggest that more original mineral matter contribute for Silopi asphaltite-ash than for Yatagan and Tunçbilek lignite.

Whole Coal' Processing. Acid washing of whole coals is motivated when no aftertreatment of flue gases or ash residues is feasible, i.e., for domestic heating in less developed countries. Improved design of stoves is important (http://www.laowan.com), but the long lifetime of such units leaves no alternative to improved fuel quality [50]. Catalytic gas conversion [51, 52] is not a realistic option in the areas where low rank coals are the dominant fuel for domestic heating.

Our results show that 10 h of leaching (1 M H_2SO_4, 25 EC) gave a near complete removal of acid-consuming parts of 12 Turkish lignites (whole coals). The results were obtained for 250-1000 μm size particles. Literature indicates 2-5 times longer time for 10 mm particles [29]. Continued tests need to refine these claims in bench or pilot plant operations of feasible process designs [5, 53]. Current commercial lumps (in Turkey 18-50 mm) should be tested, but indications are that the necessary combustion tests must address the effects of an altered particle size distribution (to < 10 mm), as well as heating values and the quality of flue gases and ash residues. Simultaneous acid leaching and biodesulfurization of coal in the

bioleaching stage of a process for metal production from sulfidic concentrates may be of interest.

Acid washing of whole coals is also of interest for preprocessing before liquefaction. During coal liquefaction the coal structure is thermally decomposed in the presence of hydrogen. Atomic hydrogen terminate thermally broken carbon-carbon bonds. Atomic hydrogen is produced on metalsulfide (Mo, Co, Ni, W, Fe) catalysts and, pending the dispersion of the catalyst, either used directly or carried by a transporting molecule to the organic part. Catalyst precursors are commonly adsorbed as metal ions from aqueous solutions, thus preferentially on polar sites, and then sulfided.

Removal of a large fraction of the 'ash' part, by acid leaching, will remove many polar sites, apart from the organic structure, and thus shorten the diffusion path of atomic hydrogen. Removal of non-combustible phases will also enhance the permeability [54] during the liquefaction process, and limit the volume of solid residues. Acid preprocessing, followed by normal hydrotreatment, constitutes an alternative to unconventional supercritical processing [28].

Conclusions

Extraction kinetics indicated that lignites are ideally suited for direct acid leaching (H_2SO_4, pH 1.0, 25 EC). We estimate that 2 days constitute a suitable time for the preparation of 'clean' coals (< 10 mm) for domestic use. Asphaltites require considerably longer residence times.

Lignites are ideally suited for treatment in the biological oxidation stage of a hydrometallurgical process for the production of metals from sulfidic concentrates. The biocatalyzed oxidation of sulfidic minerals is also one and the same reaction as biodesulphurization of coals. Coals, washed in the bioleaching stage, will emerge with lower sulfur, 'ash' and trace element contents. The washed product is intended for domestic stoves. Two technical obstacles remain and need to be addressed: (i) the low neutralizing capacity of coal require 5-10 times larger masses compared with CaO and (ii) readsorption and precipitation onto the washed coal must be prevented.

Lignite- and asphaltite-ashes consume acid during ca. 10 days. We discern a 'fast regime' ending after 30 min and dominated by the release of Ca, Mg, K and Al ions, probably from carbonates and simple oxides, but possibly also from small particles or poorly crystalline complex minerals and oxides. A second, 'slow regime' for ashes is well modelled by a diffusion limited shrinking core (SCM) process. Several minerals contribute to the neutralizing capacity in this regime and we observe the leaching of Fe, Al, K, Na and Mn.

Acknowledgement. We thank our colleagues Agah Köker and Selami Toprak from MTA in Ankara for discussions on coal pretreatments. We also thank Ömer Ünver from TKI Türkiye Kömür Isletmeleri Kurumu *(Eng. Turkish Coal Enterprises*) for his continued interest in our work and Michael L. Smith, Anabolic Laboratories, Phoenix/AZ for his careful reading of the manuscript. Last, but not least, we acknowledge Vattenfall AB and Ånge Energi for their support of our project.

References

(1) Querol X., Uma□a J.C., Alastuey A., Ayora C., Lopez-Soler A., Plana F., Fuel 2001; 80; 801
(2) Chandler A.J., Eighmy T.T., Hartlén J., Hjelmar O., Kosson D.S., Sawell S.E., van der Sloot H.A., Vehlow J., Municipal Solid Waste Incinerator Residues, Study in Environmental Science 67 (Elsevier, 1997, Amsterdam)
(3) Katsuura H., Inoue T., Hiraoka M., Sakai S., Waste Management 1996; 16; 491
(4) Paul M., Sandström Å., Paul J., Journal of Hazardous Materials (submitted)
(5) Seferino□lu M., Paul M., Sandström Å., Köker A., Toprak S., Paul J., Fuel 2003; 82; 1721
(6) Harris W.R., Silberman D., Environ. Sci. Technol. 1983; 17; 139
(7) Paul M, Seferinoglu M., Aycik G.A., Sandström Å., Paul J., Fuel (submitted)
(8) MTA Enstitüsünce Bilinen Türkiye Yeralti Kaynaklari Envanteri, No.168, (MTA, Ankara, 1977), *in Turkish*
(9) Tuncal2 E., Çifci B., Yavuz N., Toprak S., Köker A., Ayçik H., Gençer A., Sahin N., Chemical and Technological Properties of Turkish Tertiary Coals, (MTA, 2002, Ankara)
(10) TMMOD, 2000'li Yillarda Ulusal Enerji Politikalari, TMMOD Elektrik Mühendisleri Odas2 Birli□i, December 1999, p.93, *in Turkish*
(11) Karayigit A.I., Whateley M.K.G., Int.J.Coal.Geol. 1997; 34; 131
(12) Gayer R.A., Karayigit A.I., Goldsmith S., Onaçak T., Rose M., Proceedings 8th Austalian Coal Science Conference, (Australian Institute of Energy, 1998, Toukley)
(13) Querol X., Alastuey A., Plana F., Lopez-Soler A., Tuncali E., Toprak S., Ocakoglu F., Köker A., Int.J.Coal.Geol. 1999; 41; 311
(14) Toprak S., Alpagut-Dodurga (Osmancik - Çorum) Bölgesi Çevresindeki Kömürlerin Olusum Ortamlari ve Özelliklerinen Belirlenmesi' (*Eng. Determination of depositional environments and properties of coals located in the vicinity of Alpagut-Dodurga (Osmanc2k - Çorum) region)*, Doctoral Thesis, (Hacettepe University, 1996, Ankara), *in Turkish*
(15) Atamer H., Derman D., Özdil G., 1975, Güneydogu Anadolu Bölgesi Asfaltit Küllerinden Molibden, Nikel, Vanadyumun ve Uranyumum Kazan2lmas2, M.T.A. Enstitüsü Teknoloji Dairesi Radyoaktif ve Nadir Metaller Teknoloji Servisi, Ankara, *in Turkish*
(16) Atamer H., Özdil G., Essiz R., Durmus H., 1979, Güneydogu Anadolu Bölgesi Asfaltit Küllerinden Molibden, Nikel ve Vanadyumun Kazanilmasi Amaciyla Liçing Ara□t2mas2, MTA 6636, M.T.A. Enstitüsü Teknoloji Dairesi Radyoaktif ve Nadir Metaller Teknoloji Servisi, Ankara, *in Turkish*
(17) Nagib S., Inoue K., Hydrometallurgy 2000; 56; 269
(18) Vitolo S., Seggiani M., Filippi S., Brocchini C., Hydrometallurgy 2000; 57; 141.
(19) Iyer R., Journal of Hazardous Materials B 2002; 93; 321
(20) Jia C.Q., Xiao J.Z., Orr R.G., J. Environ. Sci. Health, Part A: Toxic/Hazardous Substances & Environmental Engineering 1999; 34; 1013
(21) Jinying Y., Moreno L., Neretnieks I., J. Environ. Sci. Health, Part A: Toxic/Hazardous Substances & Environmental Engineering 1998; 33; 923
(22) Finkelman R.B., Palmer C.A., Krasnow M.R., Aruscavage P.J., Sellers G.A., Dulong F.T., Energy & Fuels 1990; 4; 755
(23) Karayi□it A.I., Querol X., Energy Sources 2002; 24; 703
(24) Stach E., Mackowsky M.Th., Teichmüller M., Taylor G.H., Chandra D., Teichmüller M., Stach's Textbook of Coal Petrology, 2nd Ed., (Gebrüder Borntraeger, 1975, Berlin), pp. 122
(25) Gray M.R., Zhao Y., McKnight C.M., Komar D.A., Carruthers J.D., Energy & Fuels 1999; 13; 1037

(26) Manju C.S., Lalithambika M., Nair V.N., Clays and Clay Minerals 2001; 49; 355
(27) Clarkson C.R., Bustin R.M., Int. J. Coal Geol. 1997; 33; 135
(28) Erol M., Demirel B., To□rul T., Çal2ml2 A., Fuel Proc. Technol. 1995; 41; 199
(29) Couch G.R., Advanced Coal Cleaning Technology, CR/44 (IEA Coal Research, 1991, London)
(30) Steenari B.M., Schelander S., Lindqvist O., Fuel 1999; 78; 249
(31) Obernberger I., Biedermann F., Widmann W., Riedl R., Biomass and Bioenergy 1997; 12; 211
(32) Steenari B.M., Lindqvist O., Biomass and Bioenergy 1998; 14; 67
Beloborodov V.V., Voronenko B.A., Inzhenerno-Fizicheskii Zhurnal 1997; 70; 685 (*in Russian*)
(33) Levenspiel O., Chemical Reaction Engineering, (John Wiley, 1999, New York)
(34) Stumm W., Morgan J.J., Aquatic Chemistry: Chemical Equilibria and Rates in Natural Waters, 3rd Ed., (Wiley, 1996, New York)
(35) Fernandez A.M., Ibá□ez J.L., Llavona M.A., Zapico R., in Light Metals, Proceedings of the 127th TMS Annual Meeting, Feb 15-19 1998, San Antonio, TX, USA, Ed. B, Welch, pp. 121
(36) Momade F.W.Y., Momade Z.G., Hydrometallurgy 1999; 54; 25
(37) Davidson R.M., Modes of Occurrence of Trace Elements in Coal - Results from an International Collaborative Programme, CCC/36, (IEA Coal Research, 2000, London)
(38) Seidel A., Zimmels Y., Chem. Eng. Sci. 1998; 53; 3835
(39) Seidel A., Sluszny A., Shelef G., Zimmels Y., Chem. Eng. J. 1999; 72; 195
(40) Momade F.W.Y., Hydrometallurgy 1996; 40; 123
(41) Ahmed I.B., Gbor P.K., Jia C.Q., 2000, Aqueous sulphur dioxide leaching of Cu, Ni, Co, Zn and Fe from smelter slag in absence of oxygen, Can. J. Chem. Eng. 2000; 78; 694
(42) Hurlbut C.S. Jr., Klein C., Manual of Mineralogy (after James D. Dana) 19th Ed., (John Wiley, 1977, New York)
(43) Berkowitz N., An Introduction to Coal Technology, 2nd Ed., (Academic Press, 1994, San Diego) pp. 46
(44) Palmer C.A., Filby R.H., Fuel 1984; 63; 318
(45) Artok L., Malla P.B., Komarneni S., Schobert H.H., Energy & Fuels 1993; 7; 430
(46) Schneider H., Okada K., Pask J., Mullite and Mullite Ceramics, (John Wiley, 1994, Chichester)
(47) Öhman L.O., Wågberg L., J. Pulp and Paper Sci. 1997; 23; J475
(48) Laiti E., Persson P., Öhman L.O., Langmuir 1998; 14; 825
(49) Unterberger S., Berger R., Maier H., Hein K.R.G., Norin B., Gaegauf C., Struschka M., Hyytiäinen H., 1998, Development of newly designed wood burning systems with low emissions and high efficiency, Final Report EU Joule III, Institute of Process Engineering and Power Plant Technology, University of Stuttgart, Germany
(50) Ferrandon M., Berg M., Björnbom E., Catalysis Today 1999; 53; 647
(51) Hannay D.P., Franklin H.N., Effect of design upon selective catalytic reduction system operation, in Proceedings of the 1997 International Conference on Power Generation, POWER-GEN, (PennWell, 1997, Tulsa) p.71
(52) Osborne D.G., Coal Preparation Technology, (Graham & Trottman, 1988, London)
(53) Güvenç A., Erol M., Çalimli A., Sarikaya Y., Fuel Processing Technol. 1994; 38; 211

Table 1. Concentrations in Untreated Ash

Element [mg/kg]	Fränsta/ sawmill residue	Yatagan/ lignite	Tunçbilek/ lignite	Silopi/ asphaltite
Ca	314510	187991	14296	162973
Fe	5511	40289	87428	32523
K	66632	5012	10787	26387
Mg	34732	25265	22310	26290
Na	2426	1313	1054	2404
P	5720	1044	1546	4890
Al	8682	55588	96353	38171
Mn	37931	803	1353	116
S	3920	118000	25400	97600

ACID LEACHING OF ASH FROM WOOD, ASPHALTITE AND LIGNITE COMBUSTION: TRACE ELEMENT OCCURRENCES

Gul Asiye Ayçik[c], Mehtap Paul[a], Meryem Seferinoglu[b], Åke Sandström[d], and Jan Paul[e]

[a]Turkish Atomic Energy Authority, Ankara Nuclear Research and Training Center, 06100 Besevler-Ankara, Turkey**.** *Present address:* Luleå University of Technology, Division of Process Metallurgy, 971 87 Luleå, Sweden.

[b]Luleå University of Technology, Division of Physics, 971 87 Luleå, Sweden *, Permanent Address:* MTA, Mineral Research and Exploration Directorate, 06520 Balgat-Ankara, Turkey

[c]Turkish Atomic Energy Authority, Ankara Nuclear Research and Training Center, 06100 Besevler-Ankara, Turkey

[d]Luleå University of Technology, Division of Process Metallurgy, 971 87 Luleå, Sweden

[e]Luleå University of Technology, Division of Physics, 971 87 Luleå, Sweden, phone +46-920-491973, fax +46-920-491074, email jan.paul@sirius.luth.se

Introduction

Trace element extraction, followed by metal recovery, offers a route to sustainable ash handling, and may become an alternative to conventional stabilization and deposition. Direct acid leaching at low pH is a most powerful first step, albeit additional steps, including strong bases or chelating agents [1-4], may be needed, if the solid residue should be cleaned of all environmentally harmful elements. The trace elements; Cd, Cu, Co, Ni, Th, U, V and Zn, are leached to high percentages in sulfuric acid (pH 1.0, initial S/L ratio 1:10 25 EC) [5, 6]. Biohydrometallurgical production of base metals, i.e., the bacteriological oxidation of dominant mineral sulfides, offers established procedures for the recovery of several metals and gives directions for others.

Data for maximum extraction [5, 6] need to be amended with the results of time dependent studies before residence times and process designs can be discussed. Time dependent studies can also correlate trace element extraction to the dissolution of dominant ions [7] and the destabilization of major phases. It is not trivial to reveal the chemical nature of trace elements in the untreated ash by direct physical observation [8], but correlation studies, optionally using several leachants [9], offer a feasible, albeit indirect, route.

Experimental

Ash from the combustion of sawmill residues was collected at the Fränsta plant (http://www.angeenergi.se) and used as received [5]. Ashes from the combustion of two lignites, Mu la-Yata an and Kütahya-Tunçbilek, and one asphaltite, Silopi (http://www.tki.gov.tr), were prepared from the untreated fuels as described [6]. The untreated ashes were analyzed by ICP-AES/MS/SMS (Analytica AB, www.sgab.se, procedure MG-2 plus additional elements). Table 1 displays trace element data. Data for dominant ions were reported in a previous communication [7].

Ash samples were divided, stirred in deionized water and forcefully leached at pH 1.0 by the addition of 1 M sulfuric [7]. The effluent was analyzed by ICP-AES/MS/SMS analysis (Analytica AB, www.sgab.se, procedure V3a plus additional elements). We report analyses of the aqueous phase after 30 min, 1 h, 2 h, 4 h, 8 h, 16 h and 32 h leaching. The results are compared with the results from our previous screening study of maximum extraction, i.e., with the concentrations after 10 days of continuous leaching in sulfuric acid at pH 1.0 [5, 6].

Results

Table 1 gives trace element concentrations in the untreated materials and the extracted fractions of the same ions during leaching in sulfuric acid can also be seen (H_2SO_4, pH 1.0, 25EC, Initial solid/liquid ratio 1:10). Akin data for dominant ions were disclosed in a previous publication [7]. Our analysis is based on the concentrations of ions in the aqueous phase and anomalous values X > 1 stem from samples variations and analysis uncertainties.

We excuse the Fränsta ash. Table 1 reveals low levels of literally all relevant trace elements and maximum extraction figures have been presented [5]. Fränsta ash is contaminated by some radioactive elements, particularly Cs-137 from softwood exposed to long-range pollutants (Chernobyl), but also natural Ra-226. We have investigated the possibility to leach these pollutants [11], albeit the activity of our sample was below 5000 Bq/kg, the legal limit for the use as forest fertilizer (http://www.ssi.se).

There is a time dependence of trace element extraction for lignite-ash (Mu la-Yata an and Kütahya-Tunçbilek) and asphaltite-ash (Silopi). We have deliberately chosen to display the data in the same SCM model as for the major components. The purpose was to compare profiles and identify patterns which will reveal the matrices surrounding particular trace elements, i.e., occurrences. One difference is that we include the values for 30 min leaching.

Discussion

Trace Element Leaching and Occurrences.

Arsenic. Maximum extraction yields between 27-81 % for ground coal and 24-77 % for coal-ash have been reported [6]. We note that only marginal quantities are leached from ash after the initial period. It has been suggested that As is associated with $CaSO_4$ [12] and our results do not contradict these findings.

Barium. Bariumsulfate is nearly insoluble and barium, dissolved from phases in the untreated ash, is readily altered to barite in the solid residue [5, 6]. We were able to observe the early stages of leaching from Silopi ash, despite the stability of $BaSO_4$. The plateau corresponds to 26 µg / L or 1 % extraction. Ba forms carbonates, but replaces also alkali metals or alkaline earths in Si/Al oxides [13]. The traces of sodium and barium are two of a kin, albeit many elements in show a similar increase during the first 4 h.

Cadmium. Silopi ash gave an approximate straight line in the entire regime. Cd associated with mineral sulfides will be altered during combustion. We note that cadmium is extracted to better than 90 % in most ashes, notably from waste incineration [5], but significantly less in whole coals [6]. The present data give 94 % Cd extraction for Silopi asphaltite-ash and 100 % for Fränsta / bio-ash, but only 30-40 % for lignite-ashes. This is at the low-end of compiled data for coal-ashes [6] and shows that dissolution continuous after 32 h, for cadmium, as well as for aluminum and iron [7], two possible host elements. Lignite combustion may also lead to the formation of insoluble spinels, akin to the formation of $ZnFe_2O_4$ from the oxidation of (Fe, Z)S or reactions between zinc oxide and hematite [14]. Association with iron or zinc containing oxides [9, 15], formed from FeS_2 or ZnS, may protrude as a similarity with Fe or Zn leaching. In conclusion, we need extended process times to deplete coal-ashes of cadmium. The rapid dissolution from waste-ashes is probably a result of surface association [16].

Cobalt. It is unclear if cobalt leaching follows a SCM model. Extraction reaches 29-44 % after 32 h, which is lower than 40-82 % after 10 days [6]. No occurrence is universally favored in literature [15], albeit association with clays has been suggested [9, 17].

Chromium. All ashes show smooth profiles but only Silopi approaches maximum extraction after 32 h i.e., the apparent plateau for Tunçbilek is artificial. The iron and aluminum profiles for Silopi ash, as well as the degree of completion [6, 7], mimic the chromium behavior, in all suggesting clay association, in agreement with literature [17]. Organic occurrences in 'whole coals' [9] and the heat during combustion, may lead to association with other oxides, apart from clay minerals. The above analysis applied anew, for Yata□an and Tunçbilek lignite-ashes, recognizes the close similarities between Cr and Fe/Al kinetics of leaching as well as the proximity to maximum extraction [6, 7]. During leaching (30 min - 16 h) the Cr / Fe atomic ratios were 1:420 (Yata□an), 1:53 (Tunçbilek) and 1:32 (Silopi). The Cr / Al ratios were 1:2900 (Y), 1:160 (T) and 1:380 (S), respectively. These values serve to illuminate the degree of doping, assuming solid solutions. In conclusion we suggest that Cr is found as a dopant in iron and aluminum oxides, i.e., probably in illite clays.

Cesium. Low concentrations are an obstacle for trustworthy data on Cs leaching of coal-ash, but measurements on radioactive Cs-137 in wood-ash indicated a very rapid process (< 30 min) with high extraction yields (>90 %) [11].

Copper. Silopi ash dissolution is well modelled by a diffusion controlled SCM process, but Yata□an and Tunçbilek give more scattered data. The common knee at 1 h is not obvious for Cu, but the near linearity of Al, Fe and Mn (>1 h) connect well to the straight line of Cu. Copper is most likely found as chalcopyrite in the whole coals [6, 9, 15]. This makes it logical to suggest that Cu is associated with Fe oxides in the ash. Copper forms very stable oxides with aluminum, but this is less likely considering the low ashing temperature, 550 EC [18, 19].

Mercury. Mercury is literally not dissolved in sulfuric acid, due to the low solubility of $HgSO_4$ [5, 6]. Other leachants must be amended to obtain mercury recovery.

Molybdenum. Molybdenum is present at unprecedented levels, 2290 mg/kg, in ash from Silopi asphaltites (Table 1). 79 % extraction is reached in 32 h. This is near the maximum value 88-90 % [4, 6]. The Elovich equation gives a straight line for Mo extraction, but a SCM model show the same steep onset as Fe and Al leaching. Al and Fe, in ash from Silopi, also reach near maximum extraction after 32 h [6, 7]. Mo is associated with organic material or sulfidic phases in coal and thus altered by ashing. The element is commonly present in solid solution with other sulfides, but high concentrations may also lead to a separate molybdenite (MoS_2) phase. Association with pyrite or chalcopyrite in the fuel suggests that Mo is primarily present as a dopant in ironoxides in the ash, but association with $CaSO_4$ in the ash has also been suggested [12]. The extraction of Mo is not affected by the combustion temperature (< 950 EC). Alternative leachants, natural waters or strong bases gave yields ranging from 10-30 %, but yields around 90 % can be obtained by pyrolysis followed by acid leaching [4].

Nickel. Nickel dissolution shows similar shapes for the three ashes. Silopi and Tunçbilek reach 17 % and 20 % extraction in 32 h, out of maximum yields of 31 % and 33 %, respectively. Surprisingly, Yata□an ash, with 24 % extraction after 32 h, reach 84 % dissolved nickel in 10 days [6]. 55 % extraction has been reported for Silopi ash in sulfuric acid, but literally no dissolution in natural waters and strong bases [4]. The shape of Ni extraction is also observed for Al and Fe dissolution and suggests association with clays [9]. Some differences persist regarding the ratio between initial leaching and 'slow phase' leaching, and we can not warrant that majority phases contain the same dopants in the two regimes. Apart from clays, both Al and Fe oxides may serve as matrices for Ni. Iron oxide association is more likely, after ashing at low or moderate temperatures, since bimetallic (bulk) oxides with aluminum require high temperature oxidation [18, 19]. A significant drop in the nickel extraction yield was observed after combustion of Silopi asphaltite at 850 EC, instead of 500 EC [4]. The lower yield was repeated for pyrolysis at 950 EC [4]. At lower combustion temperatures we merely observe alumina surface modifications and leaching of surface associated metals do not follow a SCM model.

Lead. Due to the low solubility of $PbSO_4$ [6, 20], only limited extraction of lead in sulfuric acid is observed, but reveals a smooth profile, albeit not a straight line, for Silopi asphaltite-ash. We obtain maximum extraction after 32 h treatment. Calcium alone of major components demonstrates similar characteristics [7]. Calcium dominates the neutralizing capacity for short contact times, but some contributions linger during the 30 min - 32 h period. Lead is mainly found as galena (PbS) in 'whole coals' [9]. We suggest the possibility that Pb^{2+} ions, after coal combustion, are substituted for Ca^{2+} ions in the untreated ash. This suggestion is well in line with the suggested association of Pb to $CaSO_4$ [12].

Tin. Sn is not leached and we note that SnO_2 is stable in sulfuric acid [5].

Thorium. The non-linear profile for Tunçbilek translates to a straight line in the Elovich model, but approximate linearity is also found for a range of other metals when X is plotted vs. ln(t) and the implications of the Elovich model are not clear [21]. 8 h of treatment almost completes the leaching process for all ashes and this mimics Ca [7] more than Al/Fe. Thorium is extracted to high percentages from Yata□an (90 %) and Elbistan (78 %) ashes [6], but also to modest levels in other lignite-ashes, notably Tunçbilek (32 %).

Uranium. The uranium concentration in untreated ash from Silopi is very high (Table 1), but also the two lignite-ashes show considerable radioactivity, from ^{238}U as well as ^{232}Th [11]. The main primary ore minerals are uraninite and pitchblende, often associated with mineral sulfides [13]. Ashing boosts the extraction yield of uranium dramatically and 79-94 % maximum dissolution is reported [6]. This points at the formation of uranyl - ions (UO_2^{2-}). Maximum extraction is reached after 8 h except for one odd value for Yata□an lignite-ash. This indicates association with calcium containing phases in the untreated ash, although we may not exclude surface association or even separate phases.

Vanadium. Vanadium is abundant in Silopi asphaltites and asphaltite-ash [6]. Combustion brakes the stable chelate of vanadyl-porphyrins and opens vanadium ions for extraction in acids. We do not reach maximum extraction after 32 h, but we recognize the SCM pattern of Al and/or Fe. Yields above 90 % were also observed after pyrolysis at 950 EC, which suggests a disintegrated porhyrin [4]. Alternative leachants, natural waters and strong bases gave yields below 10 %. We concede with literature [17] and suggest V association with clays (illite) in the ash, or possibly, with a separate phase of iron or aluminum oxide. Combustion temperatures below 950 EC have no effect on V extraction [4], which tells that no complex oxides were formed.

Zinc. The profile of zinc leaching from Tunçbilek is very similar to the profile of cadmium leaching and we note that the main occurrence of cadmium is as a substitutional defect in sphalerite [9, 15]. Extraction numbers between 70-90 % were reported for waste incineration ashes, but zinc bound as a trace element in minerals makes coal-ash a different material than ash from garbage combustion [20]. We note the possibility of spinel formation, $ZnFe_2O_4$, upon the combustion of lignites. The time dependence of waste-ash leaching [20] indicates that Zn is bound at the surface of fly ash particles, rather than as a dopant. It has been suggested that Zn is bound to $CaSO_4$ particulates [4].

Coal-Ash Treatment: **Residence Times and Process Design**. The above data may serve as input to full-scale plant studies on acid leaching [22-24]. Two additional concepts have been presented [5, 6]: (i) the use of ash for pH control in the biological oxidation of

sulfidic concentrates and (ii) a separate acid leaching process followed by metal recovery in the main bioleaching plant or a separate metallurgical unit. Conditions utilized in the present study (pH 1.0) mimic the biocatalyzed stage of a hydrometallurgical process for metal production from sulfidic minerals, albeit commonly used mesophilic organisms favor higher temperatures (40 EC).

The residence time of the biocatalyzed oxidation stage is 3-5 days, i.e., we will complete the fast phase of ash leaching and start the slow dissolution of more stable phases. This translates to 50-100 % lower concentrations of, for instance; Cd, U, Th and V, in the solid residue compared with the untreated ash. The issues that need to be addressed are twofold: (i) will the extracted elements hamper the biological activity and (ii) can the extracted elements be retrieved or removed economically with maintained quality of the main product, usually copper or zinc. We suggest that the recovery of Cd, Co, Cu, Ni and Zn is technically feasible and of potential economic value [6, 25, 26]. Mn and V may be amended at a higher cost. U and Th leaching are of interest to prevent the release of radioactive materials. A complete scheme for the acid leaching and recovery of Mo, V, Ni and U has been proposed [24]. In the present work we suggest that the washed ash will be mixed and deposited with mineral residues or the precipitates from the main biohydrometallurgical process [5, 6].

The residence times of intermediate (Fe/As) and final precipitation stages in a bioleaching process are around 2 h [5, 6]. pH is raised to 2.5 - 3.0 in the former and 7.0 in the latter. The usage of ash for pH adjustment in these stages needs to be addressed in further studies.

In a separate acid leaching plant we may choose the residence times independently of the requirements of parallel processes. We suggest the possibility to use acid leachate (excess sulfuric acid) from the bioleaching plant, but local feeds, from roasting or desulfurization units, coking plants or refineries, may determine the source of sulfuric acid. Acid leaching is simple and can be accommodated either at the power plant or the main hydrometallurgial plant [5, 6]. Leached elements can be shipped as precipitated hydroxides or sulfides to the main plant for metal recovery. Residues will be literally inert since no natural habitat will display a more acidic environment.

Further tests must be conducted with as received ash samples [6, 27]. Above we argued that the combustion temperature is critical, with higher temperature favoring more stable ceramics [28], but variations in fuel quality and additives from ash aftertreatment also affect leaching properties. Moreover, chlorine is found in ash from waste incineration both as a result of plastics in the fuel and as an additive [29]. Finally, it can not be taken for granted that stabilization by carbonatization or flocculation will reduce dissolution at low pH, which means that even deposits of stabilized ashes are an environmental hazard [6, 30].

Conclusions

Lignite- and asphaltite-ashes dissolve in sulfuric acid (initial S/L ratio 1:10, pH 1.0, 25 EC). We discern a 'fast regime' ending after 30 min and a second, 'slow regime' extending 10 days or more. The second stage is well modelled by a diffusion limited shrinking core (SCM) process.

High extraction yields of Th and U are observed during the initial 30 min of leaching. Ca, Ba and Pb readily precipitate as sulfates, but low levels of Ba and Pb dissolution were noticed. Extraction of the trace elements Cd, Co, Cr, Cu, Mo, Ni, V and Zn were observed during the second stage and linked to the dissolution of clays and other relatively stable complex minerals and oxides. 3-5 days of treatment may render an inert residue with 50-100 % lower concentrations of Cd, U, Th and V.

The recovery of Cd, Co, Cu, Ni and Zn is technically feasible using present hydrometallurgical processes. Additional measures are necessary for the recovery of Mn, Mo, Th, U and V, but schemes have been suggested and tested at bench or pilot scale. There is no need for additional extraction steps if direct acid leaching give high yields. Alternative acids, strong bases or complexing agents will be motivated if targeted elements remain in the solid residue. This is the case for Hg, Pb and Zr in the present study, due to the formation of insoluble sulfates.

Acknowledgement. We thank our colleagues Agah Köker and Selami Toprak from MTA in Ankara for discussions on coal pretreatments. We also thank Ömer Ünver from TKI Türkiye Kömür Isletmeleri Kurumu *(Eng. Turkish Coal Enterprises*) for his continued interest in our work and Michael L. Smith, Anabolic Laboratories, Phoenix/AZ for his careful reading of the manuscript. Last, but not least, we acknowledge Vattenfall AB and Ånge Energi for their support of our project.

References

(1) Harris W.R., Silberman D., Environ. Sci. Technol. 1983; 17; 139
(2) Nugteren H.W., Janssen-Jurkovícová M., Scarlett B., Fuel 2001; 80; 873
(3) Nugteren H.W., Janssen-Jurkovícová M., Scarlett B., J.Chem.Technol.Biotechnol. 2002; 77; 389
(4) Atamer H., Özdil G., Essiz R., Durmus H., 1979, Güneydogu Anadolu Bölgesi Asfaltit Küllerinden Molibden, Nikel ve Vanadyumun Kazanilmasi Amaciyla Liçing Ara∏t2mas2, MTA 6636, M.T.A. Enstitüsü Teknoloji Dairesi Radyoaktif ve Nadir Metaller Teknoloji Servisi, Ankara, *in Turkish*
(5) Paul M., Sandström Å., Paul J., Journal of Hazardous Materials (submitted)
(6) Seferinoglu M., Paul M., Sandström Å., Köker A., Toprak S., Paul J., Fuel 2003; 82; 1721
(7) Paul M, Seferinoglu M., Ayç2k G.A., Sandström Å., Paul J., Fuel (submitted)
(8) Camerani M.C., Somogyi A., Drakopoulos M., Steenari B.M., Spectrochim. Acta Part B 2001; 56; 1355
(9) Davidson R.M., Modes of Occurrence of Trace Elements in Coal - Results from an International Collaborative Programme, CCC/36, (IEA Coal Research, 2000, London)
(10) Levenspiel O., Chemical Reaction Engineering, (John Wiley, 1999, New York)
(11) Ayç2k G.A., Paul M., Smith M.L., Sandström Å., Paul J., Waste Management (manuscript)
(12) Querol X., Fernández-Turiel J.L., López-Soler A., Fuel 1995; 74; 331
(13) Hurlbut C.S. Jr., Klein C., Manual of Mineralogy (after James D. Dana) 19th Ed., (John Wiley, 1977, New York)
(14) López-Delgado A., Martín de Vidales J.L., Vila E., López F.A., J. Alloys and Compounds 1998; 28; 312
(15) Swaine D.J., Trace Elements in Coal, (Butterworth, 1990, London)

(16) Camerani Pinzani M.C., Somogyi A., Simionovici A.S., Ansell S., Steenari B.M., Lindqvist O., Environ. Sci. Technol. 2002; 36; 3165
(17) Palmer C.A., Filby R.H., Fuel 1984; 63; 318
(18) Centi G., Perathoner S., Applied Catalysis A: General 1995; 132; 179
(19) Trumble K.P., Acta Metallurgica et Materialia 1992; 40 SUPPL; S105
(20) Nagib S., Inoue K., Hydrometallurgy 2000; 56; 269
(21) Stumm W., Morgan J.J., Aquatic Chemistry: Chemical Equilibria and Rates in Natural Waters, 3rd Ed., (Wiley, 1996, New York)
(22) Katsuura H., Inoue T., Hiraoka M., Sakai S., Waste Management 1996; 16; 491
(23) Querol X., UmaƷa J.C., Alastuey A., Ayora C., Lopez-Soler A., Plana F., Fuel 2001; 80; 801
(24) Atamer H., Derman D., Özdil G., 1975, Güneydogu Anadolu Bölgesi Asfaltit Küllerinden Molibden, Nikel, Vanadyumun ve Uranyumum Kazan2lmas2, M.T.A. Enstitüsü Teknoloji Dairesi Radyoaktif ve Nadir Metaller Teknoloji Servisi, Ankara, *in Turkish*
(25) Jia C.Q., Xiao J.Z., Orr R.G., J. Environ. Sci. Health, Part A: Toxic/Hazardous Substances & Environmental Engineering 1999; 34; 1013
(26) Ahmed I.B., Gbor P.K., Jia C.Q., Can. J. Chem. Eng. 2000; 78; 694
(27) Steenari B.M., Schelander S., Lindqvist O., Fuel 1999; 78; 249
(28) Stach E., Mackowsky M.Th., Teichmüller M., Taylor G.H., Chandra D., Teichmüller M., Stach's Textbook of Coal Petrology, 2nd Ed., (Gebrüder Borntraeger, 1975, Berlin), pp. 122
(29) Chandler A.J., Eighmy T.T., Hartlén J., Hjelmar O., Kosson D.S., Sawell S.E., van der Sloot H.A., Vehlow J., Municipal solid waste incinerator residues, Study in Environmental Science 67 (Elsevier, 1997, Amsterdam)
(30) Wei M.C., Wey M.Y., Hwang J.H., Chen J.C., 1998, Stability of heavy metals in bottom ash and fly ash under various incinerating conditions, J. Hazard. Mater. 1998; 57; 145

Table 1. Concentrations in Untreated Ash

Element [mg/kg]	Fränsta/ sawmill residue	Yatagan/ lignite	Tunçbilek/ lignite	Silopi/ asphaltite
As	< 3	226	80.3	132
Ba	5840	409	422	297
Cd	5.3	2.43	0.457	123
Co	12.2	27.7	97.6	13
Cr	44	168	794	346
Cs	2.66	4.93	11.2	4.27
Cu	131	308	86	207
Hg	< 0.1	< 0.1	< 0.1	< 0.1
Mo	< 6	44.2	50	2290
Ni	21.5	111	2150	3030
Pb	22.8	187	79.2	22.8
Sn	< 20	< 20	< 20	< 20
Th	N/A	18	34.4	4.85
U	0.422	67.3	23.9	171
V	6.04	294	265	3990
Zn	1020	385	147	3890

THE STUDY OF HYDRODESULFURIZATION OF 4,6-DIMETHYLDIBENZOTHIOPHENE OVER PHOSPHORUS-ADDED NiMo/γ-Al_2O_3

Yongqiang Xu, Hongyan Shang, Chenguang Liu

Key Laboratory of Catalysis, CNPC
State Key Laboratory of Heavy Oil Processing
College of Chemistry & Chemical Engineering
University of Petroleum (East China),
Dongying, Shandong, 257061, China

Introduction

Deep hydrodesulfurization (HDS) of diesel oil has attracted much attention recently as the more and more strict environmental regulations. Among the sulfur compounds of diesel oil, dibenzothiophenes (DBTs, such as dibenzothiophene (DBT), 4-methyldibenzothiophene (4-MDBT), 4,6-dimethyldibenzothiophene (4,6-DMDBT)) are found the refractory compounds to HDS [1-4]. However, even now scientists have different ideas on the adsorption states of DBTs over the HDS catalysts and carriers [5-7], as a result, they proposed different HDS mechanism of DBTs. On the other hand, the reactive thermodynamics and kinetics of HDS of DBTs are still studied inadequately. Therefore, the studies of HDS of DBTs are the key subjects to the deep HDS of diesel oil.

The phosphorus-added hydrotreating catalysts were found have promoting effects on the HDS activity of these catalysts [8,9]. The reasons for that have various explanations. Kwak C. et al. [8] concluded that phosphorus modifies catalytic behavior in two ways: increase of active sites by enhanced metal dispersion and increase of Bronsted acidity. In this paper, the HDS of 4,6-DMDBT on phosphorus-added NiMo/γ-Al_2O_3 sulfide catalyst (P-NiMo/γ-Al_2O_3) was studied, moreover, the reaction network and mechanisms were advanced on the basis of GC, and GC-MS analyses of the reaction products.

Experimental

Material and Catalyst. 4,6-DMDBT was synthesized according to an improved method of literature [10]. Its purity is 99.6%, and its melting point is 153.5-154.1°C.

CoMo/γ-Al_2O_3 catalyst was prepared in the following way. γ-Al_2O_3(20-40 mesh) was impregnated with an aqueous solution of ammonium heptamolybdate, followed by drying at 120ºC for 5h, and calcinations in air at 500ºC for 5h. After that, it was impregnated with an aqueous solution of cobalt nitrates, dried and calcined as done above. The CoMo/γ-Al_2O_3 catalyst contains 16.1wt% MoO_3 and 3.4wt% CoO, CoO/(CoO+ MoO_3) (mol/mol)=1:3.5.

Phosphorus-added NiMo/γ-Al_2O_3 catalyst was prepared in the following way. The slurry of γ-Al_2O_3 mixed with P_2O_5 was extruded to form 1mm in diameter needle. Then it was dried in air at 120°C for 5h, and then crushed and sieved to get 20-24 mesh granules. The granules were calcined in air at 500°C for 5h. The phosphorus-added γ-Al_2O_3 was then impregnated with an aqueous solution of molybdenum oxide, nickel carbonate basic and phosphorus acid, followed by drying at 120ºC for 5h, and calcinations in air at 500ºC for 5h. The phosphorus-added NiMo/γ-Al_2O_3 catalyst contained 26wt.% MoO_3 and NiO, NiO /(NiO + MoO_3) (mol/mol)=1:3.5. The amount of phosphorus added to the catalyst was 3.5wt.%.

Reactor and Experimental Procedure. The HDS reaction was carried out in a fixed-bed flow microreactor, consisting of a 17mm i.d. stainless steel tube. 2ml of catalyst particles were diluted with quartz sand to 10ml, and then packed in the middle section of the tube, and the other sections were filled by quartz sand. The catalyst was presulfided before HDS reaction with 3wt%CS_2 in cyclohexane for 6h at 2.0MPa, 300°C, LHSV, $3h^{-1}$ and H_2/feed ratio (V/V), 200/1. After presulfidation, the reactant (1wt%4,6-DMDBT in decalin) was pumped into the reactor. 6h later, sampling of products was started at intervals of 30 min. the samples were immediately analyzed by gas chromatograph. Reaction pressure and temperature were then changed for studying the effects of them on HDS of 4,6-DMDBT. The reaction pressures used were 2.0, 1.5, 1.0MPa, while the reaction temperatures used were 300ºC, 280ºC, 260ºC.

Analysis. The samples were analyzed by Varian 3800 Chromatograph. The products were identified by GC-MS (Finnigan SSQ710).

Results and Discussion

The Analysis of Products of HDS and The Reaction Network. The products from reactions of 4,6-DMDBT and their yield at 300ºC under 2.0MPa over P-NiMo/γ-Al_2O_3 were shown in Table 1. The isomerization of 4,6-DMDBT to 3,6-DMDBT was found over P-NiMo/γ-Al_2O_3 as well as HDS. From Table 1, the speculated reaction network for HDS of 4,6-DMDBT is shown in Scheme 1.

Table 1 also shows the products from HDS of 4,6-DMDBT and their concentration at 300ºC under 2.0Mpa over sulfided CoMo/γ-Al_2O_3. It can be found that under the same reaction conditions, the conversion of 4,6-DMDBT over sulfided CoMo/γ-Al_2O_3 is much lower than that over P-NiMo/γ-Al_2O_3. That means the P-NiMo/γ-Al_2O_3 has higher 4,6-DMDBT-HDS activity than sulfided CoMo/γ-Al_2O_3. On the other hand, the ratio between cyclohexylbenzenes (CHBs) and biphenyls (BPs) in the products of HDS of 4,6-DMDBT over P-NiMo/γ-Al_2O_3, which approximately reflects the ratio of the rate of the desulfurization through hydrogenation (HYD) route to the direct desulfurization (DDS) route, is 3.05. But over sulfided CoMo/γ-Al_2O_3, it is 2.54, which means that P-NiMo/γ-Al_2O_3 has higher hydrogenation activity than CoMo/γ-Al_2O_3.

The concentrations of isomers such as 3,6-DMDBT, 3,4'-DMBP in the products of HDS of 4,6-DMDBT over P-NiMo/γ-Al_2O_3 are very low, which replies the high HDS activity of P-NiMo/γ-Al_2O_3 should not lie on its acidity, but on increase of active sites by enhanced metal dispersion.

Table 1. Concentration of HDS products of 4,6-DMDBT

Product	Concentration, wt.%	
	P-NiMo/Al_2O_3	CoMo/Al_2O_3
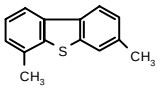	0.23	0.20
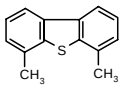	25.66	64.26
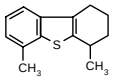 And its isomer	1.66	1.65
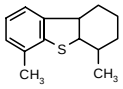	0.23	0.46
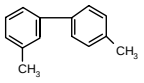	0.10	0.04
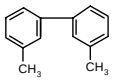	17.10	9.18
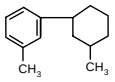 and its isomers	52.44	23.41
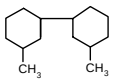 and its isomer	2.59	0.80

The Effect of Reaction Pressure And Reaction Temperature on HDS of 4,6-DMDBT. The concentration of products for HDS of 4,6-DMDBT under different reaction pressures at 300ºC is shown in Fig.1. Fig.1 illustrates that the reaction velocity of HYD routes in HDS of 4,6-DMDBT obviously decreases with the descending of reaction pressure. But the effect on DDS pathway is much smaller than that on HYD. As a result, the CHBs/BPs ratio descends greatly with the reducing of reaction pressure (as shown in Fig.2). It can also be found that the effect of reaction pressure on the transformation of 4,6-DMDBT is very obvious for the high selectivity of HYD route in the HDS reaction network of 4,6-DMDBT.

The concentration of products of HDS of 4,6-DMDBT at different reaction temperatures under 2.0MPa is shown in Fig.3. From Fig.3 it can be found that the reaction velocity of the HDS of 4,6-DMDBT and the DDS route, HYD route inside all obviously decrease with the descending of reaction temperature, which suggests that the HDS is not reach the thermodynamic equilibrium under the reaction conditions adopted in this experiment.

Conclusion

P-NiMo/γ-Al_2O_3 has higher 4,6-DMDBT-HDS activity and hydrogenation activity than sulfided CoMo/γ-Al_2O_3, which does not lie on its acidity, but on increase of active sites by enhanced metal dispersion. Effect of reaction pressure on the HYD route is higher than that on the DDS route for HDS of 4,6-DMDBT. Reaction temperature has obvious effect on all the HDS of 4,6-DMDBT and the DDS route, HYD route inside

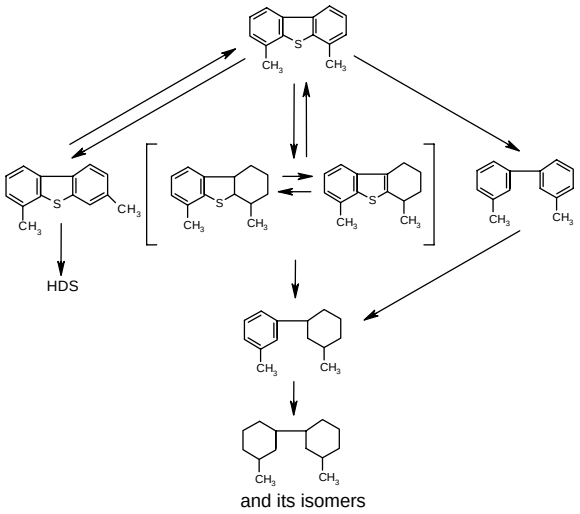

Scheme 1. Reaction network for HDS of 4,6-DMDBT on P-NiMo/γ-Al_2O_3.

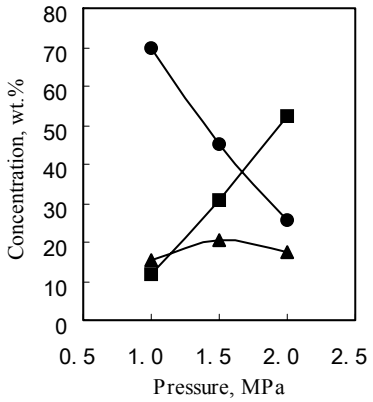

Figure 1. Concentration of hydrodesulfurization products of 4,6-DMDBT under different reaction pressure, ●4, 6-DMDBT, ▲ 3,3'-dimethylbiphenyl and 3,4'-dimethylbiphenyl, ■ 3,3'-dimethyldicyclohexyl

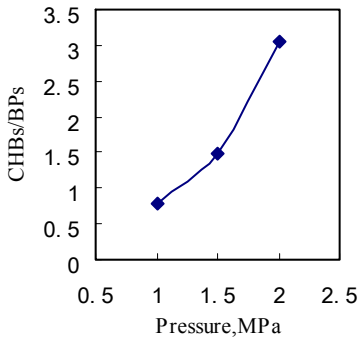

Figure 2. Ratio of dimethylcyclohexylbenzene to dimethylbiphenyl under different reaction pressure

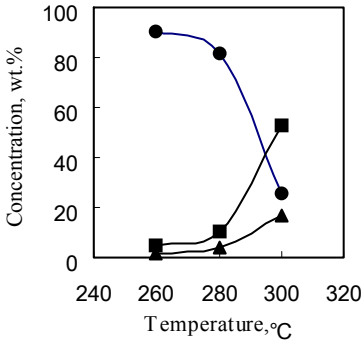

Figure 3. Concentration of HDS products of 4,6-DMDBT under different reaction temperatures, ●4, 6-DMDBT, ▲ 3,3'-dimethylbiphenyl and 3,4'-dimethylbiphenyl, ■ 3,3'-dimethyldicyclohexyl

References

(1) Amorelli A., Amos Y. D., Halsig C.P., et al., Estimate Feedstock Processsability [J], *Hydrocarb.Proc.*,1992, *71(6)*: 93-101.

(2) Shih S. S., Mizrahi S., Green L. A., et al., Deep Desulfurization of Distillates [J], *Ind. Eng. Chem. Res.*, 1992, *31*:1232-1235

(3) Kabe T., Ishihara A., Tajima H., Hydrodesulfurization of Sulfur-Containing Polyaromatic Compounds in Light Oil[J], *Ind. Eng. Chem. Res*., 1992, *31*: 1577-1580

(4) Schulz H., Bohringer W., Ousmanov F., et al.,, Refractory sulfur compounds in gas oils[J], *Fuel Processing Technology*, 1999, *61*: 5–41

(5) Macaud M., Milenkovic A., Schulz E.,et al., Hydrodesulfurization of Alkyldibenzothiophenes: Evidence of Highly Unreactive Aromatic Sulfur Compounds[J], *J. Catal.*, 2000,*193*:255-263.

(6) Kabe T., Qian W., Ishihara A., Study of Hydrodesulfurization of Dibenzothiophene on Ni-Mo/Al_2O_3, Mo/Al_2O_3,and Ni/Al_2O_3 Catalysts by the Use of Radioisotope ^{35}S Tracer[J], *J. Catal.*, 1994,*149*: 171-180.

(7) Laudau, M. V., Deep Hydrotreating of Middle Distillates from Crude and Shale Oils[J]. *Catalysis Today*, 1997,*36(4)*:393-429

(8) Kwak C., Kim M. Y., Choi K., et al., Effect of Phosphorus Addition on the Behavior of CoMoS/Al_2O_3 Catalyst in Hydrodesulfurization of Dibenzothiophene and 4,6-Dimethyldibenzothiophene[J], *Applied Catalysis A: General* 1999,185 (1): 19±27.

(9)Atanasova P., Lopez Cordero R., Mintchev L., et al., Temperature Programmed Reduction of the Oxide Form of PNiMo/Al_2O_3 Catalysts Before and After Water Extraction [J], *Applied Catalysis A: General* 1997, 159(1): 269-289.

(10) Kuchm-Caubere, C., Adach-Becker, S., Fort, Y. et. al., Expeditious and Efficient Syntheses of pure 4-Methyl and 4,6-Disubstituted Dibenzothiophene[J]. *Tetrahedron*, 1996,*52(27)*:9087-9092.

THE HYDRODESULFURIZATION OF 4-METHYLDIBENZOTHIOPHENE AND DIBENZOTHIOPHENE OVER SULFIDED Mo/γ-Al_2O_3

Yongqiang Xu, Chenguang Liu

Key Laboratory of Catalysis, CNPC,
State Key Laboratory of Heavy Oil Processing
College of Chemistry & Chemical Engineering
University of Petroleum (East China),
Dongying, Shandong 257061, China

Introduction

Deep hydrodesulfurization (HDS) of diesel oil has attracted much attention recently as the more and more strict environmental regulations. Among the sulfur compounds of diesel oil, dibenzothiophenes (DBTs, such as dibenzothiophene (DBT), 4-methyldibenzothiophene (4-MDBT), 4,6-dimethyldibenzothiophene (4,6-DMDBT)) are found the refractory compounds to HDS [1-4]. However, even now scientists have different ideas on the adsorption states of DBTs over the HDS catalysts and carriers [5-8], as a result, they proposed different HDS mechanism of DBTs. On the other hand, the reactive thermodynamics and kinetics of HDS of DBTs are still studied inadequately. Therefore, the studies of HDS of DBTs are the key subjects to the deep HDS of diesel oil.

Sulfided Mo/γ-Al_2O_3 catalyst has lower reactivity of catalysis than sulfided CoMo/γ-Al_2O_3 catalyst. But just because of this, most of the partly hydrogenated DBTs remain in the products, which are helpful to the studies of the HDS mechanism of DBT and 4-MDBT over Sulfided Mo/γ-Al_2O_3 catalyst.

Experimental

Material and Catalyst. DBT was synthesized by a modified procedure of the literature (9). Its purity is 99.7%, and its melting point is 98.2-98.4°C. 4-MDBT was synthesized according to an improved method of literature (10). Its purity is 94.6%, and its melting point is 63.6-63.7°C.

Mo/γ-Al_2O_3 catalyst was prepared in the following way. γ-Al_2O_3(20-40 mesh) was impregnated with an aqueous solution of ammonium heptamolybdate, followed by drying at 120ºC for 5h, and calcinations in air at 500ºC for 5h. The Mo/γ-Al_2O_3 catalyst contained 16.7wt%MoO_3.

Reactor and Experimental Procedure. The HDS reaction was carried out in a fixed-bed flow microreactor, consisting of a 17mm i.d. stainless steel tube. 5ml Mo/γ-Al_2O_3 catalyst (20-40 mesh) was packed in the middle section of the tube, and the other sections were filled by quartz sand. The catalyst was presulfided before HDS reaction with 3wt%CS_2 in cyclohexane for 6h at 2.0MPa, 300°C, LHSV, $3h^{-1}$ and H_2/feed ratio (V/V), 200/1. After presulfidation, the reactant (2wt%DBT or 2wt% 4-MDBT in toluene) was pumped into the reactor. 6h later, sampling of products was started at intervals of 30 min, the samples were immediately analyzed by gas chromatograph. Reaction pressure and temperature were then changed for studying the effects of them on HDS of DBT and 4-MDBT. The reaction pressures used were 2.0, 1.5, 1.0MPa, while the reaction temperatures used were 300ºC, 280ºC, 260ºC, 240ºC.

Analysis. The samples were analyzed by Varian 3800 Chromatograph. The products were identified by GC-MS (Finnigan SSQ710).

Results and Discussion

The Analysis of Products of HDS and The Reaction Network. The products from HDS of 4-MDBT and their yield at 300ºC under 2.0MPa over Mo/γ-Al_2O_3 are shown in Table 1. From that, the speculated reaction networks for HDS of 4-MDBT are shown in Scheme 1.

Table 2 shows the products from HDS of DBT and their concentration at 300ºC under 2.0Mpa over Mo/γ-Al_2O_3. From Table 2 and Table 1, it can be found that under the same reaction conditions, the conversion of 4-MDBT is slightly lower than that of DBT, and the molar ratio between cyclohexylbenzenes (CHBs) and biphenyls (BPs) in the products of HDS of 4-MDBT, which approximately reflects the ratio of the rate of the desulfurization through hydrogenation (HYD) route to the direct desulfurization (DDS) route, is 2.40. But to DBT, it is 0.97, which means that the HDS of 4-MDBT is essentially through the HYD route, while to DBT, the contributions of both routes are comparable. The methyl group in 4-MDBT molecule spatially hinds the "end on adsorption" of sulfur atom on the active sites of the catalyst, which depresses the DDS route and lead to the reduction of conversion of 4-MDBT. On the other hand, because the HYD route is also important to the HDS of DBT over Sulfided Mo/γ-Al_2O_3 catalyst, the difference between the conversion of DBT and 4-MDBT is not as obvious as that over Sulfided CoMo/γ-Al_2O_3 catalyst. Over Sulfided CoMo/γ-Al_2O_3 catalyst the HDS of DBT is essentially through the DDS route.

The Effect of Reaction Pressure on HDS of DBT and 4-MDBT. The concentration of products for HDS of DBT and 4-MDBT under different reaction pressures at 300ºC are shown in Fig.1 and Fig.2. The apparent kinetic orders of reaction pressure in different reaction among the HDS reactions are summarized in Table 3. Fig.1, Fig.2 and Table 3 illustrates that the reaction velocity of HYD routes in HDS of DBT and 4-MDBT obviously decreases with the descending of reaction pressure. But the effect on DDS is much smaller than that on HYD. As a result, the BPs/CHBs molar ratio increases greatly with the reducing of reaction pressure (as shown in Fig.3). Although the obviously difference exists between the transformation of DBT and that of 4-MDBT, it is found from Table 3 that the apparent kinetic orders of reaction pressure in HYD route in the HDS reaction network of DBT is similar with that of 4-MDBT. All of these imply that the reaction mechanisms of them may be similar.

Table 1. Concentration of HDS products of 4-MDBT

Product	Concentration, mol%
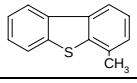	50.3649
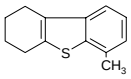	5.9015
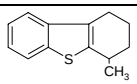	2.7141
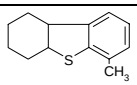	0.8139
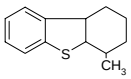	0.2748
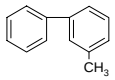	10.2775
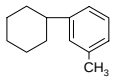	5.2329
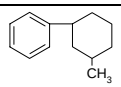	19.2945
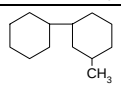	2.6525

The Effects of Reaction Temperature on HDS. The concentration of products of HDS of DBT and 4-MDBTat different reaction temperatures under 2.0MPa are shown in Fig.4 and Fig.5. From them it can be found that the reaction velocity of the HDS of DBT and 4-MDBT and the DDS routes, HYD routes inside all obviously decrease with the descending of reaction temperature, which suggests that the HDS is not reach the thermodynamic equilibrium under the reaction conditions adopted in this experiment. On the other hand, it is also found that the effects of reaction temperature on the DDS routes of the HDS of DBT and 4-MDBT are relatively weaker than that on the HYD routes, which lead to the BPs/CHBs molar ratio increases with the reducing of reaction temperature (as shown in Fig.6). This shows that the activation energy of the DDS routes is smaller than that of the HYD routes. At the same time, it can be found the effects of reaction temperature on conversion of DBT and 4-MDBT are different. The BPs/CHBs molar ratio in the products of HDS of 4-MDBT increases more slowly with the descending of reaction temperature than that of DBT. The reason speculated for that is the electron donor induction of the methyl group in 4-MDBT could promote the hydrogenation of the adjacent phenyl, leading to the reduction of activation energy of that. But that enhances the activation energy of the direct hydrogenolysis route for that's spatial restraining for the "end up adsorption".

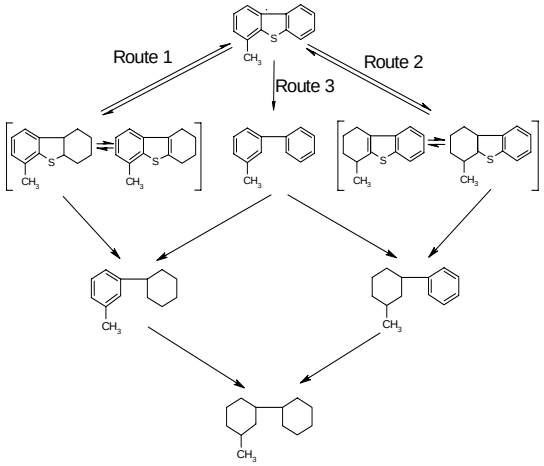

Scheme 1. Reaction network for HDS of 4-MDBT on Mo/γ-Al_2O_3, Route 1: hydrogenation route 1; Route 2: hydrogenation route 2; Route 3: hydrogenolysis route.

Table 2. Concentration of HDS products of DBT

Product	Concentration, mol%
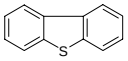	48.3679
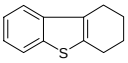	5.2465
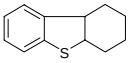	1.071
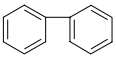	22.0872
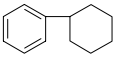	21.358
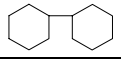	1.0265
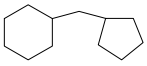	0.843

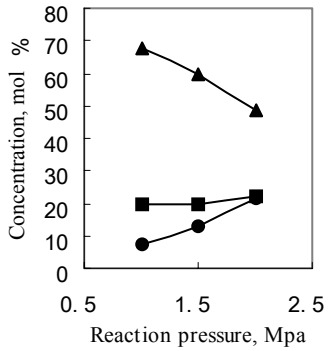

Figure 1. Concentration of HDS products of DBT under different reaction pressures, ▲DBT, ■biphenyl, ●cyclohexylbenzene

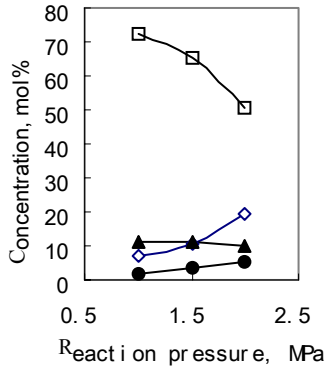

Figure 2. Concentration of HDS products of 4-MDBT under different reaction pressures, □4-MDBT, ○ (3- methyl-cyclohexyl)-benzene, ▲3- methyl-biphenyl, ●1-cyclohexyl-3-methyl-benzene

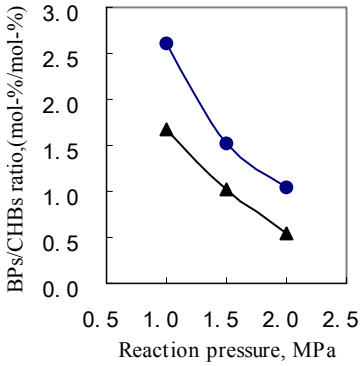

Figure 3. Molar ratio of BPs to CHBs under different reaction pressures, ●DBT, ▲4-MDBT

Table 3. Apparent Kinetic Orders of Reaction Pressure in Different Reactions

Reactant	DBT	4-MDBT
Conversion	0.66	0.83
Direct desulfurization route	0.18	0.15
Desulfurization route through hydrogenation	1.51	
HYD Route 1*		1.47
HYD Route 2*		1.36

*HYD route 1: to 1-cyclohexyl-3-methyl-benzene;
HYD route 2: to (3- methyl-cyclohexyl)-benzene

Conclusion

Comparing with sulfided CoMo/γ-Al_2O_3 catalyst, Sulfided Mo/γ-Al_2O_3 catalyst has lower reactivity of catalysis. As a result, most of the partly hydrogenated DBTs are detectable in the products. From that, the detail HDS mechanisms of DBT and 4-MDBT were proposed. over Sulfided Mo/γ-Al_2O_3 catalyst, the HDS of 4-MDBT occurs mainly through the HYD route. But to DBT, the contributions of both routes are comparable. The methyl group in 4-MDBT molecule spatially hinds the "end on adsorption" of sulfur atom on the active sites of the catalyst, which depresses the DDS route and lead to the reduction of conversion of 4-MDBT. However, the HYD route is also important to the HDS of DBT over Sulfided Mo/γ-Al_2O_3 catalyst, thus the difference between the conversion of DBT and 4-MDBT is not as obvious as that over Sulfided CoMo/γ-Al_2O_3 catalyst.

Descending reaction pressure evidently causes the descending of reaction rate of the hydrogenation routes of HDS of 4-MDBT and DBT. However, the reaction rate of the direct hydrogenolysis routes slightly ascends with the descending of reaction pressure. The effect of reaction pressure on the conversion of 4-MDBT is higher than that on DBT.

Reaction temperature has obvious effect on both the direct hydrogenolysis routes and the hydrogenation routes of HDS of 4-MDBT and DBT. However, the electron donor induction of the methyl group in 4-MDBT can promote the hydrogenation of the adjacent phenyl, leading to the reduction of activation energy of that. But that enhances the activation energy of the direct hydrogenolysis route for that's spatial restraining for the "end up adsorption".

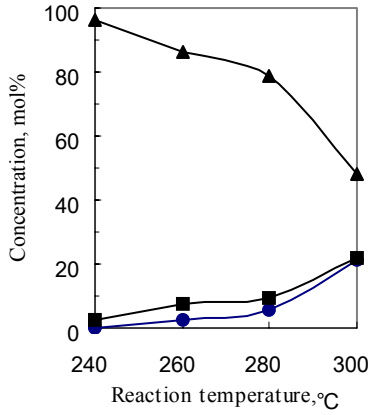

Figure 4. Concentration of HDS products of DBT under different reaction temperatures, ▲DBT, ■biphenyl, ●cyclohexylbenzene.

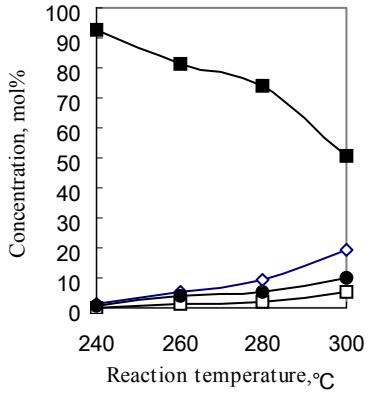

Figure 5. Concentration of HDS products of 4-MDBT under different reaction temperatures, ■4-MDBT, ○ (3- methyl-cyclohexyl)-benzene, ●3- methyl-biphenyl, □1-cyclohexyl-3-methyl-benzene

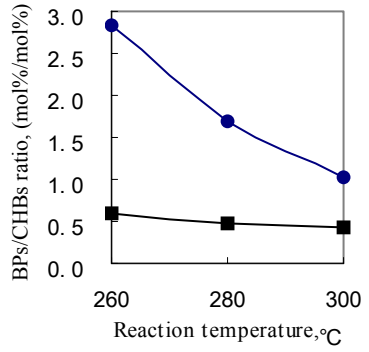

Figure 6. Molar ratio of BPs to CHBs under different reaction temperatures, ●DBT, ▲4-MDBT

References

(1) Amorelli A., Amos Y. D., Halsig C.P., et al., Estimate Feedstock Processsability [J], *Hydrocarb.Proc.*,1992, *71(6)*: 93-101.
(2) Shih S. S., Mizrahi S., Green L. A., et al., Deep Desulfurization of Distillates [J], *Ind. Eng. Chem. Res.*, 1992, *31*:1232-1235
(3) Kabe T., Ishihara A., Tajima H., Hydrodesulfurization of Sulfur-Containing Polyaromatic Compounds in Light Oil[J], *Ind. Eng. Chem. Res.*, 1992, *31*: 1577-1580
(4) Schulz H., Bohringer W., Ousmanov F., et al.,, Refractory sulfur compounds in gas oils[J], *Fuel Processing Technology*, 1999, *61*: 5–41
(5) Macaud M., Milenkovic A., Schulz E.,et al., Hydrodesulfurization of Alkyldibenzothiophenes: Evidence of Highly Unreactive Aromatic Sulfur Compounds[J], *J. Catal.*, 2000,*193*:255-263.
(6) Singhal, G. H., Espino R. L., Sobel J. E., Hydrodesulfurization of Sulfur Heterocylic Compounds: Reaction Mechanism[J], *J.Catal.*,1981,*67*: 446-456.
(7) Kabe T., Qian W., Ishihara A., Study of Hydrodesulfurization of Dibenzothiophene on Ni-Mo/Al_2O_3, Mo/Al_2O_3,and Ni/Al_2O_3 Catalysts by the Use of Radioisotope ^{35}S Tracer[J], *J. Catal.*, 1994,*149*: 171-180.
(8) Laudau, M. V., Deep Hydrotreating of Middle Distillates from Crude and Shale Oils[J]. *Catalysis Today*, 1997,*36(4)*:393-429
(9) Gilman, H. & Jcoby, A. L., Dibenzothiophene: Orientation and Derivatives[J]. *J. Org. Chem.*, 1938, *3*:108-119
(10) Kuchm-Caubere, C., Adach-Becker, S., Fort, Y. et. al., Expeditious and Efficient Syntheses of pure 4-Methyl and 4,6-Disubstituted Dibenzothiophene[J]. *Tetrahedron*, 1996,*52(27)*:9087-9092.
(11) Stanislaus A., Cooper, B. H., Aromatic Hydrogenation Catalysis: A Review[J], *Catalysis Reviews-Science and Engineering*, 1994, *36(1)*:75-123.
(12) Vasudevan P.T., A Review of Deep Hydrodesulfurization Catalysis[J], *Catalysis Reviews-Science and Engineering*, 1996, *38(2)*:161-188.